UNLV Theses, Dissertations, Professional Papers, and Capstones

2009

# High pressure phase transistions in the lanthanide sesquioxides

Jason Patrick McClure
*University of Nevada Las Vegas*

## Repository Citation

HIGH PRESSURE PHASE TRANSISTIONS IN THE

LANTHANIDE SESQUIOXIDES

By

Jason Patrick McClure

Bachelor of Science
Denison University, Granville
2002

A dissertation submitted in partial fulfillment
of the requirements for the

**Doctor of Philosophy in Physics**
**Department of Physics and Astronomy**
**College of Science**

**Graduate College**
**University of Nevada, Las Vegas**
**December 2009**

THE GRADUATE COLLEGE

We recommend that the dissertation prepared under our supervision by

**Jason Patrick McClure**

entitled

**High Pressure Phase Transitions in the Lanthanide Sesquioxides**

be accepted in partial fulfillment of the requirements for the degree of

**Doctor of Philosophy**
Physics

Andrew Cornelius, Committee Chair

Oliver Tschauner, Committee Member

Len Zane, Committee Member

Brendon O'Toole, Graduate Faculty Representative

Ronald Smith, Ph. D., Vice President for Research and Graduate Studies
and Dean of the Graduate College

**December 2009**

ABSTRACT

**High Pressure Phase Transitions in the Lanthanide Sesquioxides**

by

Jason Patrick McClure

Dr. Andrew Cornelius, Examination Committee Co-Chair
Associate Professor of Physics
University of Nevada Las Vegas

Dr. Oliver Tschauner, Examination Committee Co-Chair
Associate Research Professor of Physics
University of Nevada Las Vegas

Crystallizing into 5 known polymorphic forms, the rare-Earth sesquioxides $RE_2O_3$ represent a family of 4-f electron compounds that have been the subject of study for many years. Aspects of the systematics in the structural phase transitions for $RE_2O_3$ (RE=La, Sm, Eu, Gd, Y, Er, Yb, Lu) under pressure were studied using diamond anvil cells (DACs). As a part of this study, detailed equation of state (EOS) data for all these compounds were obtained through the use of angle-dispersive x-ray diffraction (XRD) where anomalies in compression data led to the detailed investigation into one particular rare-Earth sesquioxide, $La_2O_3$.

I show evidence that a long established sequence of high pressure phase transformations in rare-Earth sesquioxides involve more than the five currently known phases. In XRD patterns acquired by imaging detectors at pressures above 7.5 GPa, new reflections appear at low $2\theta$ angle, implying that a super lattice forms. High resolution XRD scans reveal peak splittings consistent with a monoclinic distortion of the A-type structure. A model of the distorted A-type structure is derived using group-subgroup relations to predict peak splittings and unit cells refined based on the observed XRD

patterns. Super lattice formation is further supported by Raman spectra acquired for separate samples which show a doubling of the $A_{1g}$ stretching mode of the A-type phase above 4 GPa. IR absorption and Raman scattering data are used together in a normal coordinate analysis where calculated mode frequencies model the observed spectra up to 18 GPa with reasonable refined values for all force constants. Until this study, there have been no reported pressure induced structural phase transitions outside the 5 known rare earth sesquioxide polymorphs.

## ACKNOWLEDGEMENTS

I first and foremost acknowledge my advisor Dr. Malcolm Nicol for his support and guidance throughout this project. It deeply saddens me that his passing was prior to the fruition of this dissertation; however, I am confident that the work presented herein would have made him proud.

I would also like to think the faculty who served on my committee for their continued guidance and support during this research project.

TABLE OF CONTNETS

LIST OF FIGURES

LIST OF TABLES

CHAPTER 1

INTRODUCTION

The lanthanides, or rare-Earths (RE) as they commonly referred, comprise lanthanum

and the 14 elements spanning the lanthanide series of the periodic table (La-Lu).  It is

also common in the many discussions regarding lanthanides, that the transition metals

scandium and yttrium be included because of their similarity in crystal structure and

chemistry to the lanthanides.

The lanthanide series begins with the filling of the 4f electron shell starting with

lanthanum having electronic configuration [Xe] $4f^05d^16s^2$.  Because the 4f electrons

penetrate the Xe core appreciably, they do not participate in bonding and are core like in

nature.[1]  The s and d valence electrons thus dominate in bonding and leave their

respective atomic cores' in a trivalent state except for Eu, Yb, Ce, and Pr where divalent

and tetravalent states are also observed.  The screening of the 4f electrons by the Xe core

serves to leave the bulk properties of the lanthanides relatively unchanged as electrons

are added to the 4f shell.[2]  It is because of this that the properties of the trivalent

lanthanides are expected to vary in a gradual manner as one traverses the series.

Systematic aspects for the rare-Earth (RE) metals at high pressure have been the

subject of investigation for more than forty years.[3] Early empirical studies revealed a

correlation between the crystal structure of trivalent lanthanide metals and the relative

volume occupied by the ion core.[4]  More specifically, it was determined that at as the

ionic radii increase from right to left across the Lanthanide series (from Lu to La) the

crystal structure sequence hcp -> Sm-Type->dhcp->fcc is observed while at ambient

conditions.[†] This sequence of closed packed structures is also observed as a series of structural phase transitions occurring with increasing pressure.[4] Latter, energy band calculations show evidence that the relative volume of the lanthanide ion core is correlated to a measure of the d-band occupancy.[5] Moreover, it is was shown that the d-band contribution to the total energy is what actually drives the lattice through the observed crystal structure sequence. That is, Lu, which crystallizes into an hcp structure at standard temperature and pressure (STP), has a d-band occupation number of about 1.5. La on the other hand, which crystallizes into a dhcp structure at STP, has a d-band occupation number on the order of 2.7. Because the crystal structure sequence hcp -> Sm-Type->dhcp->fcc is observed in the lanthanide metals as a function of increasing pressure, leads one to the natural conclusion that pressure has the effect on increasing the energy of electrons in the s-band relative to the d-band. At sufficient pressure, a transition in electronic state, s->d transfer, is observed and the number of d electrons per atom in the conduction band tends toward 3.

Further studies show the structural phase transition sequence observed in the "regular" trivalent lanthanide metals (La through Lu excluding Ce, Eu, Yb and Pr which adopt divalent or tetravalent states) is observed in metallic yttrium where no 4f electrons are present.[6] For metallic yttrium, this structural phase transition sequence is again regarded as the result of pressure changing the number of d electrons in the conduction band. However, yttrium's absence of any 4f electrons provides support for the argument that the existence of anomalous structural phase transitions in the regular lanthanide metals must be the result of 4f electron character at the Fermi surface. That is, the 4f electrons

---

[†] Lanthanum adopts a dhcp structure at ambient temperature and pressure.

should show a tendency toward becoming more delocalized or hybridized with other electron bands as pressure is increased.

The most obvious place to look for a relatively low pressure anomaly in the lanthanide metals' structural phase transition sequence would be where there is already a high d-band occupation number and only one 4f electron present. That is, metallic cerium. There have been many studies to date that show metallic cerium to transform from fcc ($\gamma$) -> fcc' ($\alpha$) -> bcm ($\alpha''$) -> bct ($\epsilon$) at pressures 0.7, 5.3, and 12.5 GPa.[7-10] The structural phase transitions observed beyond the fcc phase have all been attributed, by these authors, to be the result of 4f electron delocalization and/or hybridization.

In efforts to determine the complete high pressure phase transition scheme in the "regular" lanthanide metals, we turn our attention back to La. In the course of the electron s -> d-band transfer with increasing pressure, La finds itself already at a d-band occupation number of approximately 2.7 at STP.[5] Thus; one would expect that in a relatively low pressure range, the rest of the phase transition sequence should be observed without formation of anomalous phases occurring due to 4f electron contributions. That is, low pressure with respect to say the pressure required to transform Lu from its hcp structure at STP to the dhcp structure La adopts at STP, which is on the order of 50 GPa. In fact, compression studies on La revealed the phase transition sequence dhcp -> fcc -> distorted-fcc occurring at pressures STP -> 2.5 GPa -> 7 GPa respectively.[11]

The fcc to distorted fcc (dist-fcc) phase transition occurring in La has also been shown to occur in Pr, Nd, Pm, Sm, Gd, and Yb at gradually increasing pressures.[12-14] The symmetry change at the fcc -> dist-fcc phase transition was observed experimentally by the observation of weak super lattice reflections via energy dispersive x-ray diffraction

3

(EDX) patterns where the intensities of super lattice peaks were seen to continuously go to zero at the transition pressure. This behavior is indicative of a second order or weak first order structural phase transition. The phenomenological theory of structural phase transitions, ubiquitously referred to as Landau Theory in these regards, was used to describe the possible structures the dist-fcc phase could adopt and to explain the nature of the phase transition.[15]

To date, the high pressure phase transition sequence observed for the "regular" lanthanide metals is hcp -> Sm-type -> dhcp -> fcc -> dist. fcc for increasing pressure and decreasing atomic number.[16] A number of anomalous phases have been found outside this sequence and their origins have been largely attributed to different effects from the 4f electrons.[13,16] A rather comprehensive listing of the phase transition in the lanthanide metals has been published by David Young.[17]

The depth of our understanding regarding the behavior of electron interactions in the 4f elements is clearly demonstrated through the systematic study of their behavior at high pressure. The lanthanide sesquioxides, or rare-Earth sesquioxides as they are referred to henceforth, comprise a smaller known set of crystallographic structures (as compared to their elemental forms) whose properties are also closely tied to 4f electron occupation number. An effort is made in this dissertation to further our understanding of the systematic relationships observed amongst rare-Earth sesquioxides at high pressure and to set the stage for future work to better our understanding of 4f electron interactions in the lanthanides.

## 1.1 The Sesquioxide Crystal Structure of the A-Type

At ambient conditions, three polymorphic modifications of the rare-Earth sesquioxides exist[18]. Their structures have been classified as A, B, or C-type corresponding to hexagonal, monoclinic, and cubic structures, respectively. For different radii of the $RE^{+3}$-cation and thermal histories, the rare-Earth sesquioxides will adopt one of the three structural modifications. The A-type structure is the stable phase for RE = La, Ce, Pr, and Nd. For some thermal histories, $Sm_2O_3$, $Eu_2O_3$, and $Gd_2O_3$, adopt either the B or C-type structure. The C-type structure is seen for Re = Tb, Dy, Ho, Sm, Eu, Gd, Er, Tm, Yb, Lu, Y, and Sc.[18]

The crystal structure of the A-type rare-Earth sesquioxide was first investigated by Zacharisen in 1926 and later challenged by Pauling in 1928.[18,19] Although it seems that the spacegroup P-3 2/m 1 was undisputed, the same was not true for the atomic site symmetries for the oxygen anions. In 1953 a neutron diffraction study of the A-type structure by Koehler helped to support the atomic site symmetries proposed by Pauling in 1928.[19] Pauling's structure found further support in 1985 when an X-ray diffraction experiment was performed by Barnighausen on single crystals of A-$Ce_2O_3$.[20] The currently accepted A-type structure is primitive hexagonal and is represented by the P-3 2/m 1($D^3_{3d}$) space group, number 164. In the unit cell, two $RE^{+3}$ cations and two $O^{-2}$ anions sit on different $C_{3v}$ (Wyckoff-2d) sites with one $O^{-2}$ anion on a $D_{3d}$ (Wyckoff-1a) site. There is one formula unit per cell (Z=1), and the $RE^{+3}$ cations are 7-fold coordinated. Table 1.1 lists a record of all experimentally determined crystal structure parameters for rare-Earth sesquioxides adopting the A-type polymorph at ambient conditions.

Table 1.1 Crystallographic structure data for rare-Earths crystallizing in the
A-type polymorph at ambient conditions

| | | | Rare-Earth Sesquioxides $RE_2O_3$ A-type Polymorph | | |
|---|---|---|---|---|---|
| | $a(A)$[1] | $c(A)$[1] | z of RE Atoms[2] | z of O Atoms[2] | Volume$(A^3)$ |
| La | 3.937 | 6.129 | 0.2454 | 0.6471 | 16.457 |
| Ce | 3.890 | 6.070 | 0.2454 | 0.6471 | 15.909 |
| Pr | 3.857 | 6.016 | 0.2454 | 0.6471 | 15.501 |
| Nd | 3.829 | 5.997 | 0.2454 | 0.6471 | 15.231 |
| Pm | 3.802 | 5.954 | 0.2454 | 0.6471 | 14.907 |

[1]Lattice constants (a and c) are obtained from reference [21]. [2]Atomic
positions for RE and O atoms are obtained from reference [20].


Figure 1.1 shows the unit cell for the A-type structure reconstructed graphically using

the crystallographic data from Table 1.1. The unit cell is oriented with the **c** axis vertical

and the **a** axis out of the page. The $RE^{3+}$ cations are pictured in metallic gray (larger

spheres) and the $O^{2-}$ anions are pictured in blue (smaller spheres). Extra space has been

added to the unit cell to allow for envisioning the $REO_7$ coordination polyhedra.

Because of the relatively small number of rare-Earths known to crystallize in the A-

type structure at ambient conditions, $La_2O_3$ was chosen to be the only one investigated.

This decision is based on the hypothesis that, if a high pressure phase transition is to

occur outside of the known polymorphs, it should appear first in the one with already the

highest anion coordination number, the A-type. Additionally, elemental lanthanum has

the lowest observed phase transition pressure from the fcc to dist.fcc phases with respect

to all other lanthanide metals.[16]
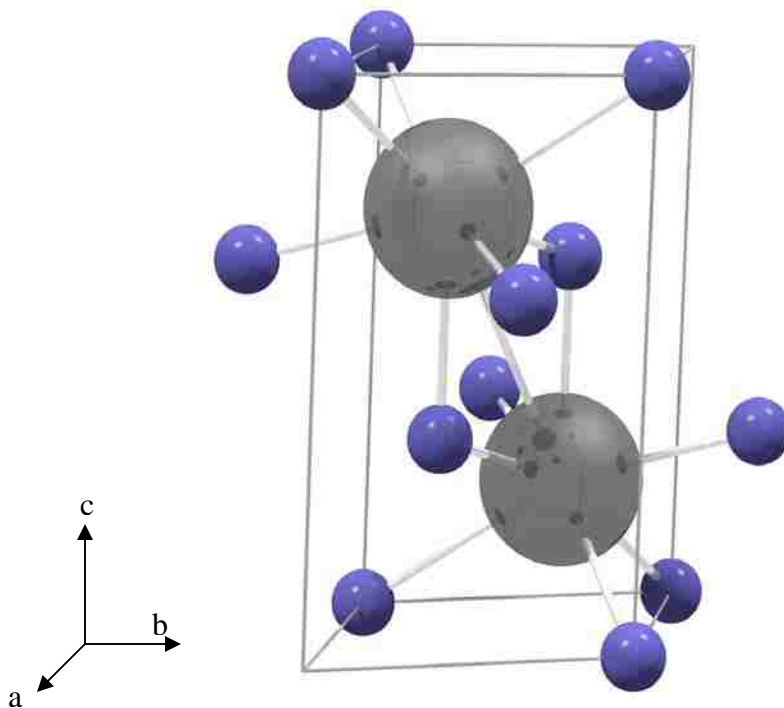
Figure 1.1 The crystal structure of the A-type rare-Earth sesquioxide.

## 1.2   The Sesquioxide Crystal Structure of the B-Type

The crystal structure of the B-type is known to be stable in $Sm_2O_3$, $Eu_2O_3$, and $Gd_2O_3$

above temperatures of 800, 1200, and 1400 $^{\circ}$C, respectively, at ambient pressure.[17]

However, upon quenching, the B-type phase will remain as a metastable phase at ambient

temperature.[22]  This effect has also been observed in my work upon sintering and

subsequently quenching these materials at temperatures in excess of 1400$^{\circ}$C.  The most

recent crystal structure determination for the B-type phase was in 1978 by Harry Yakel

and yielded a monoclinic structure with the C2/m space group.[23]  In the unit cell, 12 $RE^{+3}$

cations and 16 $O^{-2}$ anions are situated on 7 different $C_s$ (Wyckoff-4i) sites with two $O^{-2}$

anions on a single $C_i$ (Wyckoff-2b) site.  There are six formula units per cell (Z=6), and

the $RE^{+3}$ cations are 6/7-fold coordinated.  Table 1.2.1 gives an account of the reported

lattice parameters for all rare-Earths that are known to crystallize into the B-type

structures at ambient pressure.

Table 1.2.1  Crystallographic structure data for rare-Earths crystallizing in the
B-type polymorph at ambient conditions

| | | | | | |
|---|---|---|---|---|---|
| Rare-Earth Sesquioxides $RE_2O_3$ B-type Polymorph | | | | | |
| | a(A) | b(A) | c(A) | β(degrees) | Volume(A$^3$) |
| Sm[24] | 14.17 | 3.63 | 8.84 | 99.96 | 14.928 |
| Eu[23] | 14.1105 | 3.6021 | 8.8080 | 100.037 | 14.695 |
| Gd[22] | 14.061 | 3.566 | 8.760 | 100.100 | 14.414 |

Reported uncertainties are in the last decimal place

In Table 1.2.2, I have listed the atomic positions as determined by Yakel.[23]  Here, I

only list the atomic positions for Eu and suggest that this is the general case for the other

rare-Earths Sm, Eu, and Gd.  This is justified given that all other reports have overlapping

uncertainties for the atomic positions of the different rare-Earth species and what I'm

reporting is the best that are known.

Table 1.2.2  Positional parameters for the B-type polymorph at
ambient conditions.

| | | | | | |
|---|---|---|---|---|---|
| Atomic Possitions for Rare-Earth Sesquioxides $RE_2O_3$ B-type Polymorph[23] | | | | | |
| | x | y | z | site symmetry | Multiplicity |
| RE1 | 0.13740 | 0.5 | 0.4897 | $C_s$ | 4 |
| RE2 | 0.18972 | 0.5 | 0.13760 | $C_s$ | 4 |
| RE3 | 0.46635 | 0.5 | 0.18763 | $C_s$ | 4 |
| O1 | 0.1291 | 0.0 | 0.2855 | $C_s$ | 4 |
| O2 | 0.3248 | 0.5 | 0.0267 | $C_s$ | 4 |
| O3 | 0.2961 | 0.5 | 0.3732 | $C_s$ | 4 |
| O4 | 0.4734 | 0.0 | 0.3431 | $C_s$ | 4 |
| O5 | 0.0000 | 0.5 | 0.0000 | $C_i$ | 2 |

Reported uncertainties are in the last decimal place.

With the data from Tables 1.2.1 and 1.2.2, I rendered an image of the unit cell for the B-type phase as shown in Figure 1.2. The unit cell is oriented with the **c** axis vertical and the **b** axis into the page. The $RE^{3+}$ cations are pictured in metallic gray (larger spheres) and the $O^{2-}$ anions are pictured in blue (smaller spheres).
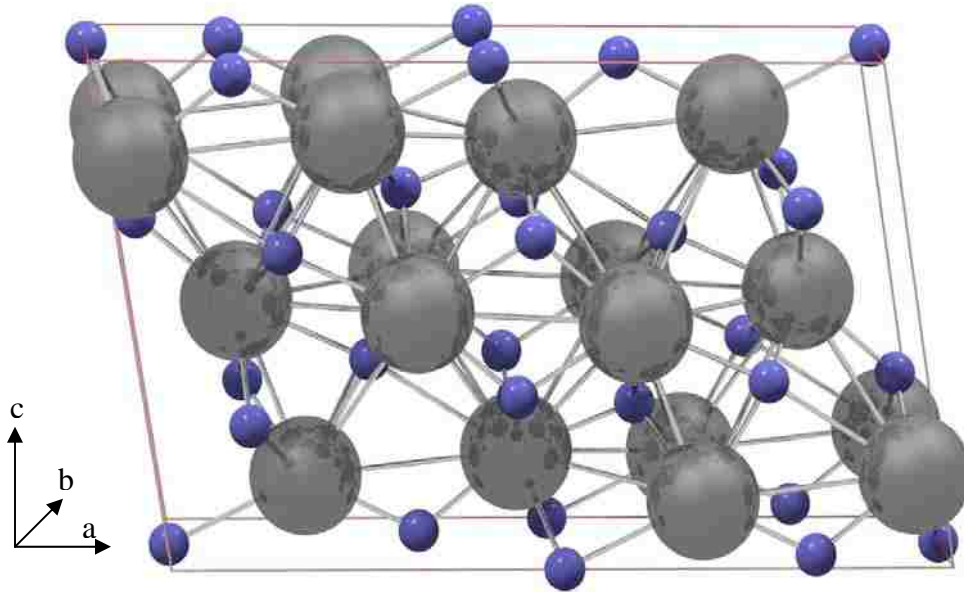


Figure 1.2    The crystal structure of the B-type rare-Earth sesquioxide

## 1.3  The Sesquioxide Crystal Structure of the C-Type

The C-type structure was first described by Pauling and Shappel in 1930 after investigating the mineral bixbyite $(Fe,Mn)_2O_3$.[25]  Subsequently, many rare-Earth sesquioxides have been shown to adopt this structure.[21,25,26]

The C-type structure is inner-center cubic and adopts the space group I-a3.  In this unit cell, 8 $RE^{+3}$ cations are on $S_6$ (Wyckoff-8b) sites and 24 are on $C_2$ (Wyckoff-24d) sites. The oxygen positions occupy 48 $C_1$ (48e-Wyckoff) general sites.  There are 16 formula units per cell (Z=16), and the $RE^{+3}$ cations are 6-fold coordinated.  Table 1.3 summarizes the crystal structure data on the rare-Earths adopting the C-type structure.

9

Table 1.3 Crystallographic structure data for rare-Earths crystallizing in the C-type polymorph at ambient conditions

| | | Rare-Earth Sesquioxides $RE_2O_3$ C-type Polymorph | | | | | |
|---|---|---|---|---|---|---|---|
| | a(A) | x of RE Atoms | x of O Atoms | y of O Atoms | z of O Atoms | Volume($A^3$/atom) | Reference |
| Sm | 10.932 | -0.035 | 0.385 | 0.145 | 0.380 | 16.33 | [21] |
| Eu | 10.8591 | -0.0330 | 0.3900 | 0.1519 | 0.3807 | 16.006 | [27] |
| Gd | 10.813 | -0.035 | 0.385 | 0.145 | 0.380 | 15.80 | [21] |
| Tb | 10.7291 | -0.0328 | 0.3989 | 0.1517 | 0.3808 | 15.438 | [27] |
| Dy | 10.667 | -0.035 | 0.385 | 0.145 | 0.380 | 15.17 | [21] |
| Y | 10.5981 | -0.0324 | 0.3907 | 0.1518 | 0.3801 | 14.880 | [28] |
| Er | 10.547 | -0.035 | 0.385 | 0.145 | 0.380 | 14.67 | [21] |
| Tm | 10.4855 | -0.033 | 0.392 | 0.153 | 0.377 | 14.410 | [27] |
| Yb | 10.4329 | -0.0336 | 0.391 | 0.151 | 0.380 | 14.195 | [27] |
| Lu | 10.391 | -0.035 | 0.385 | 0.145 | 0.380 | 14.02 | [21] |

Reported uncertainties are in the last decimal place in the recorded figures.

Figure 1.3 shows a rendered image of the unit cell for the C-type structure. I have used the structure information in Table 1.3 for $Y_2O_3$ to construct Figure 1.3 because it is the most recent and seemingly most accurate structure determination for the C-type phase. The unit cell is oriented with the **c** axis vertical and the **a** axis out of the page. The $RE^{3+}$ cations are pictured in metallic gray (larger spheres) and the $O^{2-}$ anions are pictured in blue (smaller spheres).
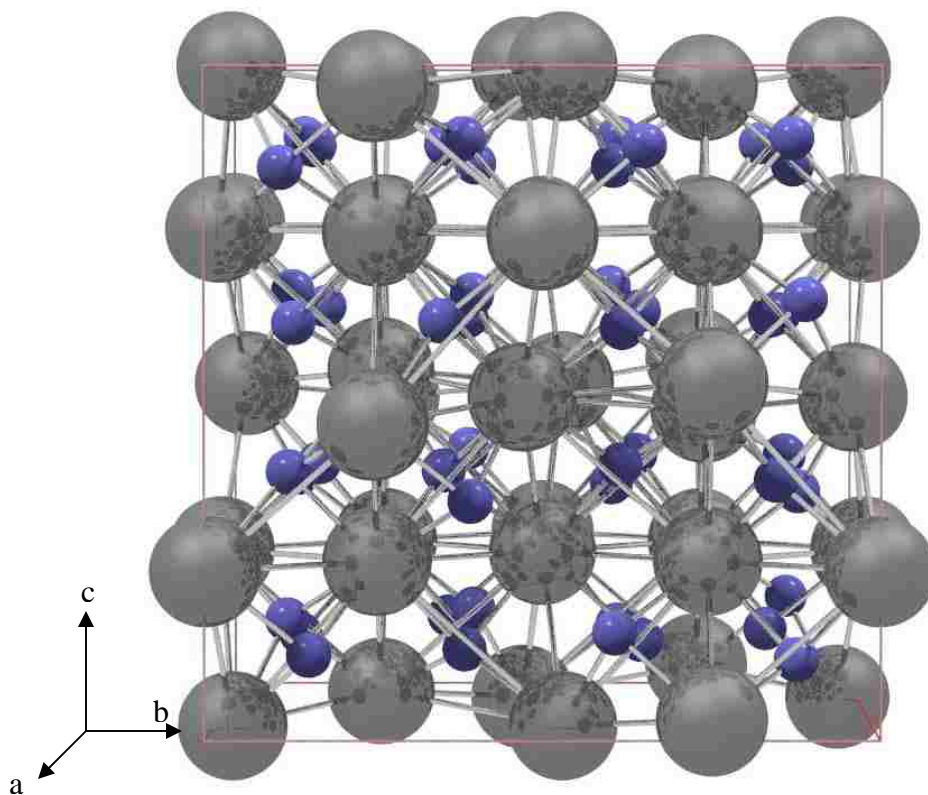


Figure 1.3    The crystal structure of the C-type rare-Earth sesquioxide

This, seemingly complex bixbyite-type structure is closely related to the more familiar cubic $CaF_2$-type structure. In $CaF_2$, the Ca and F atoms are situated on m-3m (Wyckoff-4a) and -43m (Wyckoff-8b) sites, respectively. A doubling of the unit cell for $CaF_2$ along each axis, results in a structure almost identical to the C-type structure. Shown for clarity

in Figure 1.4 is the $CaF_2$ unit cell doubled along the **a**, **b**, and **c** axis.  The calcium and

fluorine atoms are shown in gray (larger spheres) and blue (smaller spheres) respectively.
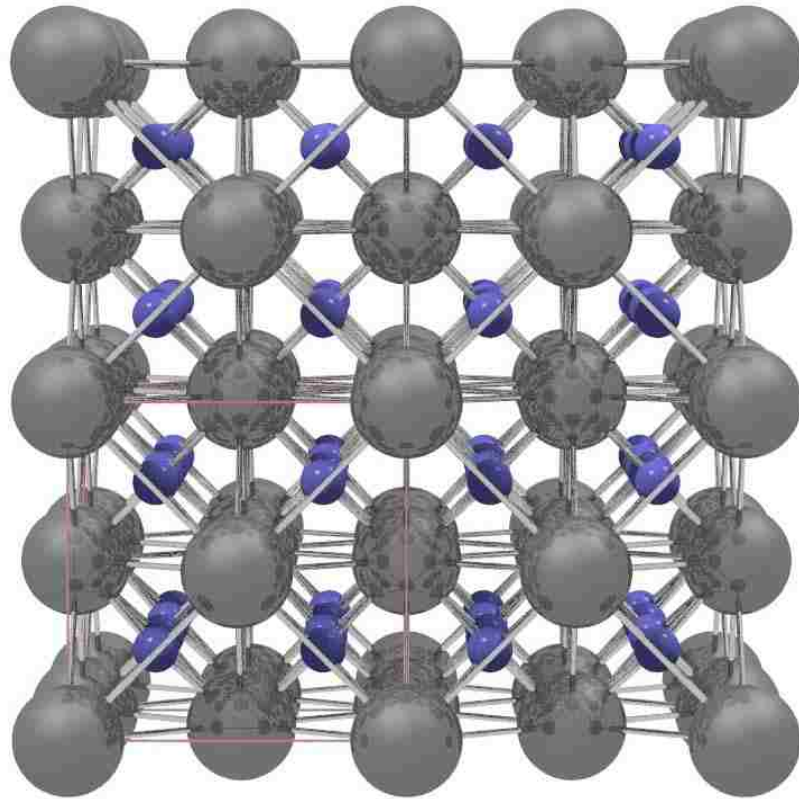


Figure 1.4 The $CaF_2$ structure with the unit cell outlined in red (lower left quadrant).

In $CaF_2$, the fluorine atoms are eight fold coordinated to the calcium atoms.  To arrive

at the C-type structure, anions are removed in pairs of two along the body diagonal and

face diagonal of the $CaF_8$ coordination cubes.[28]  This ordered removal of anions results in

the following changes: the cation coordination number changes from 8 to 6, the oxidation

state of the cation changes from $4^+$ to $3^+$, and the anions no longer sit on the corners of

their former primitive sub-lattice.   The anions, now situated on 48e general Wyckoff

sites as given by (x,y,z) in Table 1.3, are coordinated about the cations in distorted cubic fashion.

Figure 1.5 shows the resulting distorted $CaF_2$-type structure with the missing anions as hollow spheres. For clarity, wire-frame cubes are drawn around the centered cations as a reference to the primitive cubic sub-lattice formed by the fluorine atoms in $CaF_2$. It is clear that around the Ln1 cations ($S_6$ sites) the unoccupied anion positions are along the body diagonal and around the Ln2 cations ($C_2$ sites) the unoccupied anion positions are along the face diagonal.
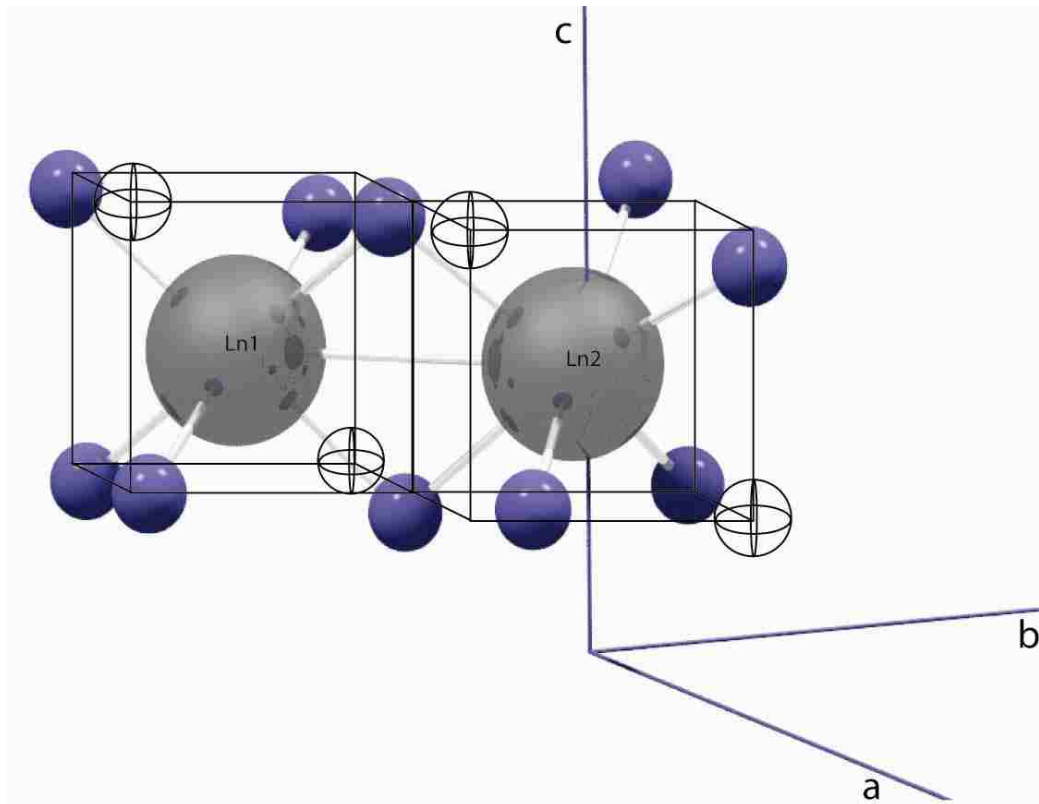


Figure 1.5 Removed section of the C-type structure showing the two crystallographically different rare-Earth sites.

## 1.4 Polymorphism in the Rare-Earth Sesquioxides

Like the rare-Earth metals, the physical properties of the rare-Earth sesquioxides are affected by the partial filling of their inner 4f-electron shells. The 4f-electrons do not participate strongly in bonding at ambient pressure; however, their effects on the structure a given rare-Earth will adopt are apparent. As the 4f-electron shell is filled, the nuclear charge screening provided by the 4f shell is lessened. The outer $5s^2 5p^6$ shells experience an increasing coulombic attraction towards the nucleus resulting in a steady decrease in ionic radii. This effect has long carried the name, the lanthanide contraction.[1]
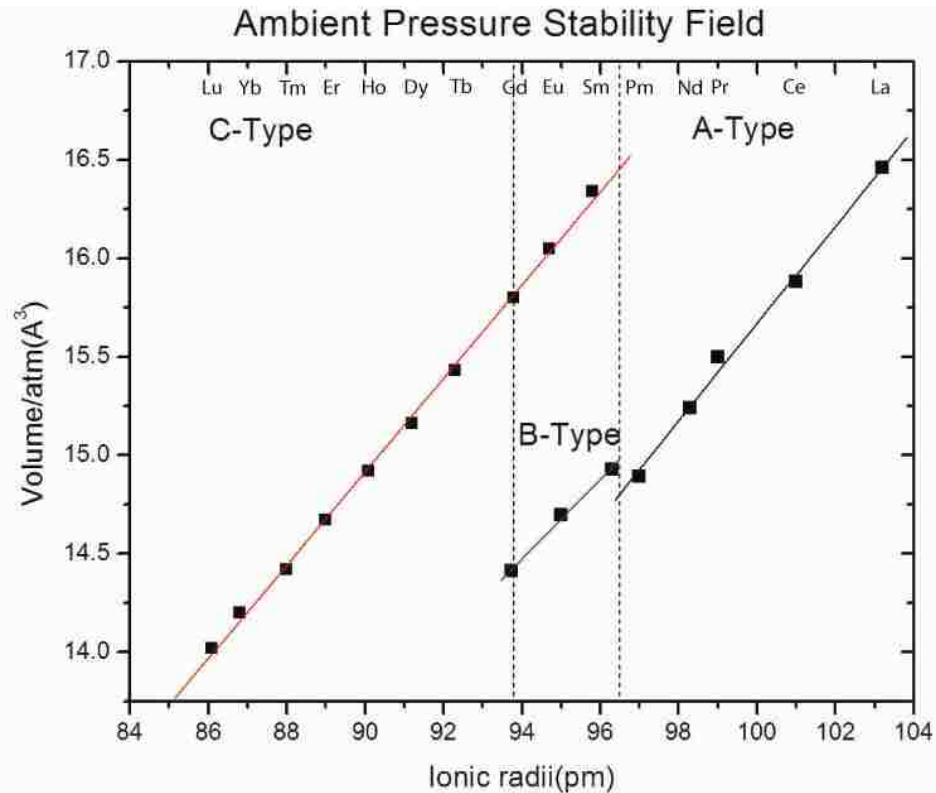


Figure 1.6 Relationship between atomic volume and ionic radii for the rare-Earth sesquioxide series. Atomic volumes are recorded from tables 1.1, 1.2.1, and 1.3. Ionic radii for the A and C-type are from reference [1]. Ionic radii for the B-type are from reference [17].

Figure 1.6 shows that the ambient pressure/temperature stability field is closely related to the radius of the $RE^{+3}$ cation which, in turn, is a function of the f-electron occupation number because of the lanthanide contraction. The regions where the C and A-types are preferred appear to the left and right of the two dotted lines respectively. The region between the dotted lines indicates where the B or C-type phases are stable. As the f-electron occupation number increases, the B and later C-type structures are stabilized in preference to the A-type. At elevated temperatures, the C-type structure is destabilized and will transform to either the A or B-type depending on temperature and the RE species.[18,29-31] Pressure tends to stabilize the A or B-type phase with respect to the C-type phase.[32] It is, therefore, expected that at elevated pressure, the temperature required to transform a given C-type structure to A or B-type would then be lower. Following this logic, the pressure/temperature phase diagrams should show a negative Clapayron slope.

Three different types of pressure induced structural phase transitions are observed at ambient temperature. The C-type structures can transform to B-type and is reversible only after long periods of annealing.[18, 33] The B-type structures can transform reversibly to the A-type via a first order displacive type phase transition accompanied by a 1-2% decrease in unit cell volume.[33] Lastly, the C-type structures can transform directly to the A-type via a first-order reconstructive type phase transition.[33] This C to A-type phase transition is irreversible and is accompanied by a ~8-10% change in unit cell volume.

Figures 1.7 and 1.8 are an account of all C → B and B → A-type pressure induced structural phase transitions reported in the literature at ambient temperature. The extension of the lighter portion of the bars indicates the maximum pressure achieved in each reported experiment. The hashed areas indicate the region of certainty to which the

phase boundary is thought to be known. I have included yttrium in this study do to its similarity to the rare-Earths. The individual rare-Earth species are ordered by increasing f-electron occupation number with yttrium being the exception. Yttrium's location in the plot was determined by its relative ionic radii with respect to the other rare-Earths.
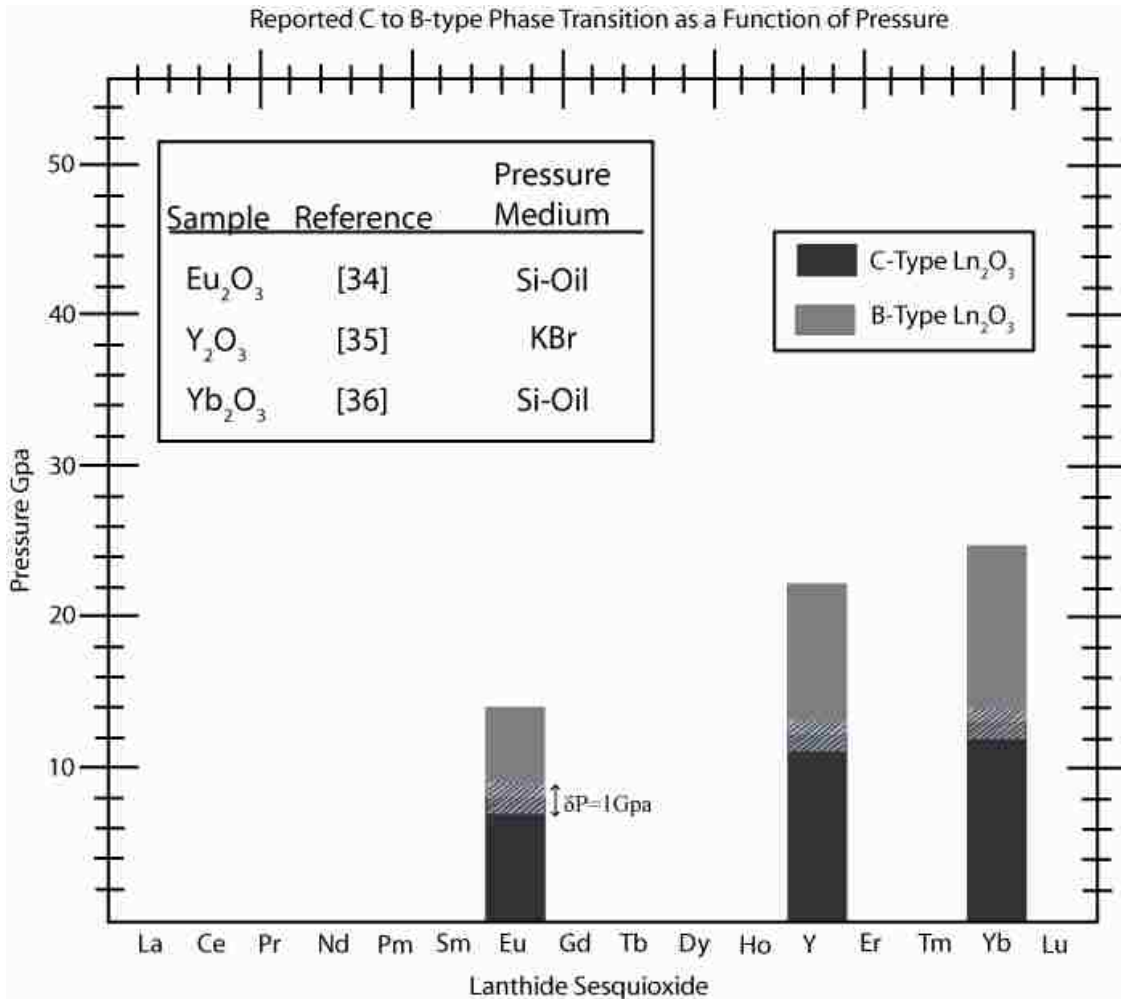


Figure 1.7 C to B-Type pressure induced structural phase transitions reported in the literature. Shown in the caption in the upper left are specific samples studied, the respective reference, and the pressure medium used in the experiment. The darker and lighter shaded portions of the bar graphs are representative of the C and B phases respectively.
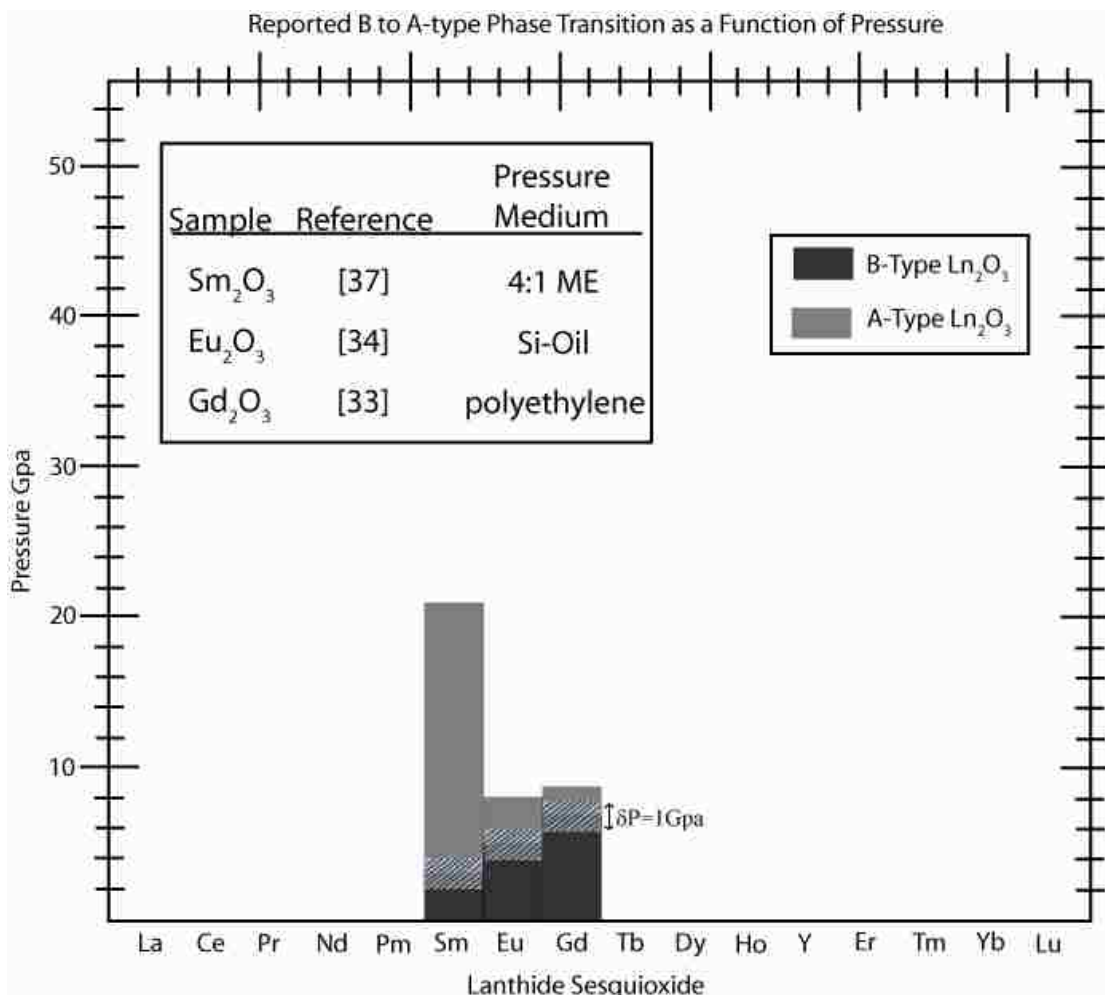
Figure 1.8 B to A-Type pressure induced structural phase transitions reported in the literature.  Shown in the caption in the upper left are specific samples studied, the respective reference, and the pressure medium used in the experiment.  The darker and lighter shaded portions of the bar graphs are representative of the A and B phases respectively.

In the present study, all C-type rare-Earth sesquioxides are observed to transform directly to the A-type with the exception of $Yb_2O_3$.  Figure 1.9 shows the only reported C → A-type phase transition occurring in the lanthanide series as $Gd_2O_3$.  It is worth noting that the pressure transmitting media used in all previous reported experiments are ones known to be far stiffer and support greater deviatoric stress than condensed gas pressure media, such as argon or nitrogen, used in the present case.
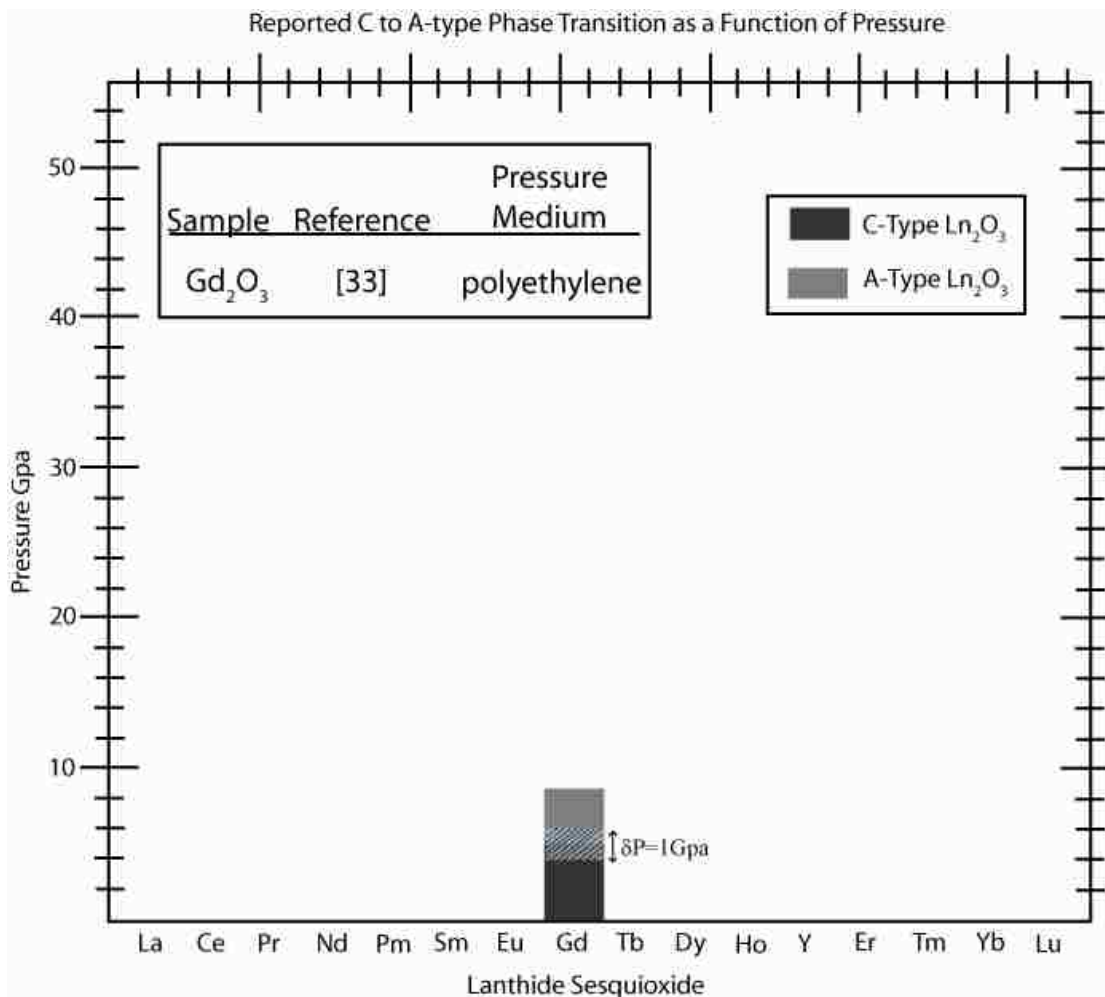
Figure 1.9 C to A-Type pressure induced structural phase transition reported in the literature for the rare-Earth sesquioxides.

## 1.5 Aims of This Dissertation

The first half of this dissertation focuses on the development of instrumentation used to perform optical spectroscopy from samples within diamond anvil cells (DACs), the theory used to model spectroscopic and x-ray diffraction data collected. In detail, I will discuss:

1. The experimental techniques I used to perform high pressure experiments in DACs.

2. The Raman and ruby fluorescence optical spectrometers I designed for this project.

3. The theory used to model optical spectra and x-ray diffraction data collected.

The second half of this dissertation focuses on a systematic study comprising many of the rare-Earth sesquioxides (RES) $RE_2O_3$ (RE=La,Sm, Eu, Gd, Er, Yb, Lu, and Y) where focus is paid to one in particular, $La_2O_3$. It is my intention to show by use of *in-situ* high pressure optical spectroscopy and X-ray diffraction techniques, that the polymorphic phase transition scheme, long known in the RES compounds, follows a different trend than was originally thought. In detail, I will show:

1) Evidence that the phase transition pathway from C-type RES compounds is directly to the A-type in the case of $RE_2O_3$ (RE= Sm, Eu, Gd, Er, Yb, Lu, and Y).

2) Evidence that the high pressure structure of A-type $La_2O_3$ is not stable above 4 GPa following a phase transition to a hexagonal super lattice and eventually to a distorted monoclinic structure.

CHAPTER 2

EXPERIMENTAL METHODS

This chapter discusses the instruments and light scattering techniques employed to create and subsequently to probe the high pressure conditions to which materials in this study are subjected.  In detail, I will discuss the diamond anvil cell (DAC), how it is used to generate a high pressure environment, and how these pressures are measured.  The details of how samples are prepared and loaded into the DAC will also be mentioned.  I will conclude with a detailed discussion covering the design of the Raman and ruby fluorescence spectrometers built for this work and the synchrotron X-ray facilities utilized to collect diffraction patterns.

## 2.1    Generation of High Pressure

Generating pressure in excess of 5 GPa or 50,000 times atmospheric pressure requires the use of very specific apparatus.  The only device that allows for easy optical access into the sample environment while at static high pressure is the DAC.  Two modifications the DAC were used in this study, one with a piston-cylinder design and one with a symmetric design.  Since the principals of their operation are the same, only the symmetric DAC will be described in detail here.

### 2.1.1    The Diamond Anvil Cell

The DAC was a invented though the joint efforts of Charles E. Weir, Alvin Van Valkenburg, Ellis R. Lippincott, and E. N. Bunting in the late 1950's and also

independently by John Jamieson.  The first high pressure publication using the DAC was

in 1959 by Weir *et. al*.[38]
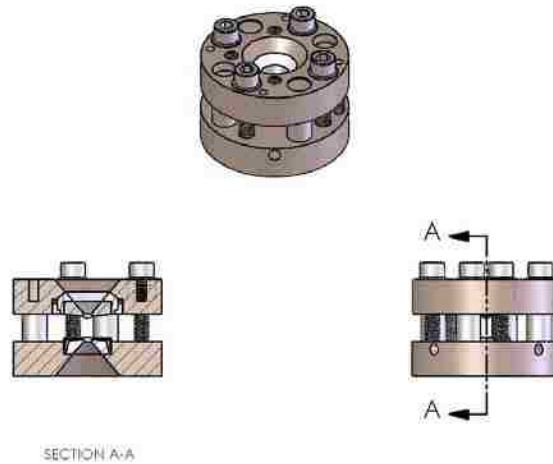


SECTION A-A

Figure 2.1 Cross-sectional and multi-angle view of the symmetric diamond anvil cell used in this study.  There a total of four guide pins and four counter rotating hex head compression screws.  The cell body is machined from hardened steel and the backing plates from either tungsten carbide or stainless steel.

Figure 2.1 is diagram of the symmetric DAC used in this study.  Mechanical load is

applied to tungsten carbide or hardened stainless steel backing plates through the cell

body via a set of four steel hex head screws.  Load from the backing plates is transferred

to the larger facet of the diamond anvil, the table.  The culet of the diamond, having the

smallest surface area, is the contact point between the anvils and the gasket.  Samples to

be pressurized are placed in a microscopic hole drilled in the gasket typically measuring

100 $\mu$m in diameter.  This drilled out hole becomes what is referred to as the sample

chamber and is ideally located at the center of the gasket.  Along with the sample, a

pressure medium, and pressure calibrant are loaded in the sample chamber for all the

present experiments.

The stress state acting on any continuous body, the sample in a DAC in this case, may be completely described in terms a second rank tensor called the stress tensor $\Sigma$. $\Sigma$ relates the force per unit area at a particular point on a body acting in a certain direction relative to a given surface normal vector. Listed as Equation 2.1, $\sigma_{ij}$ are the components of the stress tensor $\Sigma$ relating the force per unit area associated with the i'th normal vector acting in the j'th direction.

$$\Sigma = \begin{pmatrix} \sigma_{11} & \sigma_{12} & \sigma_{13} \\ \sigma_{21} & \sigma_{22} & \sigma_{23} \\ \sigma_{31} & \sigma_{32} & \sigma_{33} \end{pmatrix} \tag{2.1}$$

The diagonal components of the stress tensor $[\sigma_{11}, \sigma_{22}, \sigma_{33}]$ comprise the normal stresses and are compressive or tensile in type. The off diagonal components $[\sigma_{21}, \sigma_{32}, \sigma_{31}]$ are shear stresses. To better illustrate the relationship amongst the 9 components of the stress tensor and the respective coordinate frame in which they live, Figure 2.2 exemplifies this with respect to Cartesian coordinates.
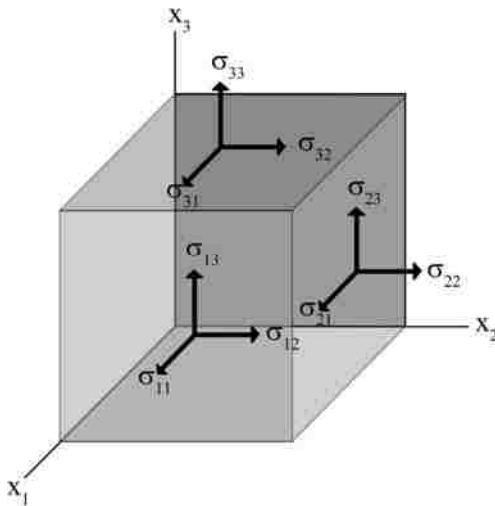


Figure 2.2 The stress tensor represented in Cartesian coordinates.

Mechanical load applied along the $x_3$ axis results in a stress $-\sigma_{33}$ at the sample. Here, the negative sign indicates a compressive stress or a positive pressure. The amount of stress, $-\sigma_{33}$, applied to the sample is controlled by fine tuning the load on the cell by turning a set of compression screws. However, mechanical load can only be increased to a maximum point where the diamonds no longer respond elastically. This is point is defined as the yield stress, $\sigma_Y$.

The yield stress is the stress point at which a material begins to plastically deform. In the case of diamond, these are irreversible deformations that mobilize dislocations in the lattice along certain crystallographic planes, called slip planes. When mechanical load is applied, the diamonds elastically deform in response to the stress. Elastic deformation, defined on terms of strain $\varepsilon$, will increase linearly as the stress in the diamonds increases until the yield stress is reached. For diamond anvils with flat non-beveled culets measuring 300 μm in diameter, pressures up to approximately 100 GPa[48] are achievable before plastic deformation occurs.

Metallic gaskets, used to confine the sample and support the diamonds during an experiment, are pre-indented using the DAC prior to drilling out the sample chamber. Pre-stressing the gasket work hardens the metal allowing higher pressures to be achieved and greater sample chamber stability. Additionally, lateral support for the diamonds is produced when plastic deformation of the gasket forces metal up around the crown of the diamond. For my experiments, the gasket pre-indentation thicknesses are stated for each experimental run and typical values of 50 μm (total indentation thickness) were used.

Once the sample is placed in the DAC, mechanical load is increased to the diamonds and the gasket will continue to thin out as its yield stress is again surpassed. Friction

between the gasket and the diamonds increases with $-\sigma_{33}$ and this helps to limit the amount of gasket material extruded laterally away from the center of the sample chamber. Elastic deformation of the anvils produces concave surfaces that "cup" the sample chamber further limiting the flow of the gasket material. In fact, the friction between the diamonds and the gasket is critical to the survival of the sample chamber as pressure is increased. If a small amount of foreign material were to coat the area between the gasket and diamond surface, even a small amount the sample being studied, a reduction in friction may result. This will allow the lateral extrusion of the gasket to rapidly increase with pressure. Typically, this is observed as the sample chamber "flowing" or moving to outward away from the center of the pre-indentation. Once this occurs, the experiment must be terminated or risk of contacting the diamonds becomes eminent.

In the present experiments, the sample chamber is filled with a pressure transmitting medium which surrounds the sample. The purpose of the pressure transmitting medium is to reduce the magnitude of shear stress components [$\sigma_{12}$, $\sigma_{23}$, $\sigma_{13}$], differential or deviatoric stress, and stress gradients produced in the sample chamber. In the presence of large shear stress, slip planes may be activated causing plastic deformation and unwanted or unintended structural phase transitions in the RES samples studied. Lattice distortion produced by the presence of deviatoric stress results in the broadening of x-ray diffraction peak profiles and misleading diffraction data interpretation. Stress gradients will also give rise to broadened x-ray diffraction peak profiles because the finite diffracting volume probed by the x-ray beam will contain a stress distribution and thus a strain distribution giving rise to a spread in lattice spacing.

The ideal pressure transmitting medium is one where $\sigma_{ij} = -p_o\delta_{ij}$ (where $\delta_{ij}$ is the Kronecker delta) for all pressures and $p_o$ is stress magnitude or hydrostatic pressure. This stress state is never fully realized because all fluids possess a finite viscosity and therefore support shear stresses. Furthermore, all pressure media that are fluid at ambient pressure will show increased viscosity at elevated pressure and eventually solidification. However, prior to solidification, if a fluid medium only weakly supports shear or deviatoric stresses relative to $p_o$ it is considered to be hydrostatic. Above the freezing point, there exists a useful pressure range where the shear and deviatoric stress components still remain small compared to $p_o$, called the quasi-hydrostatic range. Both the hydrostatic and quasi-hydrostatic pressure ranges vary depending on the medium and are selected with a particular pressure range in mind. Table 2.1 lists, in rank of increasing freezing pressure, the different pressure media used in the present experiments.

Table 2.1 Comparison of pressure transmitting media.

|  | Freezing pressure at 300K (GPa) | Pressure limit of quasi-hydrostatic behavior (GPa) | Reference |
|---|---|---|---|
| Ar | 1.2 | 9.0 | [44] |
| N2 | 2.5 | 13.0 | [40] |
| He | 11.8 | 50.0 | [55,56] |
| 4:1 M:E | 10.4 | 10.4 | [57] |
| 16:3:1 M:E:$H_2O$ | 14.5 | 14.5 | [57] |

2.1.2    Preparation and Method of Loading Samples

All samples in this study were of high purity 99.999% polycrystalline powders of the rare-Earth sesquioxides (RES) $RE_2O_3$ (RE=La,Sm, Eu, Gd, Er, Yb, Lu, and Y) provided

by the Sigma-Aldrich and Alfa Asera chemical supply companies. Prior to investigation, all samples were sintered at 1200 $^{o}$C for 8 hrs to drive off water and other trace impurities and then annealed at 700 $^{o}$C for 24 hrs. The annealing process helps to insure high temperature meta-stable phases formed during sintering are not present once the samples are cooled to ambient temperature. After annealing, samples are placed in desiccators to prevent re-adsorption of water.

Prior to loading the DAC, a sample chamber must first be constructed. Each sample chamber is unique to the particular experiment, and a new one must be created each time a high pressure experiment is performed. Sample chambers are formed by first pre-indenting a 9.5 mm diameter by 0.280 mm thick disk of rhenium metal, referred to as the gasket, with the DAC to a thickness of 50 μm. Within the center of this indentation, a hole of approximately 100 μm diameter is drilled out using an electric discharge machine. This forms a cylindrical sample chamber measuring 100 μm in diameter and 50 μm in thickness within the rhenium gasket. The gasket is then cleaned for 15 min in an ultrasonicator using distilled water as the sound transmitting medium. After cleaning, the gasket is then dried and carefully placed back on one of the diamonds in its previous location. A small amount of wax is generally used to stabilize the gasket during the loading process.

Approximately one third of the sample chamber is filled, at its center, with one of the polycrystalline RES samples. This corresponds to approximately 0.1 nL in volume. Several ruby spheres are then placed around the sample serving as pressure markers. A pressure transmitting medium of either condensed argon, nitrogen, helium, or a 4:1 mixture of methanol to ethanol is used to provide a quasi-hydrostatic environment while

samples are compressed. The cell is mechanically closed once the pressure transmitting

medium is introduced into the sample chamber and pressure is increased to about 1 GPa.
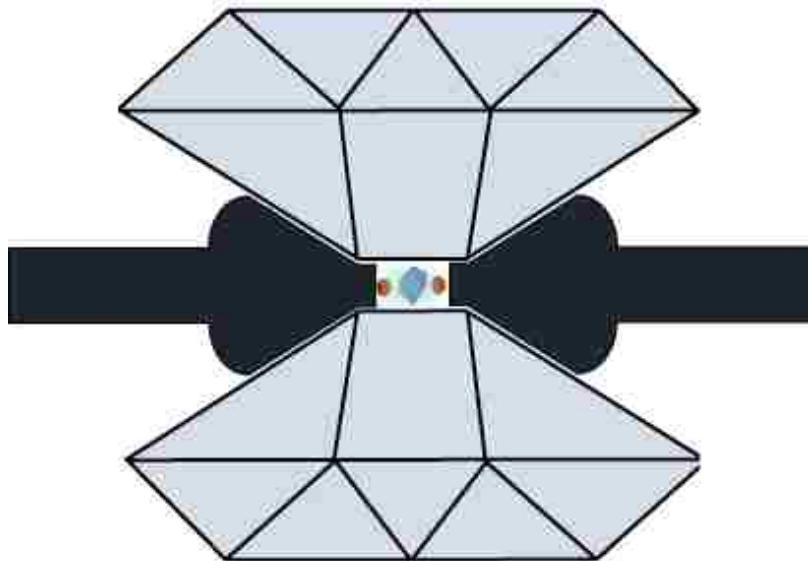


Figure 2.3. Enlargement of the diamonds, gasket, and sample chamber in a typical high pressure experiment.

Figure 2.3 is a detailed schematic of the diamonds, the pre-indented gasket, and the

sample chamber. Pictured within the sample chamber are two ruby spheres on either side

of the sample which is centered with respect to the gasket. For details on the cryogenic

loading of condensed gas pressure media, the reader is referred to one of Jayaraman's

papers.[39]

## 2.2 Measurement of Pressure

The DAC was not immediately recognized as a valuable scientific instrument at it's

time of discovery as no practical means of measuring pressure existed. The only means

of pressure determination was based on calculation of the force per unit area being

exerted on the diamonds by the loading device.  However, this proved to be quite

inaccurate for several reasons, however not limited to; unaccounted frictional effects,

plastic deformation of the gasket and sample, and elastic deformation of the anvils.  Use

of the pressure-volume equation of state of NaCl was substantially more accurate, though

at that time, powder diffraction measurements took nearly 15 hrs to obtain via a

conventional X-ray source.  It was not until 1971 that S. Block, D. Barnett, G. Piermarini,

and R. Forman began to investigate the fluorescence spectra of various materials as a

function of pressure.  $Cr^{3+}$ doped $Al_2O_3$ (ruby) showed the greatest change in emission

wavelength with increasing pressure and was later shown in a publication by Piermarini

to be linear up to 20 GPa in good approximation.[40]

Piermarini's approach to calibrating the observed wavelength shift in the fluorescence

lines in ruby is based on the calculated equation of state of NaCl as developed by Decker

in 1965.[41]  The results of Decker's calculated equation of state for NaCl are in agreement

with experimentally determined results by Bridgman and from that of high-pressure high-

temperature shock data.[42]  The agreement in the calculated equation of state to

experimental data is approximately 3% for pressures up to 30 GPa.  The validity of the

Decker equation of state is also realized through comparison of known phase transition

pressures of Ba I-II and Bi II-IV occurring at 5.5 and 7.6 GPa respectively.  These fixed

point phase transitions are seen to be in agreement with the Decker equation of state to

within 3%.

Piermarini's pressure scale is derived from an experiment where the change in lattice

constant of NaCl is observed through powder X-ray diffraction methods as load on a

DAC is increased.  As load is increased, the wavelength shift of the $R_1$ fluorescence line

in ruby is measured. Decker's equation of state is then used to obtain the pressure in the sample chamber based on observed unit cell volume changes in NaCl. The resulting fit for the shift of $R_1$ fluorescence line ($\Delta\lambda$ in angstroms) as a function of pressure (P in kbar) is shown in Equation 2.2. This pressure scale is used for all measurements up to 5 Gpa or 50 kbar in this study.

$$P(kbar) = 2.740 \pm 0.016 \cdot \Delta\lambda_{R1}(angs) \qquad (2.2)$$

In 1977, Mao, Bell, Shaner, and Stienberg extend the ruby fluorescence pressure scale to 100 GPa.[43] This new scale is generated much in the same way as the Piermarini scale except reduced shock wave equation of state data was used in place of the Decker equation of state to measure pressure. The observed shifts of the ruby $R_1$ line as a function of pressure are then fit to a non-linear function.

$$P(Gpa) = \frac{1904}{B} \cdot \left[ \left( \frac{\lambda_p}{\lambda_o} \right)^B - 1 \right] \qquad (2.3)$$

Equation 2.3 is the Mao-Bell pressure scale where B is equal to 5 for non-hydrostatic measurements[43] and 7.66 for quasi-hydrostatic measurements.[44] The wavelength of the $R_1$ line measured at ambient and elevated pressure is represented by $\lambda_o$ and $\lambda_p$ respectively. The reported error in this scale is about +/-5% using the above stated values for B in the pressure range of 6-100 GPa. The most recent cross-calibration of the ruby scale involving reduced shock wave equation of state data has the value of B=9.5 with reported uncertainties at +/-2% for pressures below 55 GPa and +/- 4% at 100 GPa.[45]

It must be born in mind that this is not an absolute pressure scale, rather a cross calibration of the observed pressure induced shift in wavelength of the $^2E$ states ($R_1$ and $R_2$ emission lines) in ruby to shock compression P-V equation of state data, where the

pressure is assumed to be known at a given density.  Additionally, this pressure scale is

implemented at 300K whereas shock compression data are recorded at much higher

temperatures and reduced to 300K which inevitably introduces error in the P-V equation

of state data.  As more accurate equation of state data are produced, the reported

pressures for a given experiment based on a particular ruby scale will necessarily change.

Pressures reported in the range between 0.1 GPa and 5.0 GPa were determined using the

Piermarini pressure scale listed as equation 2.2.  Pressures reported above 5.0 GPa were

determined using the Mao-Bell scale with B=9.5 as listed in Equation 2.3.

The measurement of pressure in a DAC using the ruby fluorescence technique

requires an optical spectrometer designed both to excite the R-line fluorescence and

simultaneously to collect the emitted light.  The excitation source must be chosen with a

particular pumping scheme in mind.

Two optical absorption bands in ruby, labeled U and Y, occur in the visible part of the

spectrum.  The U and Y bands have a peak optical absorption near 18,215 $cm^{-1}$ (549nm)

and 24,814 $cm^{-1}$ (403nm) respectively.  Optical excitation into the U or Y bands is

followed by rapid decay through non-radiative transitions to the $^2E$ states.  Radiative

emission from the $^2E$ states to the electronic ground state give rise to the $R_1$ and $R_2$

emission lines.

The origin of the $R_1$ and $R_2$ emission lines comes from the splitting of the 5-fold

degenerate $3d^3$ electronic states in the $Cr^{3+}$ atom from crystal field and spin-orbit

perturbations.  The degenerate d-electron states are first split be the strong cubic crystal

filed giving rise to the $e_g$ and $t_{2g}$ eigenstates.  The basis functions for the $e_g$ doublet and $t_{2g}$

triplet are $\{z^2, x^2-y^2\}$ and $\{xy, yz, xz\}$ respectively.  Smaller trigonal field and spin-orbit

perturbations further split the $e_g$ and $t_{2g}$ levels giving rise to the $\{^2E, \,^2T_2\}$ and $\{^2T_1, \,^4T_2, \,^4T_1\}$ states respectively.[46]  Figure 2.4 shows the energy level diagram for $Al_2O_3{:}Cr^{3+}$.



| Cubic Field Terms | Eigen-state | Transition to ground state | Energy (cm⁻¹) |
|---|---|---|---|
| $^4T_1$ | $^4A_2$ | Y | 25200 |
| | $^4E$ | | 24400 |
| $^2T_2$ | $\bar{E}_b$ | $B_3$ | 21360 |
| | $\bar{E}_a$ | $B_2$ | 21070 |
| | $2\bar{A}$ | $B_1$ | 21000 |
| $^4T_2$ | $^4A_1$ | U | 18450 |
| | $^4E$ | | 18000 |
| $^2T_1$ | $\bar{E}_a$ | $R'_1$ | 15190 |
| | $2\bar{A}$ | $R'_2$ | 15170 |
| | $\bar{E}_b$ | $R'_3$ | 14960 |
| $^2E$ | $2\bar{A}$ | $R_2$ | 14430 |
| | $\bar{E}$ | $R_1$ | 14400 |
| $^4A_2$ | | | 0 |
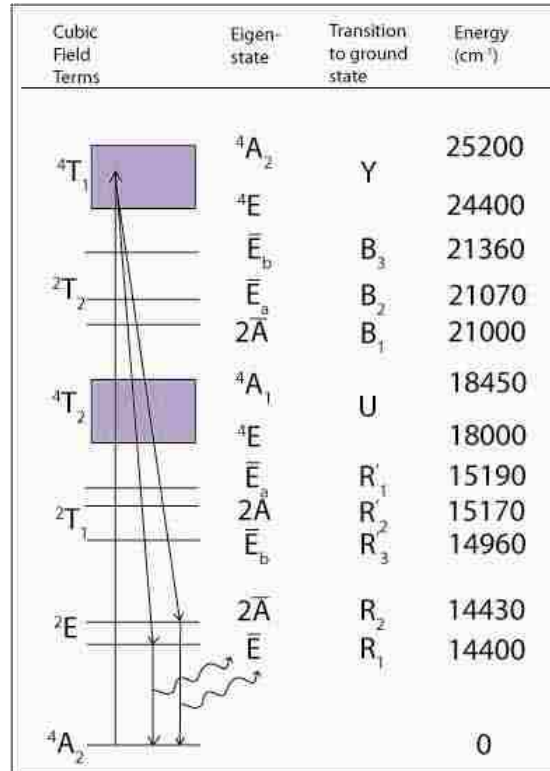
Figure 2.4. Electronic energy diagram for $Al_2O_3{:}Cr^{3+}$.  The arrows outline the pumping scheme used in all 'in-house' pressure measurements.  The cubic crystal field terms are subsequently split by smaller trigonal field and spin-orbit perturbations to the free ion energy levels.[46]

## 2.3   Spectroscopic Apparatus Developed

This research project prompted the design of two optical spectrometers.  One

spectrometer was designed for measuring pressure (ruby fluorescence) and the other for

collecting Raman scattered light from within a DAC.  Both spectrometers share certain

optical design characteristics that are unique.  Given the relatively small sample sizes

DAC's afford, usually 100 μm in diameter by 50 μm in thickness, a microscope must be

implemented in the design allowing samples to be optically located.  Special long

working distance objectives are also required because the separation between sample

chamber and DAC body usually exceeds that of most common objectives.  Optical spatial

filtering techniques are used to reduce the amount of Rayleigh scatter and luminescence

emission from the diamonds and other parts of the sample chamber from entering the

spectrometer.    This is especially the case when performing Raman spectroscopic

measurements.

### 2.3.1    Ruby Fluorescence/Absorption Spectrometer

All pressure measurements done at UNLV were made with an optical spectrometer

using a 50 mW, 405 nm diode laser to pump the 'Y' absorption band in ruby.  A 300 mm

focal length Acton SpectraPro 2300i spectrograph is used to disperse light onto a

Princeton Instruments Peliter cooled CCD spectroscopic camera.  The SpectraPro 2300i

monochromator uses a Cherny-Turner type light dispersion geometry.  Equipped with a

1200 grove/mm grating blazed at 550nm, the monochrometer produces a resolution of

0.05nm.  All wavelength calibrations are done with PenRay calibrated lamps from Oriel.

The monochromator's source optics, shown in figure 2.5, are designed to allow two

different types of optical spectroscopy to be performed.  The tungsten lamp, shown in the

upper left corner of figure 2.5, serves as a broad band source for which absorption

spectroscopy can be done.  A reference spectrum from the lamp is collected from a 90/10

(transmittance/reflectance) beam splitter and collected at one of two ends on a bifurcated

fiber optic cable.  The remaining 90% of light from the source is focused by a series of

optics to a point inside the DAC.  A Mitutoyo long working distance infinity corrected

objective is used to image the sample and gather the transmitted light from the tungsten lamp.  The first lens after the objective, called the tube lens, produces an intermediate image at the tube lens's focal point.  A 50/50 beam splitter positioned after the tube lens creates two identical optical paths traveling in orthogonal directions.  One path serves as a visual reference line and the other a spectroscopic line.

The light path transmitted by the beam splitter is used as the visual reference line.  At this line's intermediate image plane is a calibrated reticle.  The second lens in this line, called the projection lens, is used to project both the image of the sample and that of the retical onto the CCD camera situated at the final image plane.

The light path reflected by the 50/50 beam splitter is used as the spectroscopic line.  Unlike the reference line, there is nothing at the position of the intermediate image plane.  At the focal plane produced by the spectroscopic line's projection lens is a 500 μm mounted pinhole.  Projected onto this pinhole is an exact copy of the image projected on the TV camera minus the retical.  Both pinhole and reticle are mounted in two-dimensional micro-adjuster stages allowing their central positions to be changed in the plane orthogonal to the optical axis.  The center of the reticle and that of the pinhole are adjusted until they are coincident.  Only light which makes through the pinhole is focused onto the second end of a bifurcated fiber optic cable.  The user now observes, via the CCD camera's output, a reference to what the monochromator is to be sensing.

When operating in absorption mode, light from both the tungsten lamp's reference line and that from the source optic's spectroscopic line are imaged onto the slits of the monochromator.  These images are then dispersed through the monochromator forming

33

two independent spectra.  By computing the logarithm the reference line divided by the transmitted line, one can determine absorbance.

When this system is in fluorescence microscopy mode, the tungsten lamp is used for diascopic illumination of the sample.  Radiation from a 405 nm Power Technology diode laser is brought to a 10 μm diameter focused spot on the sample by the Mitutoyo objective.   When a 20X objective is used, this system produces an optical magnification of approximately 50X.  The increase in magnification is produced by the additional optics following the objective.  The 500 μm diameter pinhole is imaged as a 10 μm aperture on the sample when reverse ray traced.  This means that only a 10 μm diameter circular portion of the image on the pinhole is transmitted to the spectrograph.  This allows for optical selectivity of individual ruby pressure markers within the sample chamber.


### 2.3.2    Micro-Raman Spectrometer

Raman spectroscopy is an important spectroscopic technique used in this study to probe changes in crystallographic symmetry as a function of pressure.   Raman spectra originate in the electronic polarization induced by the oscillating electric field of an incident monochromatic light source.  If monochromatic light of frequency $\nu$ is incident on a material, then, because of fluctuations of the electronic polarization induced in the material, light of frequency $\nu^{\dagger}$ (Rayleigh scattering) as well as $\nu+\nu_i$ and $\nu-\nu_i$ (Raman scattering) is emitted.  In this notation, $\nu_i$ is a vibrational frequency in the material being studied.

---

[†] The frequency of the Rayliegh scatter is actually Doppler broadened be thermal vibrations which results.

Tungsten Lamp
Aperature Stop
90/10
Fiber Optic Collimator
Bifurcated Fiber
SpectraPro 2300i
CCD Camera
500um Pin Hole
50/50
20X Mitutoyo
DAC
50/50
50/50
Light Pipe
Reticle
TV Camera
50mW 405nm Diode Laser
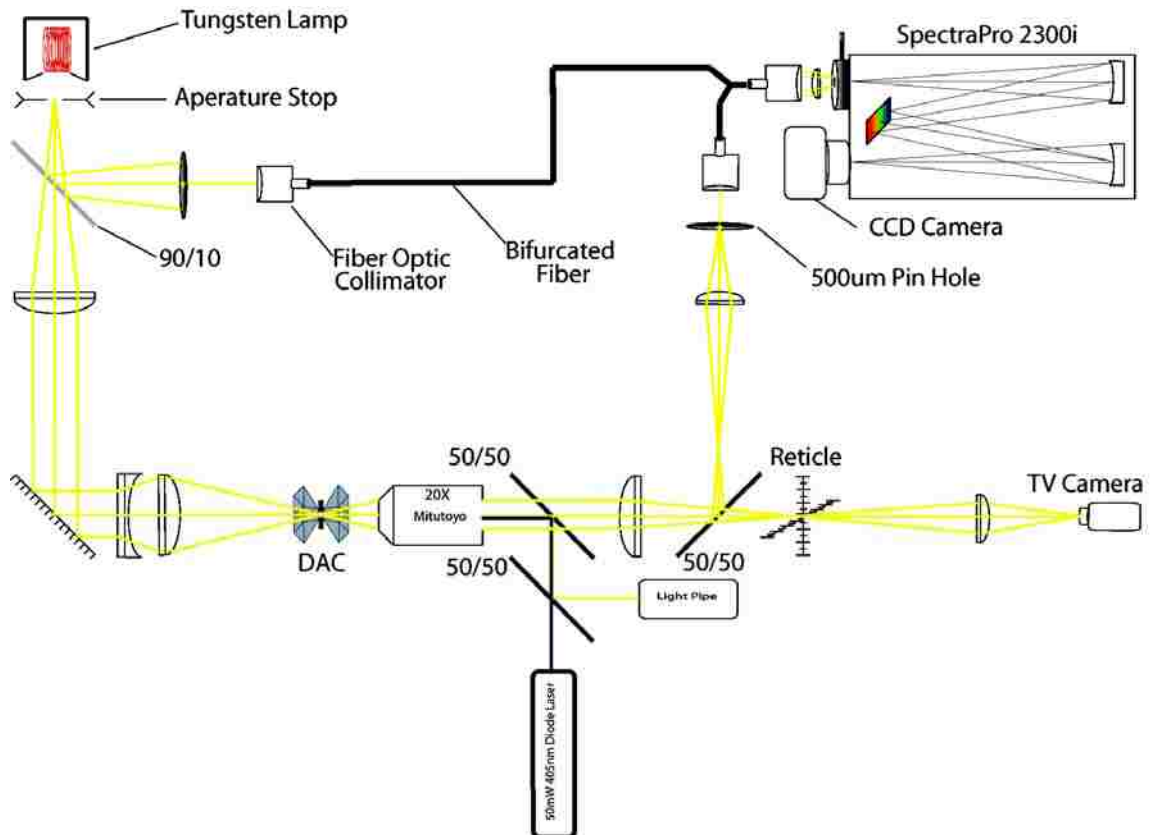
Figure 2.5. Spectrometer used for all 'in house' ruby pressure measurements. Originally this system was designed for conducting *in-situ* high pressure optical absorption spectroscopy and later modified so that ruby fluorescence spectroscopy would be possible.

Figure 2.6 is a diagram of the Raman effect. Excitation from the electronic and vibrational ground state to virtual states, far below that of the first electronic excitation, and subsequent de-excitation to the first excited vibrational state v=1 is referred to as Stokes Raman scattering. Excitation from the electronic ground state and first excited vibrational state to a virtual state followed by subsequent de-excitation to the vibrational ground state is referred to as Anti-Stokes Raman scattering.[47]

The Raman effect samples zone center phonons whose energies range from 10 to $10^4$ cm$^{-1}$. Raman shifted photons are therefore very close in energy to the excitation source which necessitates the need for edge or notch filters to block the elastically scattered light

(Rayleigh scatter) after interaction with the sample.  Even though the Raman effect is a

factor of $10^3$ to $10^4$ times weaker than Rayleigh scattering, it is observable from nano-

liters of material within a DAC if special considerations are made with regard to the

experimental setup.

   A schematic of the micro-Raman spectrometer designed for these experiments is

shown in Figure 2.7.  A Lexel 95 argon-ion laser's 488 nm line is used as the excitation

source.
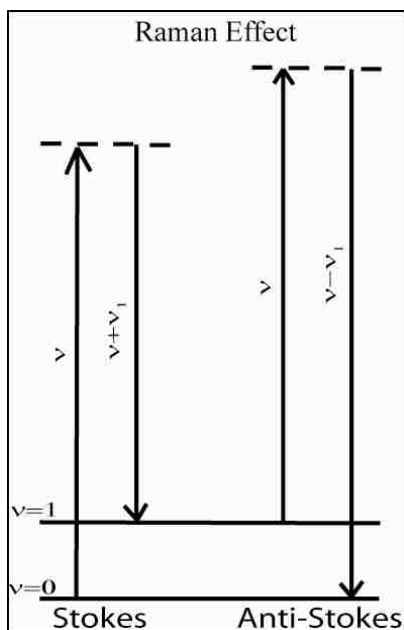


Figure 2.6. Simplistic diagram of the Raman effect.  The dotted lines represent the virtual
excited state.  In this case the excitation source is far below that of the first electronic
excited state.

   A Kaiser Optics holographic band pass filter is positioned to diffract the 488 nm line

90 degrees to the incident beam direction.  The $Ar^+$ plasma lines, which diffract at

different angles, are subsequently blocked by the first aperture.

A spatial filter is built using a 10X Newport microscope objective having a numerical aperture (N.A.) of 0.25 with a 15.8 mm focal length, a 20 µm Mo pinhole, and a 100 mm focal length plano convex lens labeled L1 in figure 2.7. The spatial filter acts as a high frequency noise filter by producing the Fourier transform of light from the laser cavity at the plane of the pinhole. At this plane, called the transform plane, light of increasing frequency appears at higher radial distances from the optical axis. High frequency noise is then reduced by placing a pinhole of appropriate size at the objective's image plane. The optimum pinhole diameter, $D_{opt}$, should be equal to the distance of first minimum in the Airy pattern produced at the image plane of the objective as given by equation 2.4. At this point, the pinhole will be passing approximately 84% of the incident laser power.

The constants, $\lambda$, N.A., and 'a' are the wavelength, effective numerical aperture, and incident beam width respectively. Using 488 nm for $\lambda$ and 0.032 as the effective N.A. of the objective accepting a 1 mm diameter beam, an optimum pinhole diameter of 18.6 µm is calculated.

$$D_{opt} = \frac{1.22\lambda}{N.A.} = \frac{2.44\lambda f}{a} \qquad (2.4)$$

Lens L1 is placed so that its focal point coincides with that of the microscope objective's focal point and serves to re-collimate and expand the beam approximately 6.4 times its original width. The relationship between initial and finial beam widths ($w_i$, $w_f$ respectively) as a function of the focal lengths 1 and 2 ($f_1$, $f_2$ respectively) are shown in Equation 2.5. Because the beam's width and divergence $\phi$ are inversely

$$w_f = \frac{f_2}{f_1} w_i \qquad (2.5)$$

proportional, this also results in a 6.4 times reduction in beam divergence as shown in Equation 2.6. This allows the beam to propagate the distance needed to reach the DAC while maintaining adequate collimation.

$$\phi_f = \frac{w_i}{w_f} \phi_i \tag{2.6}$$

A long focal length lens for L2 (100 mm) is needed to prevent collisions between the objective, L2's lens mount, and the DAC. However, as Equation 2.4 states, the size of the focused beam is directly proportional to focal length and inversely to beam diameter.

Because the Raman effect is seen about once for every $10^6$ photons that interact with the sample[47], a tightly focused beam is required to produce a fluence rate (J/s/m$^2$) high enough to record a meaningful Raman spectrum. Given the incident beam's expanded width is now 6.4 mm, equation 2.4 yields a focused spot size of approximately 18.6 μm which produces a fluence rate (assuming 20mW power on the sample) on the order of $10^7$ J/s/m$^2$ which is high enough to obtain quality spectra.

A 10X Mitutoyo long working distance microscope objective is used to gather light scattered from the sample at 30 degrees relative to the incident beam. This is in contrast to typical 180 degree backscattering geometry[39,48] where the specular reflection of the laser from the table of the diamond is entering the optical path of the monochromator. This geometry reduces the amount of unwanted elastically scattered light from entering the monochromator.

Following the Mitutoyo objective is the tube lens, labeled L3, which forms an intermediate image at the aperture stop for the eyepiece used in visual alignment of the sample. L3 has a focal length of 200 mm and in combination with the Mitutoyo objective, of focal length 20 mm, an image with a magnification of 10X is produced at
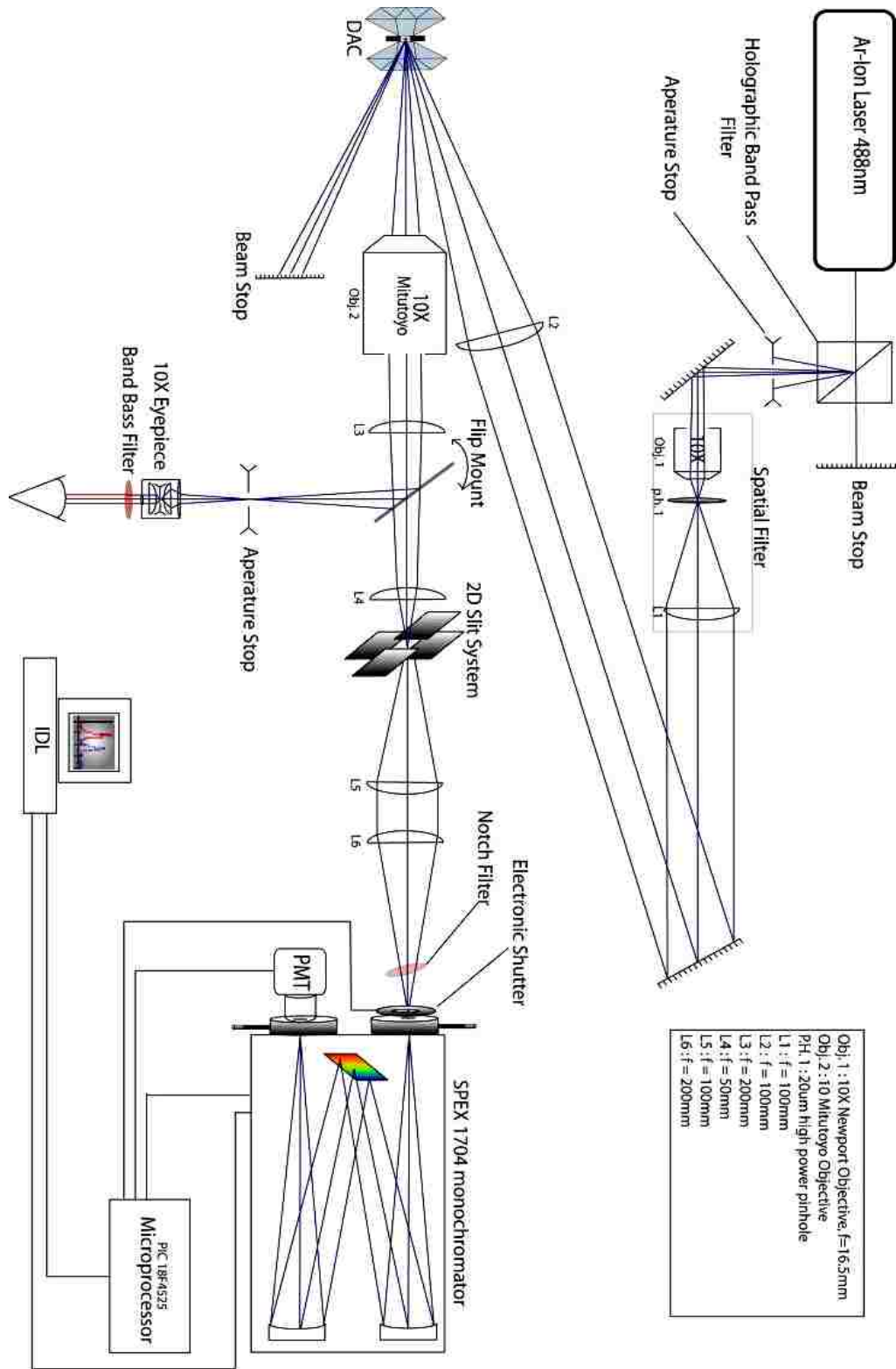
Figure 2.7 Optical layout for the micro-Raman spectrometer.

the aperture stop for the eyepiece. The magnification at the intermediate image plane is given by ratio of the focal length of the tube lens to that of the objective. The final magnification as seen by the observer through the eyepiece is given by the product of the magnification of the objective/tube lens combination and that of the eyepiece, and is 100X.

The combination of L3 and L4 form an image of the sample at the position of the 2D-slit system with a magnification of approximately 3X. The region of interest that is to be sampled by the monochromator is set via adjusting the size of the aperture formed by the 2D-slit system. Lens L5 re-collimates the light passing through the 2D slit system to a width of approximately 20 mm.

This optical setup is the basis for all confocal microscopy. Light gathered by an objective is focused onto an aperture, re-collimated, and focused onto the entrance slits of a monochromator. This design has the advantage of providing the user with the ability to not only select a region within the DAC that is of spectroscopic interest but also prevents light from other positions along the optical axis from entering the monochromator. In the case of all Raman scattering experiments using a DAC cell with 488 nm excitation, there will be fluorescence from the diamonds that will enter the monochromator, unless blocked by a confocal aperture such as the one described here.

Figure 2.8 details how the micro-Raman spectrometer functions as a confocal optical system. Light that is in focus at the sample is also in focus at the 2D slit system, represented in Figure 2.8 by a pinhole for convenience. By adjusting the size of the aperture formed by the slits, the spatial extent and depth sampled by the spectrometer is controlled. In the present case, the displaced scattering layer is the diamond anvil itself

which produces broad band fluorescence when excited by a 488 nm source. This confocal setup allows the gathering of Raman scattered light that has a significantly reduced amount of unwanted fluorescence, Rayleigh, and Raman scattered light originating from the diamonds. This results in a cleaner Raman spectrum from the sample to be recorded.

Figure 2.9 is a detailed ray trace analysis of a lens system comprising a 20 mm focal length objective lens, L3, L4, and a 250x250 μm square aperture serving as the 2D slit system or the confocal aperture. Light is increasingly blocked by the aperture as the object plane for the objective lens is displaced in the direction towards the lens. When the object plane is located 2 mm in front of the original sample plane, nearly all of the light is blocked by the aperture. This demonstrates how scatter coming from the diamonds or any other position along the optical axis blocked by the confocal aperture. Greater spatial resolution is obtained by closing down the aperture farther which decreases the effective optical volume accepted by the system, however, at the expense of signal throughput.

The two remaining optics in the lens system L5 and L6 serve to re-collimate the light passing through the 2D slit system and focus light onto the entrance slits of the monochromator respectively. The focal length of lens L5 is 100 mm and is chosen such that the collimated beam width produced is approximately 20 mm in diameter.

Using a 200 mm focal length lens for L6 gives a working f/# of f/10 which is slightly larger than the monochromator at f/8. Operating the monochromator at a higher f/# under fills its optics, reducing the probability of stray light scattering within the monochromator.

Finally, a Kaiser Optics Super Notch Plus filter is used to block the Rayleigh scattered light from entering the monochromator. This multi-layered interference filter produces an attenuation of approximately 5-6 orders of magnitude at 488 nm +/- 2.5 nm. This
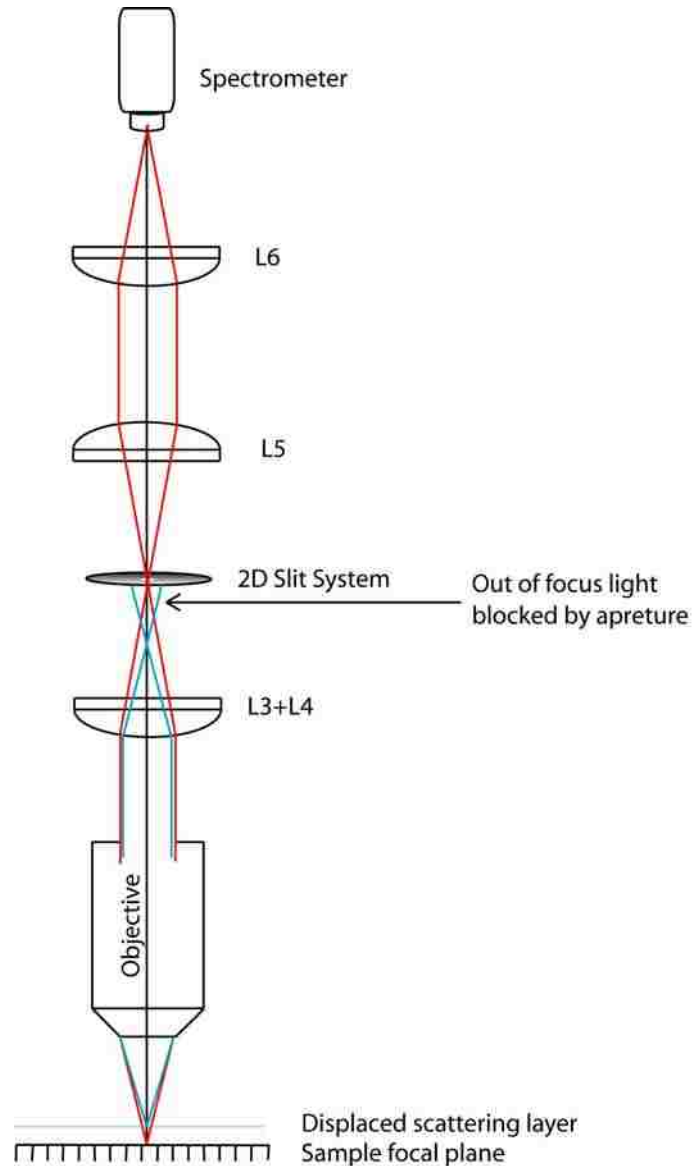


Figure 2.8 Confocal setup of optics on the micro-Raman spectrometer. Refer to Figure 2.7 for focal lengths of lenses in this diagram.

ultimately limits the low frequency range available to the monochromator to above approximately 100 cm$^{-1}$ relative to 488 nm.

The monochromator used in this experiment is a SPEX 1704 1 meter focal length f/8

Czerny-Turner monochromator equipped with a ruled 1200 groove/mm diffraction

grating blazed for maximum efficiency at 500 nm.  This gives the monochromator a

linear dispersion of approximately 0.8 nm/mm at the blaze wavelength.  The entrance and

exit slits are always set to equal values ranging from 50-100 μm.  This gives the

instrument a spectral band pass of 0.04-0.08 nm or 1.67-3.5 cm$^{-1}$ relative to 488 nm.  A

Peltier cooled Hamamatsu R928 Photo Multiplier Tube (PMT) is used as a single point

detection device.  The temperature on the PMT is locked at -40$^{o}$C for all experiments

giving a dark count less than 1 s$^{-1}$ for cathode voltage of -1 KV.
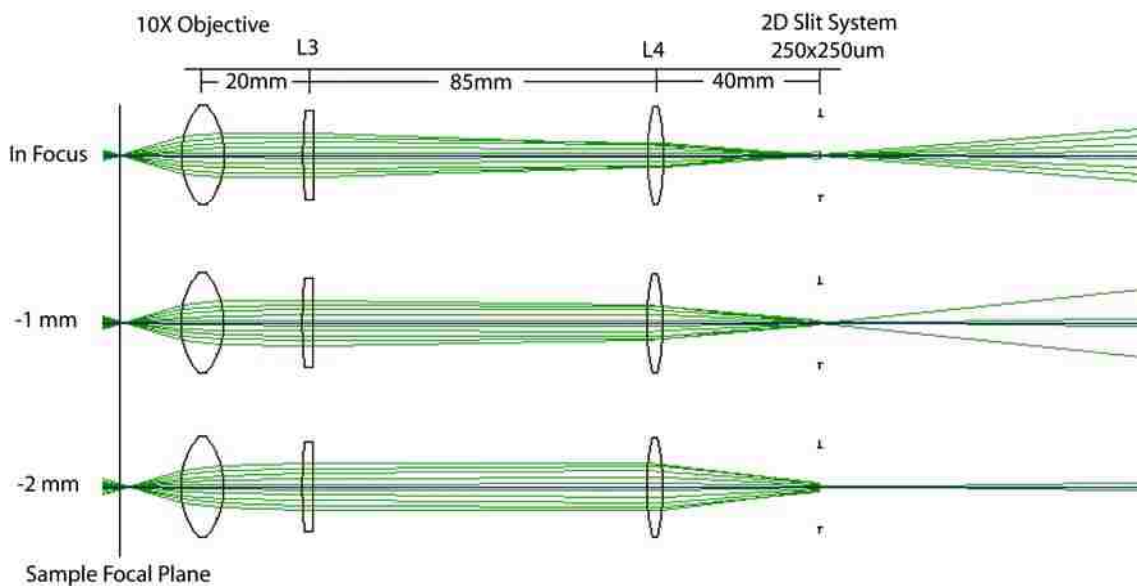


Figure 2.9 Ray trace analysis of the light gathering optics for the micro-Raman
spectrometer.

Control of the spectrometer is accomplished via the joint efforts of the SPEX CDA2

control interface and a PIC18F4525 microprocessor.  The CDA2 is designed to accept

commands via RS-232 communication protocol and has the primary function of

controlling the linear sine drive on the SPEX 1704 monochromator.  ASCII commands

sent to the CDA2 allow parameters for a wavelength scan to be setup.  The PIC18F4525

microprocessor, also accepting commands via RS-232, handles photon counting,

monochromator shutter control, and instructs the CDA2 when to advance to the next

wavelength position during a scan.  Basically, the wavelength rage and step width are

setup by the CDA2 and control is then handed over to the PIC18F4525.  Firmware

programming for the PIC18F4525 is written using PICC, a C language designed

specifically for embedded systems like the PIC series microprocessors.  A software

control interface written in IDL handles communication between the PIC18F4525 and the

CDA2 allowing the user full control over the monochromator via a graphical user

interface.  Figure 2.10 is a layout of electronic circuitry designed for this system.

## 2.4   X-Ray Diffraction Techniques

All X-Ray diffraction experiments included in this study were performed at one of

three synchrotron facilities.  Sector 16 (HP-CAT) at the Argonne National Lab, stations

16ID-B and 16BM-D, are utilized to perform angular dispersive and energy dispersive x-

ray diffraction respectively.  The CHESS (Cornell High Energy Synchrotron Source)

station B2 is also used to perform angular dispersive x-ray diffraction.  Lastly, the PAL

(Pohong Accelerator Laboratory) station 5A in Pohong Korea is used for high resolution

diffraction experiments on $La_2O_3$ and $Sm_2O_3$.

Powder x-ray diffraction is used as the primary technique for determining the structure

of materials at high pressure in this study.  There are many sources that cover the basics

of the techniques used and several to which the reader is referred.[49,50]  Some key points,

Figure 2.10 Control circuitry for the Raman spectrometer.

for clarity sake, need to be mentioned here to aid the understanding of the following chapters.

In an x-ray diffraction experiment, angles between diffracted rays and the incident beam (2θ) are measured to yield the spacing between lattice planes in a crystal ($d_{hkl}$). Given Bragg's law, equation 2.7, we have a simple relationship between diffracting angle 2θ, lattice plane spacing $d_{hkl}$ (hkl- Miller Index for particular lattice plane), and the wavelength of the incident radiation λ. Bragg's law is a consequence of the periodicity of the lattice; however, it gives no information regarding the associated basis of atoms with every lattice point. As will be shown; the composition of the basis determines the relative intensity of the various Bragg reflections.

$$2\,d_{hkl}\sin(2\theta) = n\lambda \tag{2.7}$$

Traditionally, a multi-circle goinometer is used to position the sample at the center of all circles of rotation and a point detector is scanned along a particular circle. For all experiments at HPCAT's ID-B and the CHESS B2 station, 2 dimensional image plate detectors are used to acquire cross-sectional images of diffracted light. This requires one to know precisely the distance from the scattering center, i.e. the sample, to image plane center, Δ. The radial distance, r, a diffracted ray strikes the detector is easily determined knowing the physical size of the image plate's pixels and the detector center coordinates. The Bragg angle of any diffracted ray can then be determined by equation 2.8.

$$2\theta = \tan^{-1}\left(r/\Delta\right) \tag{2.8}$$

Accurately determining Δ and ensuring that the sample, which is inside of a DAC, always remains at the same location in space is now the problem we must solve. First, to determine Δ, a diffraction pattern from a material with known lattice plane spacing, such

as $CeO_2$, Si, NaCl, etc is collected from a capillary or thinly pressed pellet. Because the lattice plane spacings $d_{hkl}$ are known along with the wavelength of the x-ray source, the angles of all diffracting rays are calculable. From each diffracting angle measured, a value for $\Delta$ is calculated by observing the radial distance, r, the ray strikes the detector. By observing several diffracting angles from the calibration standard, an accurate measure of $\Delta$ is obtained. The program Fit2D is performing this procedure in an automated fashion where more instrument parameters, such as detector tilting angles and center coordinates, are determined. The reader is referred a paper by A. Hammersley which gives a comprehensive account of how calibration and integration of 2D powder x-ray diffraction data is performed using Fit2D.[51]

Once the diffractometer is calibrated, the sample within the DAC must be positioned precisely where the calibration standard was previously. This is accomplished having first located the calibration standard at the center of the sample stage's circle of rotation and then empirically one can determine how far and in what direction the stage must move in order that the sample in the DAC, once placed on the stage, need move to be in the center of rotation. A sample centering method was derived to determine the magnitude and direction a DAC must move to be located in the center of a stage's circle of rotation. This centering method uses the sample chamber in the gasket as an aperture for the collimated x-ray beam in combination with a photo diode to measure three positions along a given linear translation axis on the stage. Figure 2.11 shows how this would look if observed from above the experiment looking down. The sample chamber is represented by a circular aperture and the three positions to be measured are labeled r, $r_1$, and $r_2$. Given the geometry of the experiment we can only determine values of

rotation angle $\omega$ and positions along the y axis. At first we are at $\omega_o$ and are off the center of rotation by some arbitrary translation $r_x$ and $r_y$. By rotating the sample stage to two known angles, $\omega^+$ and $\omega^-$, two new y values, $y_1$ and $y_2$, can be measured by scanning the stage in the y direction. These two y values and rotation angle are used to solve for the translations rx and ry that bring the DAC to the center of the rotation circle.

Rotation by +/-$\omega$ transforms r into $r_2$ and $r_1$ respectively as indicated by equation 2.9.

$$\vec{r_1} = \begin{pmatrix} \cos\omega & -\sin\omega \\ \sin\omega & \cos\omega \end{pmatrix} \begin{pmatrix} r_x \\ r_y \end{pmatrix}$$

$$\vec{r_2} = \begin{pmatrix} \cos\omega & \sin\omega \\ -\sin\omega & \cos\omega \end{pmatrix} \begin{pmatrix} r_x \\ r_y \end{pmatrix}$$

(2.9)

$$r_{1y} = r_y - y_1$$
$$r_{2y} = r_y + y_2$$

(2.10)

By adding and subtracting the y components of $r_1$ and $r_2$, solving for $r_y$ and $r_x$ respectively, and substitution of equation 2.10 one obtains equation 2.11. Equation 2.11 is then used to determine where the center of rotation is relative to the current sample position.

$$r_y = \frac{y_2 - y_1}{2(\cos\omega - 1)}$$

$$r_x = \frac{-(y_1 + y_2)}{2\sin\omega}$$

(2.11)

Because the DAC must be removed from the diffractometer each time pressure is increased and/or measured, this centering method is routinely performed before each diffraction pattern is acquired. This ensures that the sample is replaced to this position as accurately as possible because any deviation will show up as changes in Bragg angles and
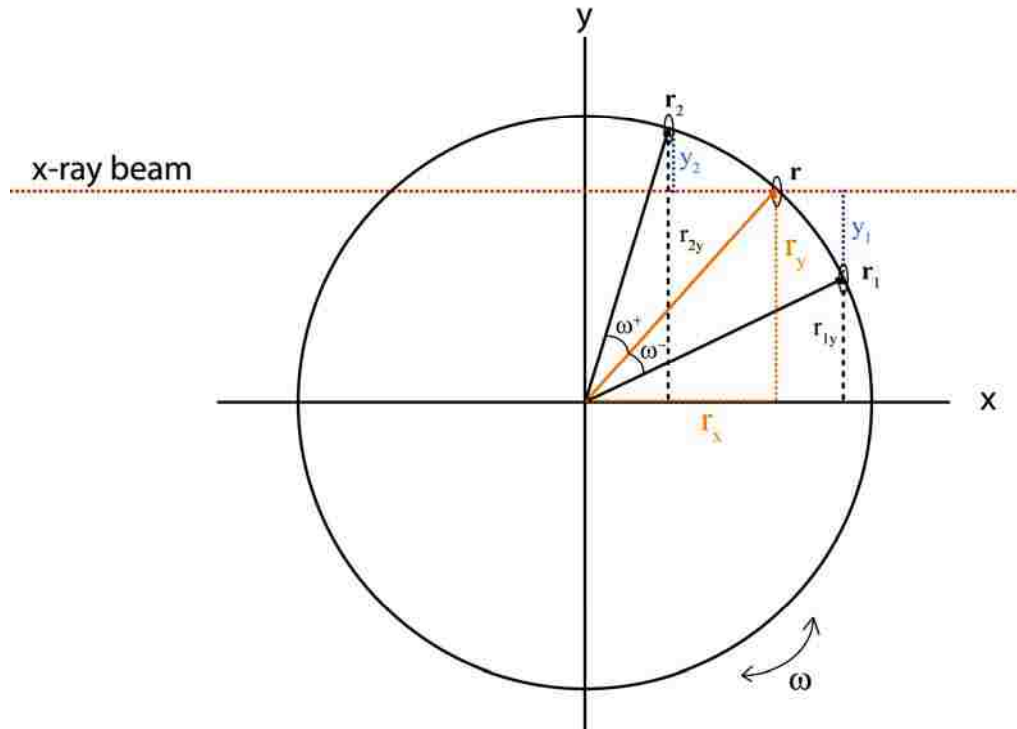
Figure 2.11 Sample centering diagram.
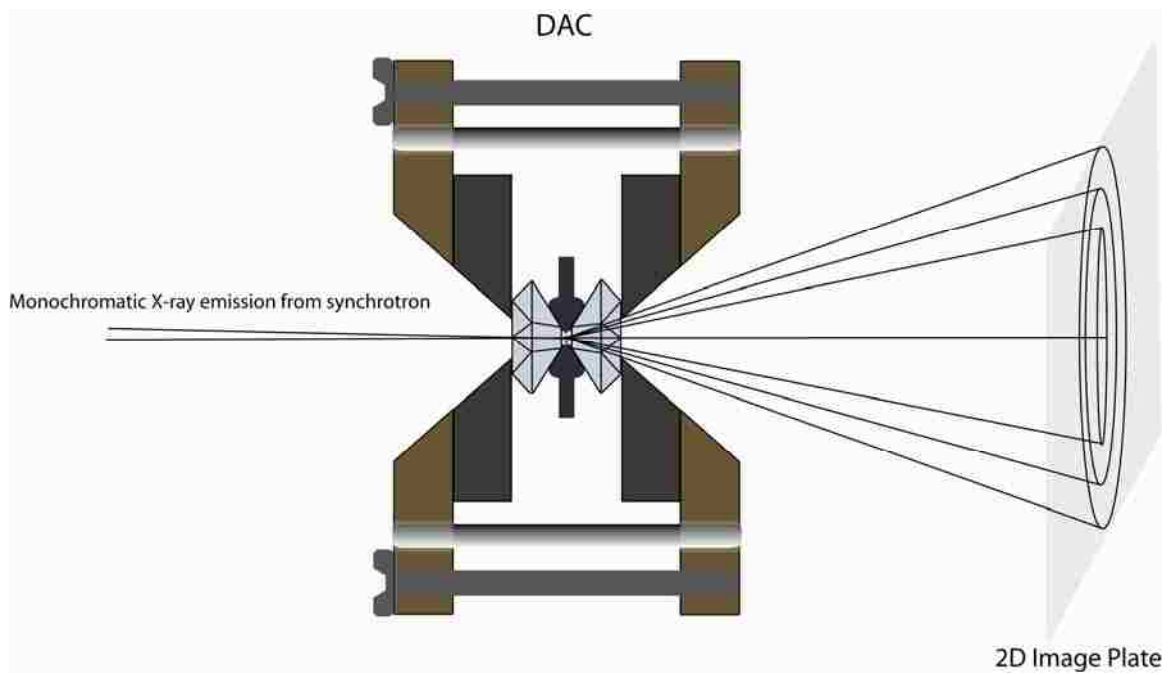


Figure 2.12 Schematic of a DAC as it is seen during a typical X-ray diffraction experiment.

compromise the accuracy of measured lattice constants.  Figure 2.12 gives a schematic of

the DAC as it would appear during a typical diffraction experiment.

In the current experiments, monochromatic X-rays from a synchrotron source are

brought to a focus at the sample position using a pair of KB-mirrors.  Debye-Scherre

cones of diffracted light impinge on an image plate as seen to the right in Figure 2.12.

The image plate detector used in all experiments is the MAR345 detector.  The MAR345

detector bins the incident image into a 3450 by 3450 pixel array.  Each 100 μM square

pixel is read out by a scanning diode laser and intensity information obtained.  Images of

the diffraction patterns produced by the sample are then converted into histograms using

the Fit2D software package.

The Rietveld method is the primary technique used for modeling observed powder

diffraction data.[53,54]  Calculated diffraction patterns are produced using an approximate

model for the crystal structure.  Calculated Bragg diffracted intensities are proportional to

the square of the structure factor, $F_{hkl}$, as defined in equation 2.12.  The structure factor is

a Fourier series in which each term describes the scattering contribution from one atom in

the crystal into a particular (hkl) reflection.  The sum is carried out over all atoms, j, in

the primitive cell and scaled to a multiplicative factor $f_j$, called the atomic scattering

factor.   The contributions for each atom j to reflection (hkl) are dependant on two

parameters (1) the type of atom $f_j$, which scales with atomic number Z and (2) its position

in the unit cell $(x_j, y_j, z_j)$.

$$F_{hkl} = \sum_j f_j e^{-2\pi i \left( hx_j + ky_j + lz_j \right)}$$ (2.12)

A structure model is first proposed based on approximate initial values for the atomic

positions $(x_j, y_j, z_j)$ and the unit cell constants $(a, b, c, \alpha, \beta, \gamma)$ for an assumed

crystallographic space group. The structure factors are then calculated for all (hkl)

reflections present. Calculated intensities $I_{hkl}$, represented by equation 2.13, are refined

against the observed diffraction pattern in a least squares manner where $H_{hkl}$ and $K_{hkl}$

represent peak profile functions and intensity correction parameters respectively. The

atomic positions, lattice constants, profile function, intensity correction parameters,

background functions...etc are adjusted until the square of the difference in observed and

calculated patterns is minimized.

$$I_{hkl} = |F_{hkl}|^2 H_{hkl} K_{hkl} \qquad (2.13)$$

The minimization parameter statistically weighted by the profile function, $M_p$, is

defined in equation 2.14 where $I_o$, $I_c$ and w are the observed, calculated intensities, and

statistical weights respectively. The residual of the fit is defined by equation 2.15 and is

of the most meaningful statistical parameters extracted from the refinement because it

contains the minimization parameter and is a measure of how well the observed and

calculated

$$M_p = \sum w(I_o - I_c)^2 \qquad (2.14)$$

patterns agree. Typically, $R_{wp}$ should be on the order of a few percent, however, it is not

uncommon that values upwards of 0.1 are obtained for powder diffraction data at high

pressure. This is especially true when the data are complicated by an irregular

background as is most often the case. A second parameter $R_F$, defined in equation 2.16,

is a measure of the agreement between the calculated and observed structure factors and

is biased towards the structure model. $R_F$ during a refinement should decrease along with

$R_{wp}$ and gives a measure of the reliability of the proposed structure.

$$R_{wp} = \sqrt{M_p \Big/ \sum w I_o^2} \qquad (2.15)$$

$$R_F = \frac{\sum_{hkl} |F_{hkl}(obs) - F_{hkl}(calc)|}{\sum_{hkl} |F_{hkl}(obs)|} \qquad (2.16)$$

A major benefit of the Rietveld method is in its use of the entire power diffraction pattern in the refinement procedure. Use of the full diffraction pattern dramatically increases the number of observables to the number of $2\theta$ steps in the data helping to overcome the problem of having an exceedingly large number of unknowns in the calculated intensity function resulting, in part, from peak overlap.

The General Structure Analysis System or GSAS[52] is the program used to carry out all Rietveld refinements. Initial structure models are taken as the ambient pressure structure and refined until $R_{wp}$ is minimized. Structure models for the high pressure phases observed are introduced and refined simultaneously with the low pressure phase once new features in the diffraction patters are found and identified. Refinements are progressed until the best fit to the overall diffraction pattern is achieved.

CHAPTER 3

THEORERTICAL METHODS

This chapter discusses the theoretical methods used in the simulation and analysis of data collected in this thesis. In separate sections, I will cover the use of; least squares refinement theory to model P-V equation of state data and normal coordinate analysis to model Raman and IR spectra.

### 3.1 Modeling of Equation of State Data

As a result of studying the properties of materials at high pressure via x-ray diffraction, pressure-volume (P-V) equation of state information can be determined which is useful in many respects. Pressure induced phase transitions are often seen via investigating the P-V isotherms where discontinuities may indicate first order structural phase transitions. In some cases, the misfit of P-V data to an otherwise correct theoretical equation of state that may indicate a weak first order phase transition has escaped ones observation. Material properties, such as the isothermal bulk modulus $K_o$ and its pressure derivative $K'_o$ can be determined which allow for the characterization of materials and analysis of trends across families of materials.

All P-V equation of state data generated in this thesis were modeled using the 3'rd order Birch-Murnaghan (BM3) (equation 3.1) and the Vinet (equation 3.2) equation of state (EOS). In these representations, x is defined as the ratio of measured volume at pressure P to a reference volume measured at $P_o$; $x=V/V_o$. The isothermal bulk modulus $K_o$ (evaluated at $P=P_o$), it's pressure derivative $K'_o$, and the reference volume $V_o$ are

varied in a least squares fashion until the best fit to the observed P-V data is obtained.  In

the case that $P_o$ is 1 bar, $V_o$ is not refined and the 1 bar value is used.

$$\text{(BM3)} \qquad P(x) = \frac{3}{2} K_o \left( x^{-\frac{7}{3}} - x^{-\frac{5}{3}} \right) \left[ 1 + \frac{3}{4} \left( K'_o - 4 \right) \left( x^{-\frac{2}{3}} - 1 \right) \right] \qquad\qquad (3.1)$$

$$\text{(Vinet)} \qquad P(x) = 3 K_o x^{-\frac{2}{3}} \left( 1 - x^{\frac{1}{3}} \right) e^{\left[ \frac{3}{2} \left( K'_o - 1 \right) \left( 1 - x^{\frac{1}{3}} \right) \right]} \qquad\qquad (3.2)$$

The 3'rd order Birch-Murnaghan equation of state, as will be shown first, is derived

from a power series expansion of the free energy, F, up to third order in Eulerian finite

strain, ε.  To fully appreciate the limitations of the BM3 EOS, we first begin with how the

ε used in the power series expansion is derived.  The Eulerian strain tensor $\varepsilon_{ij}$, equation

3.3, represents the deformation and displacement of a continuous body with respect to the

coordinates of the deformed state, $X_i$.  The components of the displacement vector are

given by $u_i$ and the indices i,j,k run over the all coordinates in the strained coordinate

frame.

$$\varepsilon_{ij} = \frac{1}{2} \left( \frac{\partial u_i}{\partial X_j} + \frac{\partial u_j}{\partial X_i} \right) - \frac{1}{2} \left( \sum_k \frac{\partial u_k}{\partial X_i} \frac{\partial u_k}{\partial X_j} \right) \qquad\qquad (3.3)$$

Going forward, the strict assumption of isotropic compressional strain caused by the

application of hydrostatic stress is made and this is mathematically written as $\varepsilon_{ij}=\varepsilon\delta_{ij}$ and

$\sigma_{ij}=-P_o\delta_{ij}$ respectively.  Assuming a hydrostatic stress state limits the pressure range the

BM3 EOS is valid over for a given pressure medium.  Table 2.1 lists the upper limit of

hydrostatic and quasi-hydrostatic behavior of every pressure medium used the present

series of experiments.  Assuming isotropic compressional strain further limits one to

materials that deform equally along each crystallographic axis.  This is the case for the C-

type but not A-type rare-Earth sesquioxides (RES).

The assumption that $\varepsilon_{ij}=\varepsilon\delta_{ij}$ and $\sigma_{ij}=-P_0\delta_{ij}$ implies equation 3.4 where $\theta = \sum_i \dfrac{\partial u_i}{\partial X_i}$.

$$\frac{\partial u_1}{\partial X_1} = \frac{\partial u_2}{\partial X_2} = \frac{\partial u_3}{\partial X_3} = \frac{\theta}{3} \tag{3.4}$$

One can view $\theta$ in 3.4 as a measure of cubical dilation in the strained state. By

substituting 3.4 into our definition of Eulerian finite strain, 3.3, we arrive at a very simple

expression for $\varepsilon$ as equation 3.5.

$$\varepsilon = \frac{\theta}{3} - \frac{1}{2}\frac{\theta^2}{9} \tag{3.5}$$

Using the deformation described by 3.4, we define the volume of a cube in the

strained and unstrained state as 3.6 where V and $V_0$ represent the strained and unstrained

volumes respectively. By dividing $V_0$ by V in 3.6 and substituting in for

$$V = (dX_1)^3$$
$$V_0 = \left[ (dX_1)\left(1 - \frac{\partial u_1}{\partial X_1}\right) \right]^3 \tag{3.6}$$

equation 3.4 we arrive at equation 3.7. In the right most expression in 3.7 we have

cleverly rearranged the exponents knowing, in advance, that we are after a form similar to

3.5.

$$\left(\frac{V_0}{V}\right) = \left(1 - \frac{\partial u_1}{\partial X_1}\right)^3 = \left(1 - \frac{\theta}{3}\right)^3 = \left[\left(1 - \frac{\theta}{3}\right)^2\right]^{3/2} \tag{3.7}$$

Expanding the squared term in 3.7 allows direct substitution of equation 3.5 and we

arrive at the familiar form of Eulerian finite strain listed as equation 3.8.

$$\left[\left(1 - \frac{\theta}{3}\right)^2\right]^{3/2} = \left[\left(1 - 2\frac{\theta}{3} + \frac{\theta^2}{9}\right)\right]^{3/2} = \left[1 - 2\left(\frac{\theta}{3} - \frac{\theta^2}{18}\right)\right]^{3/2} = \left[1 - 2\varepsilon\right]^{3/2} \tag{3.8}$$

Solving for ε in 3.8 in terms of $V_0/V$ gives equation 3.9 where we have used the previous definition of $x=V/V_0$ as in 3.1 and 3.2.

$$\varepsilon = \frac{1}{2}\left(1 - x^{-\frac{2}{3}}\right)$$ (3.9)

Armed now with a manageable description of Eulerian finite strain, equation 3.9, we proceed with the derivation of the BM3 EOS. The expansion of the free energy, F, is truncated at the 3'rd order in ε as equation 3.10. The coefficients, $a_i$, are determined by differentiation of F with respect to volume and evaluating at $V=V_0$. These are presented in table 3.1 for convenience.

$$F = a_0 + a_1\varepsilon + a_2\varepsilon^2 + a_3\varepsilon^3$$ (3.10)

Table 3.1 Free energy expansion terms for the BM3 EOS.

| $a_0$ | $F(V=V_0)$ | $a_0 = F_0$ |
|---|---|---|
| $a_1$ | $\left(\dfrac{\partial F}{\partial V}\right)_{V=V_0} = -P_0$ | $a_1 = -3P_0V_0$ |
| $a_2$ | $\left(\dfrac{\partial F^2}{\partial^2 V}\right)_{V=V_0} = \dfrac{K}{V_0}$ | $a_2 = \dfrac{3}{2}(3K - 5P_0)V_0$ |
| $a_3$ | $\left(\dfrac{\partial F^3}{\partial^3 V}\right)_{V=V_0} = \left(\dfrac{-K}{V_0^2}\right)\cdot(K'+1)$ | $a_3 = \dfrac{1}{2}(36K - 9KK' - 35P_0)V_0$ |

Substitution of the expansion coefficients in table 3.1 into equation 3.10 results in the BM3 EOS defined as equation 3.1. The limitations of the BM3 EOS are made obvious by this derivation. The definition of Eulerian finite strain makes the strict assumption of isotropic compression under hydrostatic stress. Moreover, the expansion of the free energy as a polynomial in ε does not have any clear physical justification. However, the BM3 EOS is widely used despite its limitations.

The Vinet EOS is derived by differentiation of an effective Rydberg potential,[58] equation 3.11, with respect to volume where $f = 3/2\left[K_0' - 1\right]$. In 3.11, L is a constant, r is the inter-atomic distance, and 'a' the equilibrium distance. The substitution $r/a = \left(V/V_0\right)^{1/3}$ is made in 3.11 and $P = -\left(\partial\phi/\partial V\right)_T$ evaluated. This results in equation 3.2 after some algebra. The Vinet EOS also suffers the limitation that isotropic compressional strain is again assumed.

$$\phi(r) = L\left[1 - f\left(1 - \frac{r}{a}\right)\right]e^{\left[f\left(1 - \frac{r}{a}\right)\right]} \tag{3.11}$$

Comparison of the two EOS forms, along with others, was considered by Singh[61] where he shows the two begin to deviate in agreement with one another below $(V/V_o)$=0.8. This is within the compression range for all RES studied and I see a good agreement in refined parameters for both forms. Many authors[58-61] point out that both the BM3, Vinet, and many other EOS forms break down at the infinite pressure limit where the behavior of a solid should approach that of a Thomas-Fermi gas with $K_\infty' = 5/3$. This is currently an active area of research where much of W. Holzapfel's efforts are in the determination of a physically sound equation of state that shows the correct pressure behavior up to the infinite pressure limit.

Fitting the P-V EOS data collected in this thesis to the BM3 and Vinet forms, derived above, was accomplished by use of non-linear least squares theory. A computer program, written in IDL, was used to automate the refinement process I derived. What follows is a complete derivation of the non-linear least square algorithm for the case of the Vinet EOS. It is a simple matter or repeating the steps with the substitution of the BM3 form to arrive at the refinement algorithm using the BM3 EOS.

In this derivation I make two substitution changes in equation 3.2 for the ease of the ensuing calculations. Letting $x = (V/V_0)^{1/3}$ and g=(1-x) we have the Vinet EOS as equation 3.12.

$$P(x) = 3K_0 x^{-2} g e^{(1.5K_0' - 1.5)g} \qquad (3.12)$$

The first step in setting up the least squares problem is defining the residual which we will be minimizing, $R_w$. The subscript, w, lets us know that our residual function will be statistically weighted. In a weighted least squares refinement, data points that are not known to very high accuracy contribute less to the overall residual function. This improves convergence of the algorithm and provides more accurate results. Equation 3.13 gives the square of the residual because it is the least value in the square of the residual that we are after.

$$R^2_w = \sum_i w_i [P_i - P(x_i)]^2 = \sum_i w_i [P_i - 3K_0 x_i^{-2} g_i e^{(1.5K_0' - 1.5)g_i}]^2 \qquad (3.13)$$

The sum in 3.13 runs over all data points for measured pressure $P_i$ and compression $x_i$. The statistical weights are defined as $w_i = 1/\sigma_i^2$ where the $\sigma_i$ are the quadratic sum of estimated uncertainties in pressure and the pressure equivalent uncertainties in volume. This is expressed more concisely in a mathematical sense as $\sigma_{P_{Eqv}} = \sqrt{\sigma_P^2 + \sigma_{V_{Eqv}}^2}$. The first term under the radical corresponds simply to the uncertainties in measured pressure. The second term under the radical is not so concisely written as equation 3.14.

$$\sigma_{V_{Eqv}} = \left( \frac{\partial P(x_i)}{\partial x_i} \right) \sigma_{V_i} = 3K_0 x_i^{-2} g(x_i) [f(x_i)(1.5 - 1.5K_0' - 2x_i^{-1}) - 1] \sigma_{V_i} \qquad (3.14)$$

The uncertainties in measured unit cell volume, $\sigma_{V_i}$, in 3.14, are defined for hexagonal A-type RES as $\sigma_V = V \sqrt{\frac{3}{4} \left[ 2\left( \frac{\Delta a}{a} \right)^2 + \left( \frac{\Delta c}{c} \right)^2 \right]}$ and for the cubic C-type RES

58

$\sigma_v = \sqrt{3}\left(\dfrac{\Delta a}{a}\right)$ where $\Delta a/a$ and $\Delta c/c$ are the fractional uncertainties in the measured lattice constants.

Next we must evaluate the partial derivatives of the residual with respect to each variable parameter in 3.13, $K_o$ and $K_o'$, set the result to zero, and solve for the respective variable parameter. I set this up in 3.15 and 3.16 noting that for $K_o'$ I calculate the $\partial/\partial K_0' (\ln R^2)$ because $K_o'$ appears in the exponent of 3.16 and simplifies the ensuing algebra.

$$\frac{\partial}{\partial K_0}\left(R^2\right) = \frac{\partial}{\partial K_0}\left(\sum_i w_i[P_i - 3K_0 x_i^{-2} g_i e^{(1.5K_0'-1.5)g_i}]^2\right) = 0 \qquad (3.15)$$

$$\frac{\partial}{\partial K_0'}\left(\ln R^2\right) = \frac{\partial}{\partial K_0'}\left(\ln \sum_i w_i[P_i - 3K_0 x_i^{-2} g_i e^{(1.5K_0'-1.5)g_i}]^2\right) = 0 \qquad (3.16)$$

Solving 3.15 and 3.16 for $K_o$ and $K_o'$ we get 3.17 and 3.18 which represent the best fit values per refinement iteration.

$$K_0 = \left(\frac{1}{3}\right)\left\{\frac{\sum_i w_i P_i x_i^{-2} g_i e^{(1.5K_0'-1.5)g_i}}{\sum_i w_i[x_i^{-2} g_i e^{(1.5K_0'-1.5)g_i}]^2}\right\} \qquad (3.17)$$

$$K_0' = 1 + \left(\frac{2}{3}\right)\left\{\frac{\sum_i w_i g_i \ln(P_i) - \sum_i w_i g_i \ln(3K_0 x_i^{-2} g_i)}{\sum_i w_i g_i^2}\right\} \qquad (3.18)$$

Errors in the refined values for $K_o$ and $K_o'$ are determined by evaluating 3.19 where the sum runs over all data points j and $\sigma_j$ are calculated from the statistical weights given above.

$$\sigma_{k_0}^2 = \sum_j \left( \frac{\partial K_0}{\partial P_j} \sigma_j \right)^2 = \left( \frac{\left(1/9\right)}{\sum_i w_i [x_i^{-2} g_i e^{(1.5K_0'-1.5)g_i}]^2} \right)^2$$

$$\sigma_{k_0'}^2 = \sum_j \left( \frac{\partial K_0'}{\partial \ln(P_j)} \sigma_j \right)^2 = \left( \frac{\left(4/9\right)}{\sum_i w_i [g_i]^2} \right)^2$$

(3.19)

The algorithm that I coded in IDL to carry out the least squares refinement is outlined in table 3.2. The process begins by reading in a 4 column, space delimited ASCII data file, as Step 1. Each column contains $P_i$, $\sigma P_i$, $V_i$, and, $\sigma V_i$ respectively where $\sigma$ represents the uncertainty in the respective data point. Starting values for $V_o$, $K_o$, and $K_o$' and entered manually. Typical starting values for $K_o$, and $K_o$' are 140 GPa and 4 respectively. Values for $V_o$ are obtained from diffraction data at 1 bar or for high pressure phases, the value is manually adjusted until a satisfactory reduced $\chi^2$ results. $\chi^2$ and the reduced $\chi^2$ values are defined as $R^2_w$ and $R^2_w/(N_o-N_p)$, where $N_o$ and $N_p$ are the number of observables and number of variable parameters respectively. At step 2, the initial fit to the data is plotted using equation 3.12 and the input P-V ASCII data are plotted over the fitted curve. At step 3, the best fit values for $K_o$ and $K_o$' are determined by evaluating 3.17 and 3.18. Step 4 updates these values in 3.13 and a new residual calculated. Next, step 5 evaluates $\chi^2$ and the reduced $\chi^2$ using the results of step 3. Additionally in this step, the uncertainties in the refined values for $K_o$ and $K_o$' are evaluated using 3.19. Step 6 is the deciding point where we compare the current value of the reduced $\chi^2$ with a predetermined threshold value and if we are within this value the refinement terminates. If $\chi^2$ is not less than the threshold value we return to step 2 and repeat.

Table 3.2 Equation of State refinement algorithm

| Step | Process |
|------|---------|
| 1 | Load ASCII Data - Set initial values for $V_o$, $K_o$, and $K_o'$ |
| 2 | Plot 3.12 and ASCII data |
| 3 | Evaluate 3.17 and 3.18 |
| 4 | update $K_o$ and $K_o'$ in 3.12 with refined values |
| 5 | Compute and display $\chi^2$, Reduced $\chi^2$, 3.19 |
| 6 | IF Reduced $\chi^2$ < threshold value GOTO 7 ELSE GOTO 2 |
| 7 | Plot 3.12 and output refinement data to ASCII file |
| 8 | END |

This refinement program was tested for accuracy using data from a recent publication by Agnes Dewale[45] in 2004 where P-V equation of state data were generated for Au, Pt, Ta, W, Cu, and Al.  In Dewaele 2004, the Vinet EOS is used to model all P-V compression data and fit parameters for $K_o$ and $K_o$' are determined.  I show in table 3.3 the results of my refinement algorithm as applied to the data in Dewale 2004 where estimated uncertainties in the refined parameters, as calculated by equation 3.19, are indicated numerically by the bold face digits.  My estimated uncertainties are within those reported in Dewaele 2004.

All P-V EOS data generated in the present experiments are fit to both the Vinet and BM3 EOS using the algorithm I derived.  There was not a statistically significant difference between the refined parameters in both cases, however, I report all refined EOS parameters using the Vinet EOS form.

Table 3.3 Comparative data used in testing the EOS refinement algorithm.

|                  | Au     | Pt     | Ta     | W      | Cu     | Al     |
|------------------|--------|--------|--------|--------|--------|--------|
| $V_o$            | 16.966 | 15.105 | 18.034 | 15.852 | 11.808 | 16.561 |
| $K_o$            | 166    | 265    | 190    | 296    | 132    | 75     |
| $K_o{}'$         | 6.09   | 5.63   | 3.78   | 4.36   | 5.34   | 4.45   |

## 3.2  The Raman Effect and Normal Coordinate Analysis

The origin of the Raman effect can be explained classically by considering the simple

example of light illuminating a diatomic molecule.  Assuming that the illuminating

monochromatic light has a field strength E and frequency $\nu$, we may write equation 3.20.

$$E(t) = E_0 \cos(2\pi\nu t) \tag{3.20}$$

A diatomic molecule perturbed by the field expressed by 3.20 is assumed to have a

dipole moment P induced by said field as described by equation 3.21.

$$P(t) = \alpha E(t) = \alpha E_0 \cos(2\pi\nu t) \tag{3.21}$$

If the molecule is vibrating with frequency $\nu_j$ we may write the atomic displacement,

q, as equation 3.22 where $q_0$ is the amplitude of oscillation.

$$q = q_0 \cos(2\pi\nu_j t) \tag{3.22}$$

For small amplitudes of oscillation, we may expand $\alpha$ as a Taylor series in q.  This is

shown up to first order in equation 3.23 where $\alpha_0$ represents the polarizability at

equilibrium position $q_0$.

$$\alpha = \alpha_0 + \left(\frac{\partial\alpha}{\partial q}\right)_{q=0} q + ...O^n \tag{3.23}$$

Substituting for q in 3.22 into 3.23 and the resulting expression for the polarizability into 3.21 we arrive at 3.24.

$$P = \alpha_0 E_0 \cos(2\pi \nu t) + \left(\frac{\partial \alpha}{\partial q}\right)_{q=0} q_0 E_0 \cos(2\pi \nu_j t)\cos(2\pi \nu t) \qquad (3.24)$$

Applying the double angle formula to the second term in 3.24 gives equation 3.25 and the evidence of the Raman effect is now apparent.

$$P = \alpha_0 E_0 \cos(2\pi \nu t) + \frac{1}{2}\left(\frac{\partial \alpha}{\partial q}\right)_{q=0} q_0 E_0 [\cos(2\pi[\nu + \nu_j]) + \cos(2\pi[\nu - \nu_j])] \qquad (3.25)$$

The first term in 3.25 describes an oscillating dipole moment at the same frequency as the perturbing field. This is called Rayleigh scattering. The second term in 3.25 describes Raman scattering and has two frequencies components, $\nu + \nu_j$ (anti-Stokes) and $\nu - \nu_j$ (Stokes), and is directly proportional to the change in polarizability. For a particular vibration to be "Raman active", the polarizability must be changing.

Our description of the Raman effect has so far been one dimensional. The polarizability may be written more generally as a second rank Cartesian tensor shown as equation 3.26.

$$\ddot{\alpha} = \begin{pmatrix} \alpha_{xx} & \alpha_{xy} & \alpha_{xz} \\ \alpha_{yx} & \alpha_{yy} & \alpha_{yz} \\ \alpha_{zx} & \alpha_{zy} & \alpha_{zz} \end{pmatrix} \qquad (3.26)$$

In this description, we see that if any one component of the polarizability tensor is changing during a vibration, it is Raman active. Now, for crystalline solid with N atoms in its Bravais cell, there are 3N normal modes of vibration. To determine which of these 3N modes of vibration should be Raman active, we look to quantum theory and group theory for answers.

Assuming a pure harmonic oscillator potential, the Schrödinger equation may be constructed as a function of the crystal's normal coordinates, $Q_k$, where the subscript k refers to a particular normal coordinate.

$$-\frac{\hbar^2}{2m}\nabla^2\psi(Q_k)+\frac{1}{2}Kq^2\psi(Q_k)=E\psi(Q_k) \qquad (3.27)$$

The solutions to equation 3.27 take the form of the Hermite polynomials and the first two are listed as equation 3.28.

$$\psi_0(Q_k)=(\eta/\pi)^{1/4}e^{-\eta Q_k^2/2} \quad E_0=\frac{1}{2}h\nu$$

$$\psi_1(Q_k)=2^{1/2}(\eta/\pi)^{1/4}Q_k e^{-\eta Q_k^2/2} \quad E_1=\frac{3}{2}h\nu \qquad (3.28)$$

$$\text{where } \eta=4\pi^2\mu\nu/h$$

By investigating the first two solutions in 3.28, we see that the ground state $\psi_0(Q_k)$ is invariant under any symmetry operation. However, the first excited state $\psi_1(Q_k)$ caries the same symmetry as $Q_k$. The probability of a transition from the ground to first excited state is determined by time dependent perturbation theory. Equation 3.29 generalizes this.

$$P\propto\left|\left\langle\psi_0\,|\,\hat{H}(t)\,|\,\psi_1\right\rangle\right|^2 \qquad (3.29)$$

$$\text{For the Raman effect } \hat{H}(t)\to\tilde{\alpha}_{ij}(t)$$

We see that for a vibrational mode to be Raman active, the integral in equation 3.29 must not vanish. Therefore, a normal vibrational mode associated with $Q_k$ becomes Raman active when at least one component of $\alpha_{ij}$ belongs to the same symmetry species as $Q_k$. A similar argument is made for a normal mode to be Infrared (IR) active. In this case the polarizability tensor is replaced with the dipole moment, $p_j$. To generalize; a particular normal mode of vibration is Raman and/or IR active if any component of the

polarizability tensor, or dipole moment vector belongs to the same symmetry species as the normal coordinate describing the vibration in question. This powerful statement allows one to determine the number and type vibrations that are optically active through the use of group theory.

In the present case, Raman and IR spectra for hexagonal A-type $La_2O_3$ are analyzed and results interpreted using group theoretical considerations largely developed by E.B. Wilson.[62] Normal coordinate analysis is performed using the GF-matrix method to calculate vibrational frequencies following the application of Wilson's theory of molecular vibrations to crystalline lattices as described by Shimanouchi.[63] The correlation method, described by Nakamoto[64], is used to predict the number and type of vibrational species present in the ambient and high pressure phases discussed in the forgoing sections.

Next, I will discuss how the correlation technique is used to determine the number and type of optically active vibrational modes in a crystalline solid belonging to a particular point symmetry group. For any point group, there exist "subgroups" that contain a fraction of the symmetry elements inherent in the "parent" group. The relationship between the symmetry species found in the parent group and those of the subgroups are tabulated in group correlation tables.[64] Because the crystallographic point group adopted by a given Bravais cell contains atomic site groups that are subgroups of the parent point group, the correlation tables may be used to determine how the symmetry species adopted by the atomic sites factor in the parent point group.

The normal vibrations for a given Bravais cell can be described in terms of translational motions of its individual atoms along the x, y, and z Cartesian axes. The

normal modes in an N-atom Bravais cell can therefore be expressed by using 3N translational motions. Because the symmetry species of the normal modes must correlate with those of the translational motions for the atomic sites within the Bravais cell, the correlation tables may be used to give this relationship. This is referred to as the Correlation Method and is discussed, at length, by Ferraro[65] and Nakamoto.[64]

For the hexagonal A-Type sesquioxide structure, there are 2 $C_{3v}$ sites whose translational species are represented by $A(T_z)$ and $E_u(T_x,T_y)$ which factor into the $A_{1g}$, $A_{2u}$ and $E_g$, $E_u$ species respectively in the $D_{3d}$ point group. The single $D_{3d}$ site has its translational species mapped one to one onto the parent point group. Arrows in figure 3.1 connect the translational species of the atomic site groups to the parent group as given by the correlation table for the $D_{3d}$ factor group. The total vibrational representation is given by the sum of the arrows terminating on a species in the factor group. For the $C_{3v}$ site, each arrow is counted twice because there are two such sites in the Bravais cell. There must also be a total of three degrees of freedom that account for the translation of the entire Bravais cell. Theses are the acoustic modes and are subtracted from the total representation giving only the optically active modes. For optically active vibrations in the A-Type structure, the correlation method gives $\Gamma_{vib} = 2A_{1g}(R) + 2A_{2u}(IR) + 2E_g(R) + 2E_u(IR)$ where R and IR indicate Raman and Infrared activity respectively.

|  | **Site Group** | **Factor Group** | **Site Group** |
|--|----------------|------------------|----------------|
|  | $2*C_{3v}$ | $D_{3d}$ | $D_{3d}$ |

$A\ (T_z)$ → $A_{1g}$                 $A_{2u}(T_z)$

$A_{2u}$

$E_u\ (T_x, T_y)$ → $E_g$                 $E_u(T_x,\ T_y)$

$E_u$

| Site | $A_{1g}$ | $A_{2u}(T_z)$ | $E_g\ (R_x, R_y)$ | $E_u\ (T_z, T_y)$ |
|------|----------|---------------|-------------------|-------------------|
| $2*\ C_{3v}$ | 1 | 1 | 1 | 1 |
| $1*\ D_{3d}$ | 0 | 1 | 0 | 1 |
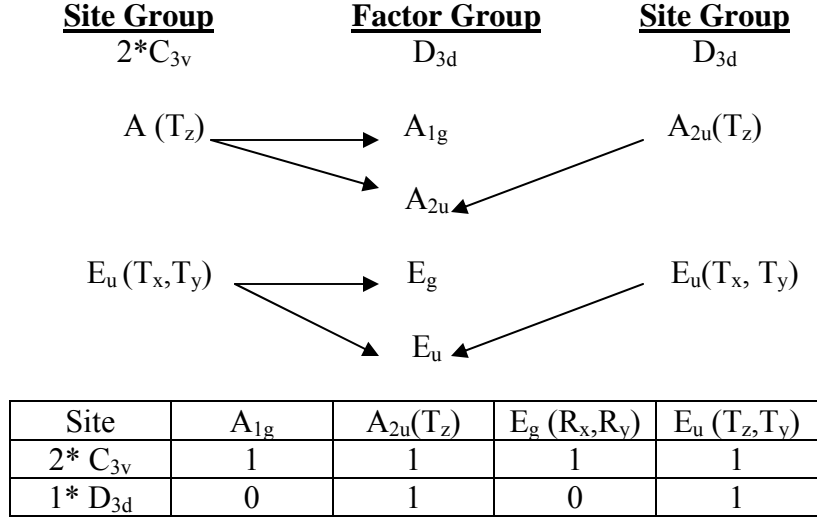
$$\Gamma_{total} = 2A_{1g} + 3A_{2u} + 2E_g + 3E_u$$
$$\Gamma_{Acoustic} = A_{2u} + E_u$$
$$\Gamma_{vib} = 2A_{1g} + 2A_{2u} + 2E_g + 2E_u$$

Figure 3.1. Correlation method applied to the A-Type sesquioxide structure. Arrows indicate the correlation between the translational species for the atomic sites and the parent point group in which they exist. The numbers of vibrational modes and atomic site involved are tabulated in the accompanied table. The vibrational representations are also listed.

Moving forward with the knowledge of the total vibrational representation, we know what to expect from our normal coordinate calculations except the vibrational frequencies associated with each normal mode. In my normal coordinate calculations, I use the GF matrix method[62-64] and solve the secular equation $|GF-E\lambda|=0$ for the eigenvalues, $\lambda$, representing the frequencies of the normal modes of vibration. In the usage of Cartesian coordinates, the G matrix listed as equation 3.30, is defined as a diagonal matrix comprised of the reciprocal masses of atoms in the Bravais cell. Super scripts *c, i,* or *sym* indicate the coordinate space, Cartesian, internal, or symmetry, a particular G or F matrix belongs.

$$G^c = \begin{pmatrix} \mu_{O1} & & & & 0 \\ & \mu_{O2} & & \bullet & \\ & & \mu_{O3} & & \\ & \bullet & & \mu_{Ln1} & \\ 0 & & & & \mu_{Ln2} \end{pmatrix} \tag{3.30}$$

The F matrix, also diagonal, is comprised of the force constants related to each internal coordinate defined. Because it is chosen here to describe the force constants ($f_i$) in terms of the internal coordinates ($r_i$), a transformation matrix B, defined as equation 3.31, must be derived to relate the internal coordinates to the Cartesian coordinates. It is determined that 23 internal coordinates are needed to fully describe the interactions within the Bravais cell of the A-type RES structure and with its first nearest neighbor cells. These internal coordinates are listed as $r_i$ where i=1..23 in figure 3.2. Atoms belonging to nearest neighbor cells are listed by indices ijk where the appropriate subscript is indexed by one unit. The $\vec{B}$ matrix is thereby a 23x5 element matrix (this accounts for the 23 internal coordinates and the 5 atoms in the Bravais cell) and may be represented by its component matrices $B^x$, $B^y$, $B^z$. The $F^i$ matrix is represented by a 23x23 element diagonal matrix.

$$\vec{R} = \vec{B} \cdot \vec{X} \tag{3.31}$$

The $F$ matrix, transformed to Cartesian space, for the z coordinates is given by equation 3.32. Because x,y transform as a degenerate pair in the $D_{3d}$ point group, it is necessary only to derive $B^x$ or $B^y$ and therefore only $F$ matrices relating to x or y and z coordinates.

$$F_z^c = \tilde{B}^z F^i B^z \tag{3.32}$$

68

The $B^z$ and $B^y$ matrices are defined in table 3.4 where rows and columns headed by $r_i$ and $Ln_i$ ($O_i$): $z_i$ ($y_i$) refer to the 23 internal coordinates and the 5 atoms in the Bravais cell respectively.
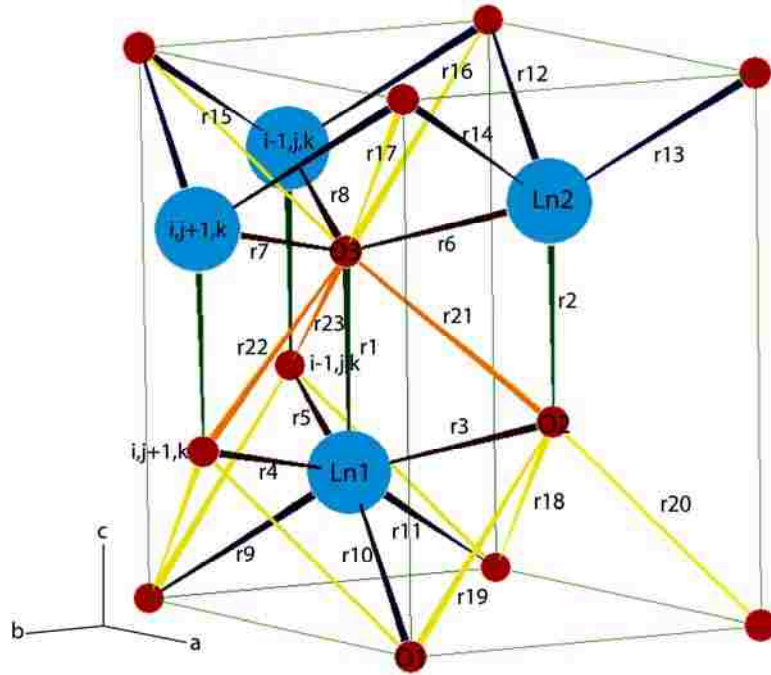


Figure 3.2 Internal coordinates ($r_i$) for the A-Type RES structure. Atoms belonging to adjacent cells are listed with ijk indices.

Because there are N=5 atoms in the A-Type RES Bravais cell, five sets of Cartesian coordinates are needed to fully describe the 3N normal modes. These coordinates, corresponding to atoms O1, O2, O3, La1, and La2, are numbered 1 through 5 in this respective order.

To facilitate the solution to the secular equation, a transformation from Cartesian to symmetry coordinates, $S_i$, is applied. Transforming to symmetry coordinates reduces the order of the secular equation needed to be solved by block diagonalizing the G and F matrices. In the present case, a reduction from a single 5$^{th}$ order matrix to a 2$^{nd}$ and 3$^{rd}$

69

order matter is produced. Additionally, symmetry transformation elucidates the correlation between a particular Eigen mode frequency and its vibrational species. The symmetry coordinate transformation matrix, $U_{jk}$, appearing in equation 3.33 is derived using the relationship by Nelison-Berryman[64,69], shown as equation 3.34, which relates the symmetry coordinates $S_j$ to the Cartesian coordinates $X_k$.

Table 3.4. Matrix elements for the $B_z$ and $B_y$ matrices. Internal coordinates ($r_i$) are graphically depicted in figure 3.2.

| $\Gamma_i, f_i$ | Bz | | | | | By | | | | |
|---|---|---|---|---|---|---|---|---|---|---|
| | O1 : z1 | O2 : z2 | O3 : z3 | Ln1 : z4 | Ln2 : z5 | O1 : y1 | O2 : y2 | O3 : y3 | Ln1 : y4 | Ln2 : y5 |
| r1, f1 | 0 | 0 | 1 | -1 | | 0 | 0 | 0 | 0 | 0 |
| r2, f1 | 0 | -1 | 0 | 0 | 1 | 0 | 0 | 0 | 0 | 0 |
| r3, f2 | 0 | COS(φ1) | 0 | -COS(φ1) | 0 | 0 | -SIN(φ1)SIN(θ1) | 0 | SIN(φ1)SIN(θ1) | 0 |
| r4, f2 | 0 | COS(φ1) | 0 | -COS(φ1) | 0 | 0 | -SIN(φ1)SIN(θ1) | 0 | SIN(φ1)SIN(θ1) | 0 |
| r5, f2 | 0 | COS(φ1) | 0 | -COS(φ1) | 0 | 0 | SIN(φ1)SIN(θ2) | 0 | -SIN(φ1)SIN(θ2) | 0 |
| r6, f2 | 0 | 0 | -COS(φ1) | 0 | COS(φ1) | 0 | 0 | SIN(φ1)SIN(θ1) | 0 | -SIN(φ1)SIN(θ1) |
| r7, f2 | 0 | 0 | -COS(φ1) | 0 | COS(φ1) | 0 | 0 | SIN(φ1)SIN(θ1) | 0 | -SIN(φ1)SIN(θ1) |
| r8, f2 | 0 | 0 | -COS(φ1) | 0 | COS(φ1) | 0 | 0 | -SIN(φ1)SIN(θ2) | 0 | SIN(φ1)SIN(θ2) |
| r9, f3 | -COS(φ2) | 0 | 0 | COS(φ2) | 0 | SIN(φ2)SIN(θ1) | 0 | 0 | -SIN(φ2)SIN(θ1) | 0 |
| r10, f3 | -COS(φ2) | 0 | 0 | COS(φ2) | 0 | -SIN(φ2)SIN(θ2) | 0 | 0 | SIN(φ2)SIN(θ2) | 0 |
| r11, f3 | -COS(φ2) | 0 | 0 | COS(φ2) | 0 | SIN(φ2)SIN(θ1) | 0 | 0 | -SIN(φ2)SIN(θ1) | 0 |
| r12, f3 | COS(φ2) | 0 | 0 | 0 | -COS(φ2) | SIN(φ2)SIN(θ2) | 0 | 0 | 0 | -SIN(φ2)SIN(θ2) |
| r13, f3 | COS(φ2) | 0 | 0 | 0 | -COS(φ2) | -SIN(φ2)SIN(θ1) | 0 | 0 | 0 | SIN(φ2)SIN(θ1) |
| r14, f3 | COS(φ2) | 0 | 0 | 0 | -COS(φ2) | -SIN(φ2)SIN(θ1) | 0 | 0 | 0 | SIN(φ2)SIN(θ1) |
| r15, f4 | COS(φ3) | 0 | -COS(φ3) | 0 | 0 | SIN(φ3)SIN(θ1) | 0 | -SIN(φ3)SIN(θ1) | 0 | 0 |
| r16, f4 | COS(φ3) | 0 | -COS(φ3) | 0 | 0 | SIN(φ3)SIN(θ1) | 0 | -SIN(φ3)SIN(θ1) | 0 | 0 |
| r17, f4 | COS(φ3) | 0 | -COS(φ3) | 0 | 0 | -SIN(φ3)SIN(θ2) | 0 | SIN(φ3)SIN(θ2) | 0 | 0 |
| r18, f4 | -COS(φ3) | COS(φ3) | 0 | 0 | 0 | SIN(φ3)SIN(θ2) | -SIN(φ3)SIN(θ2) | 0 | 0 | 0 |
| r19, f4 | -COS(φ3) | COS(φ3) | 0 | 0 | 0 | -SIN(φ3)SIN(θ1) | SIN(φ3)SIN(θ1) | 0 | 0 | 0 |
| r20, f4 | -COS(φ3) | COS(φ3) | 0 | 0 | 0 | -SIN(φ3)SIN(θ1) | SIN(φ3)SIN(θ1) | 0 | 0 | 0 |
| r21, f5 | 0 | -COS(φ4) | COS(φ4) | 0 | 0 | 0 | -SIN(φ4)SIN(θ1) | SIN(φ4)SIN(θ1) | 0 | 0 |
| r22, f5 | 0 | -COS(φ4) | COS(φ4) | 0 | 0 | 0 | -SIN(φ4)SIN(θ1) | SIN(φ4)SIN(θ1) | 0 | 0 |
| r23, f5 | 0 | -COS(φ4) | COS(φ4) | 0 | 0 | 0 | SIN(φ4)SIN(θ2) | -SIN(φ4)SIN(θ2) | 0 | 0 |

φ 1,2,3,4 = 73.7, 56.2, 46.1, 51.7 degress respectively
θ 1,2 = 30, 90 degrees respectively

$$S_j = U_{jk} X_k \tag{3.33}$$

$$S_{C_i}^{\Gamma_i} = N \sum_K \chi_i(K) K(C_i) \tag{3.34}$$

In equation 3.34, symmetry coordinates $S_{C_i}^{\Gamma_i}$ are derived for each irreducible representation $\Gamma_i$ using Cartesian generators $C_i$ for all 15 normal modes present. The sum in equation 3.34 is over all symmetry operations K in the $D_{3d}$ point group, N is a normalization constant, $\chi_i$ are the characters of the K symmetry operations, $K(C_i)$ is the

outcome of operating a particular K on one of the generators $C_i$. An example of how the symmetry coordinates are defined is shown in equations 3.35-3.37. This procedure is applied to all 15 Cartesian coordinates producing 15 symmetry coordinates. However, because the x and y coordinates transform as a degenerate pair in $D_{3d}$, only the x or y symmetry coordinates are needed.

$$S_{Z_1}^{A_{1g}} = N\left[1 \cdot I(z_1) + 1 \cdot 2 \cdot 3^+(z_1) + 1 \cdot 3 \cdot C_2(z_1) + 1 \cdot i(z_1) + 1 \cdot 2 \cdot S_6(z_1) + 1 \cdot 3 \cdot \sigma_d(z_1)\right] \quad (3.35)$$

$$S_{Z_1}^{A_{1g}} = 0$$

$$S_{Z_1}^{A_{2u}} = N\left[1 \cdot I(z_1) + 1 \cdot 2 \cdot 3^+(z_1) - 1 \cdot 3 \cdot C_2(z_1) - 1 \cdot i(z_1) - 1 \cdot 2 \cdot S_6(z_1) + 1 \cdot 3 \cdot \sigma_d(z_1)\right] \quad (3.36)$$

$$S_{Z_1}^{A_{2u}} = \frac{1}{\sqrt{2}}[z_1]$$

$$S_{Z2}^{A_{1g}} = N\left[1 \cdot I(z_2) + 1 \cdot 2 \cdot 3^+(z_2) + 1 \cdot 3 \cdot C_2(z_2) + 1 \cdot i(z_2) + 1 \cdot 2 \cdot S_6(z_2) + 1 \cdot 3 \cdot \sigma_d(z_2)\right] \quad (3.37)$$

$$S_{Z2}^{A_{1g}} = N\left[1 \cdot (z_2) + 2 \cdot (z_2) + 3 \cdot (-z_3) + 1 \cdot (-z_3) + 2 \cdot (-z_3) + 3 \cdot (z_2)\right] = N\left[6z_2 - 6z_3\right]$$

$$S_{Z2}^{A_{1g}} = \frac{1}{\sqrt{2}}[z_2 - z_3]$$

Several points may be made by immediate inspection of the symmetry coordinates when compared back to table 3.4. First, 3.35 indicates O1 atoms on $D_{3d}$ sites are not recruited by an $A_{1g}$ mode rather 3.36 shows an $A_{2u}$ mode is responsible. Furthermore, this $A_{2u}$ mode can be regarded as an acoustic mode because it describes the translation of the Bravais cell along the z direction. Equation 3.37 indicates oxygen atoms O2 and O3 on $C_{3v}$ sites are recruited in the $A_{1g}$ vibrational mode.

The U matrix is defined as equation 3.38 and is identical for the x, y, and z representations with the exception that $A_{1g}$ and $A_{2u}$ modes are described by generators over the z coordinates and $E_g$ and $E_u$ modes by generators over the x and y coordinates.

$$U_{jk} = \begin{pmatrix} 1 & 0 & 0 & 0 & 0 \\ 0 & \dfrac{1}{\sqrt{2}} & -\dfrac{1}{\sqrt{2}} & 0 & 0 \\ 0 & 0 & 0 & \dfrac{1}{\sqrt{2}} & -\dfrac{1}{\sqrt{2}} \\ 0 & \dfrac{1}{\sqrt{2}} & \dfrac{1}{\sqrt{2}} & 0 & 0 \\ 0 & 0 & 0 & \dfrac{1}{\sqrt{2}} & \dfrac{1}{\sqrt{2}} \end{pmatrix}$$ (3.38)

The F and G matrices, transformed to symmetry coordinates, are given by equations 3.39 and 3.40. The F matrix, in equation 3.39, pertains to vibrations that recruit motion along the z-axis ($A_{1g}$, $A_{2u}$) as indicated by the z subscript.

$$F_Z^{Sym} = U\tilde{B}^z F^i B^z \tilde{U} = U F_Z^C \tilde{U}$$ (3.39)

$$F_Z^{Sym} = \begin{pmatrix} A & B & C & 0 & 0 \\ B & D & E & 0 & 0 \\ C & E & F & 0 & 0 \\ \hline 0 & 0 & 0 & G & H \\ 0 & 0 & 0 & H & G \end{pmatrix} \qquad F_Z^{A2u} = \begin{pmatrix} A & B & C \\ B & D & E \\ C & E & F \end{pmatrix}$$

$$F_Z^{A1g} = \begin{pmatrix} G & H \\ H & G \end{pmatrix}$$

$$Where: \begin{bmatrix} A = 6\left(f_3 \cos^2 \phi_2 + f_4 \cos^2 \varphi_3\right) \\ B = -\dfrac{6}{\sqrt{2}}\left(f_4 \cos^2 \phi_3\right) \\ C = -\dfrac{6}{\sqrt{2}}\left(f_3 \cos^2 \phi_2\right) \\ D = f_1 + 3\left(f_2 \cos^2 \phi_1 + f_4 \cos^2 \varphi_3\right) \end{bmatrix} \cdots \begin{bmatrix} E = -f_1 - 3f_2 \cos^2 \phi_1 \\ F = f_1 + 3\left(f_2 \cos^2 \phi_1 + f_3 \cos^2 \varphi_2\right) \\ G = f_1 + 3\left(f_2 \cos^2 \phi_1 + f_4 \cos^2 \varphi_3\right) + 6f_5 \cos^2 \varphi_4 \\ H = -f_1 + 3f_2 \cos^2 \phi_1 \end{bmatrix}$$

$$G_Z^{Sym} = U G^c \tilde{U}$$ (3.40)

$$G_Z^{Sym} = \begin{pmatrix} \mu_{O1} & 0 & 0 & 0 & 0 \\ 0 & \dfrac{1}{2}\left(\mu_{O2} + \mu_{O3}\right) & 0 & 0 & 0 \\ 0 & 0 & \dfrac{1}{2}\left(\mu_{Ln1} + \mu_{Ln2}\right) & 0 & 0 \\ \hline 0 & 0 & 0 & \dfrac{1}{2}\left(\mu_{O2} + \mu_{O3}\right) & 0 \\ 0 & 0 & 0 & 0 & \dfrac{1}{2}\left(\mu_{Ln1} + \mu_{Ln2}\right) \end{pmatrix} \begin{matrix} \\ \\ G_Z^{A2u} \\ \\ \\ G_Z^{A1g} \end{matrix}$$

The block diagonalized representations of the F and G matrices may now be broken down to yield a second and third order matrix representing the $A_{1g}$ and $A_{2u}$ vibrations as shown by the shaded areas in equations 3.39 and 3.40. The same symmetry transformation is applied to the $F_Y^C$ matrix resulting in a second and third order matrix for the $E_g$ and $E_u$ vibrational modes.

The secular equations now to be solved take the form of equation 3.41 where the eigen frequencies are representative of the vibrational mode indicated by the superscripts. A secular equation is solved for each of the vibrational species present.

$$\left| G_z^{A1g} F_z^{A1g} - \lambda E \right| = 0 \qquad \left| G_{x,y}^{Eg} F_{x,y}^{Eg} - \lambda E \right| = 0 \qquad (3.41)$$
$$\left| G_z^{A2u} F_z^{A2u} - \lambda E \right| = 0 \qquad \left| G_{x,y}^{Eu} F_{x,y}^{Eu} - \lambda E \right| = 0$$

CHAPTER 4

SYSTEMATIC OBSERVATIONS

In this chapter, I present high pressure X-ray diffraction data collected in a systematic compression study which included most all the rare-Earth sesquioxide (RES) compounds. The results of this study suggest a more complex phase transition scheme must be present in the RES compounds than was originally thought, see Chapter 1.4 for details. This prompted the detailed investigation of one RES compound in particular, $La_2O_3$, as will be discussed in Chapter 5.

In chapter 4.1, all powder diffraction data are separated into subsections according to the particular RES studied. A brief description of the experimental conditions relative to each experiment is given along with comments pertaining to the data. I note that not all data are presented in the body of this thesis. Rather, where applicable, data sets are located in referenced sections in the Appendix to this thesis. In Chapter 4.2, a summary of the data is provided.


4.1 X-Ray Diffraction Data

The high pressure behavior of the RES $RE_2O_3$ (RE=La,Sm, Eu, Gd, Er, Yb, Lu, and Y) are studied using the methods of X-ray power diffraction as discussed in Chapter 2.4. Separate compression experiments are conducted for each of the RES studied. In each compression experiment, a series of diffraction patterns, refined lattice constants, and unit cell volumes are produced. Each data set is labeled by the name of the particular RES compound followed by an experimental run number. For example, $La_2O_3$ Experimental

Run #1 is the first set of compression data collected on $La_2O_3$ and subsequent information

on that experiment may be found in the appendix under that heading.

Table 4.1 outlines all x-ray diffraction experiments involved in this study. Reported

are the pressures at which each material is observed to transform from the cubic C-Type

to the hexagonal A-Type structure. $La_2O_3$ is the only material in Table 4.1 involved in

this study that adopts the A-Type structure at ambient pressure. Here, reporting a 0.0001

GPa transition pressure is simply a way of stating that this material starts of in the A-

Type phase at ambient pressure (~0.0001 GPa).

Table 4.1 Observed C to A-Type phase transitions in the lanthanide
sesquioxides. Pressures are reported in GPa on increasing pressure with an
estimated uncertainty of +-1.5 Gpa.

Lanthanide Sesquioxide $Ln_2O_3$ C to A-Type Observed Phase Transition Pressure

| $Ln_2O_3$ | Transition Pressure | Pressure Range | Pressure Medium |
|---|---|---|---|
| La | 0.0001 | 17.8 | Ar |
| Ce | x | x | x |
| Pr | x | x | x |
| Nd | x | x | x |
| Pm | x | x | x |
| Sm | 4 | 39.5 | $N_2$, Ar |
| Eu | 6 | 16.3 | $N_2$ |
| Gd | 7 | 76.9 | $N_2$, Ar, He |
| Tb | x | x | x |
| Dy | x | x | x |
| Ho | x | x | x |
| Y | 13 | 34.5 | $N_2$ |
| Er | 14 | 17.2 | $N_2$ |
| Tm | x | x | x |
| Yb | 17 | 32.5 | $N_2$ |
| Lu | 14 | 16.3 | $N_2$ |

### 4.1.1  La$_2$O$_3$

La$_2$O$_3$ Experimental Run #1 is performed at HPCAT's 16 ID-B diffraction beam line

using a focused X-ray beam of wavelength 0.41356 angstroms.  A rhenium sample

chamber, having dimensions of 100 μm in diameter by 50 μm in thickness, is loaded with

an amount of polycrystalline La$_2$O$_3$ filling approximately one third its volume.  A

pressure transmitting medium of cryogenically condensed argon gas is introduced into

the sample chamber along with several ruby spheres used as pressure markers.  The DAC

is closed under a bath of liquid argon, pressurized to 3 GPa, and then removed allowing

the cell to return to ambient temperature.

Figure 4.1 contains a plot showing all of the integrated diffraction patterns collected

for La$_2$O$_3$ Experimental Run #1.  For each observed diffraction pattern, a calculated

pattern is produced using structure models of the identified phases present in the

experiment.  In this case, there are detectable amounts of La(OH)$_3$ and Ar from the

pressure medium.  Diffraction peaks from La(OH)$_3$ and Ar are marked with x's and *'s

respectively for the lowest pressure recorded.

Because of the extreme hygroscopic nature of La$_2$O$_3$, it is nearly impossible to prevent

the formation of La(OH)$_3$ as a result of the sample's brief exposure to atmospheric

humidity during the loading process.  However, it is observed that the hydroxide phase

becomes less stable as pressure is increased and is thought not to be problematic for the

investigation of the A-Type sesquioxide phase.

Once all impurity phases are determined and their peak positions noted, they are

excluded from the ensuing Rietveld structure refinements.  Figure 4.2 shows the finial

refinement of the lowest pressure diffraction pattern using the A-Type structure model of
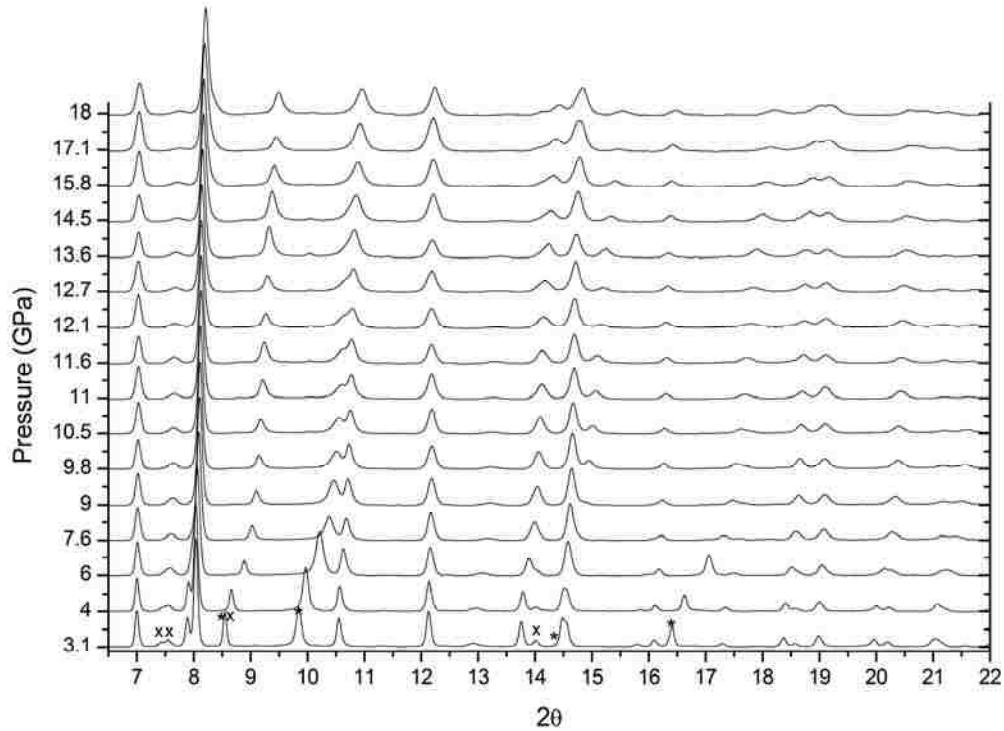
Figure 4.1 Angular dispersive X-ray diffraction of $La_2O_3$ compressed to 18 GPa in an argon pressure transmitting medium.

$La_2O_3$ compressed to 4.1 GPa. Tick marks below the diffraction pattern indicate the location of calculated diffraction peaks in the plot. From top to bottom they indicate the positions of diffraction peaks from A-type $La_2O_3$, $La(OH)_3$, and Ar respectively. The residual difference in the calculated and experimental patterns is shown below the diffraction pattern. Statistical results correlating the agreement between calculated and observed diffraction patterns are displayed in the upper right corner of figure 4.2. These parameters are defined in chapter 2.4. A profile weighted residual (wRp) value of 0.085 is typical for these experiments and indicates a reasonable fit to the calculated lattice plane d-spacings. However, a $RF^2$ value of 0.26 is not very good and indicates a misfit to the observed intensities.

Lattice parameters, obtained via the Rietveld refinement method, are subsequently

used to calculate unit cell volumes. Table 4.2 lists all refined lattice parameters and unit

cell volumes as a function of pressure for this experiment. Using the data from Table 4.2,

the isothermal bulk modulus, $K_0$, and the derivative of the bulk modulus, $K_0$', are obtained

by least squares refinement fit of the data to the Vinet equation of state (EOS). These

results are shown in figure 4.3 and the details of the fitting procedure and theory are

discussed in chapter 3.1.
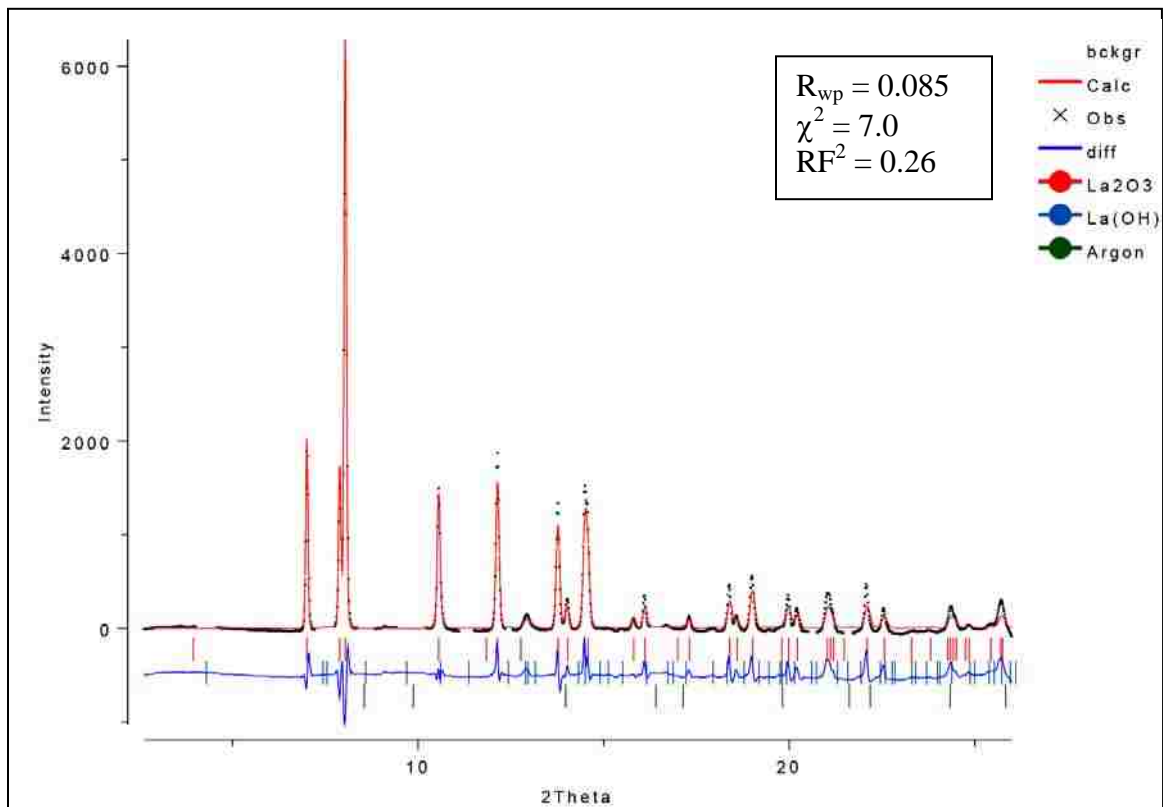


Figure 4.2 Rietveld refinement of $La_2O_3$ at 3.1 GPa loaded in an argon pressure
transmitting medium.

It is important to note that the fit of the Vinet EOS is not at all that good. In fact, the

fitted curve does not lay within the estimated error for the first four data points. There

are several reasons which may explain this.  First, the structure model used to generate

the unit cell volumes is based on the assumption that the A-Type sesquioxide crystal

structure is the stable phase for $La_2O_3$ at high pressure.  This may provide evidence that

the A-Type phase is, in fact, not stable for pressures above a 3 GPa.

Table 4.2 Compression Data on A-Type $La_2O_3$
Experimental Run: $La_2O_3$ #1
Source: HPCAT ID-B

| P (GPa) | a($A^3$) | c($A^3$) | Vol($A^3$)/Z |
|---------|----------|----------|--------------|
| 0.0001  | 3.9340   | 6.1360   | 16.4481      |
| 3.1     | 3.911    | 6.014    | 15.93        |
| 4.0     | 3.908    | 5.991    | 15.85        |
| 6.0     | 3.901    | 5.933    | 15.64        |
| 7.6     | 3.896    | 5.889    | 15.48        |
| 9.0     | 3.891    | 5.875    | 15.40        |
| 9.8     | 3.885    | 5.862    | 15.32        |
| 10.5    | 3.884    | 5.860    | 15.31        |
| 11.0    | 3.878    | 5.849    | 15.23        |
| 11.6    | 3.878    | 5.850    | 15.24        |
| 12.1    | 3.871    | 5.841    | 15.16        |
| 12.7    | 3.869    | 5.837    | 15.13        |
| 13.6    | 3.8(85)  | 5.766    | 15.07        |
| 14.5    | 3.8(79)  | 5.736    | 14.95        |
| 15.8    | 3.8(76)  | 5.712    | 14.86        |
| 17.1    | 3.8(75)  | 5.678    | 14.77        |
| 18.0    | 3.8(68)  | 5.660    | 14.67        |

Cell volumes are reported as cubic Angstroms
per number of atoms (Z) in the primitive cell.

Secondly, $La_2O_3$ does not undergo isotropic strain even under hydrostatic stress.  That

is, the c-axis is more compressible than the a-axis.  This will cause a misfit to the data

because the Vinet equation of state describes a solid undergoing isotropic strain as a

function of hydrostatic stress and this is not the case here.  The Birch-Murnaghan

equation of state was also used to model the compression data for which similar results were obtained.
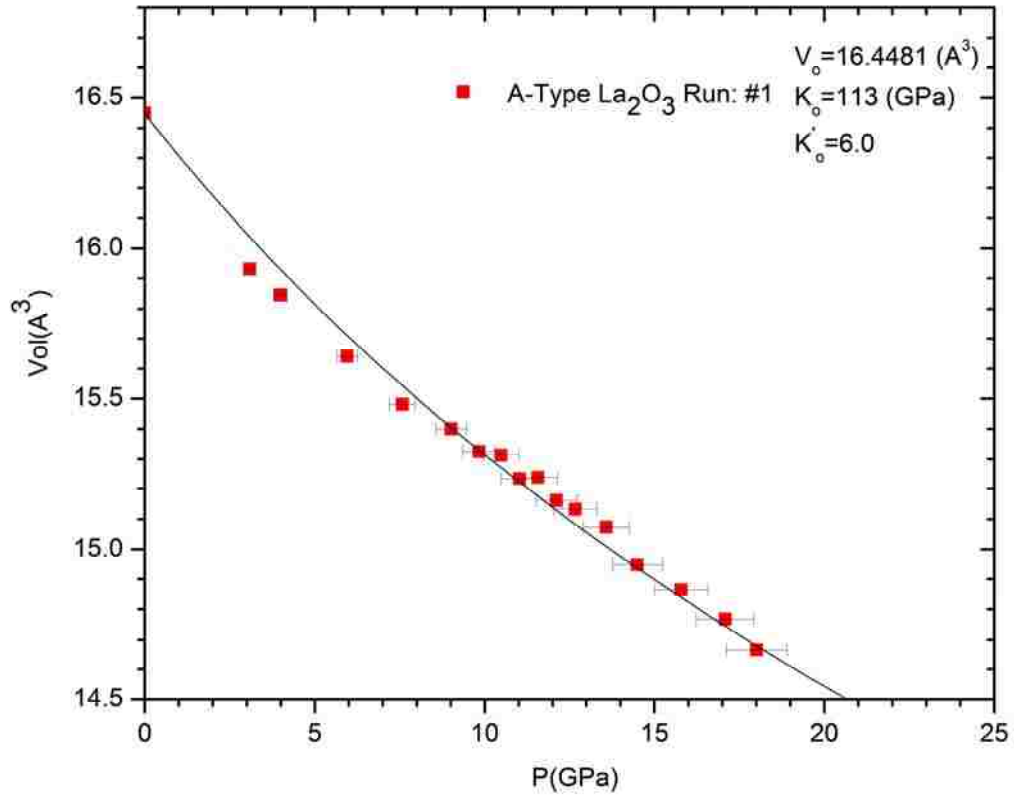


Figure 4.3 Volume versus pressure equation of state of $La_2O_3$.

### 4.1.2 $Sm_2O_3$

A total of eight compression studies were performed on $Sm_2O_3$. However, only three of which, labeled $Sm_2O_3$ Experimental Run: #1, #2, and #3 were successful. Difficulties in the preparation of polycrystalline $Sm_2O_3$ led to samples containing large amounts of the monoclinic B-type phase along with the cubic C-type phase that was of interest. $Sm_2O_3$ must be sintered at temperatures above 1000 $^o$C for at least 24 hrs in order to drive off water and other impurities in the material. After sintering, if the material is quenched

to room temperature by immediate removal from the oven, the high temperature monoclinic phase is stabilized.  X-ray diffraction analysis of the quenched samples indicated nearly 100% phase fraction of monoclinic B-Type $Sm_2O_3$.  This problem is avoided by annealing the sample at approximately 700 $^o$C for period of 24 hrs.  Samples prepared in this fashion were confirmed by X-ray diffraction analysis to contain nearly 100% the C-Type sesquioxide phase.  However, small amounts of $Sm(OH)_3$ were present in most samples because of the extreme hygroscopic nature of the material.

Figure 4.4 shows X-ray diffraction patterns from $Sm_2O_3$ Experimental Run: #3 collected at HPCAT's 16 ID-B beam line with a focused X-ray beam of wavelength 0.353144 angstroms.  In this run, argon was used as the pressure transmitting medium and the sample was compressed to a maximum pressure of 12 GPa.   Enlarged in figure 4.5, the evolution of the phase transition in $Sm_2O_3$ from the C-Type to A-Type structure is clearly seen.  At 4.3 GPa, the A-Type phase has already begun to form but is not very apparent from the diffraction patterns.  At 6.8 GPa the A-Type phase is quite prominent as indicated by the upward pointing arrows.  Asterisks indicate diffraction peaks from the argon pressure medium.  At 12 GPa there is full transformation to the A-Type phase.  Additionally, there exists a pressure regime, between approximately 4 to 12 GPa, where the two phases are seen to coexist.

Figure 4.6 shows the data collected on $Sm_2O_3$ Experimental Run #2 at HPCAT's 16 ID-B with X-ray wavelength of 0.413561 angstroms.  This plot shows the evolution of the diffraction data up to approximately 40 GPa.  Diffraction peaks similar in d-spacing to the A-Type phase, seen in Figure 4.5, are present in $Sm_2O_3$ up to 40 GPa. However, given the continuous broadening of the diffraction peaks widths, it is not clear that the
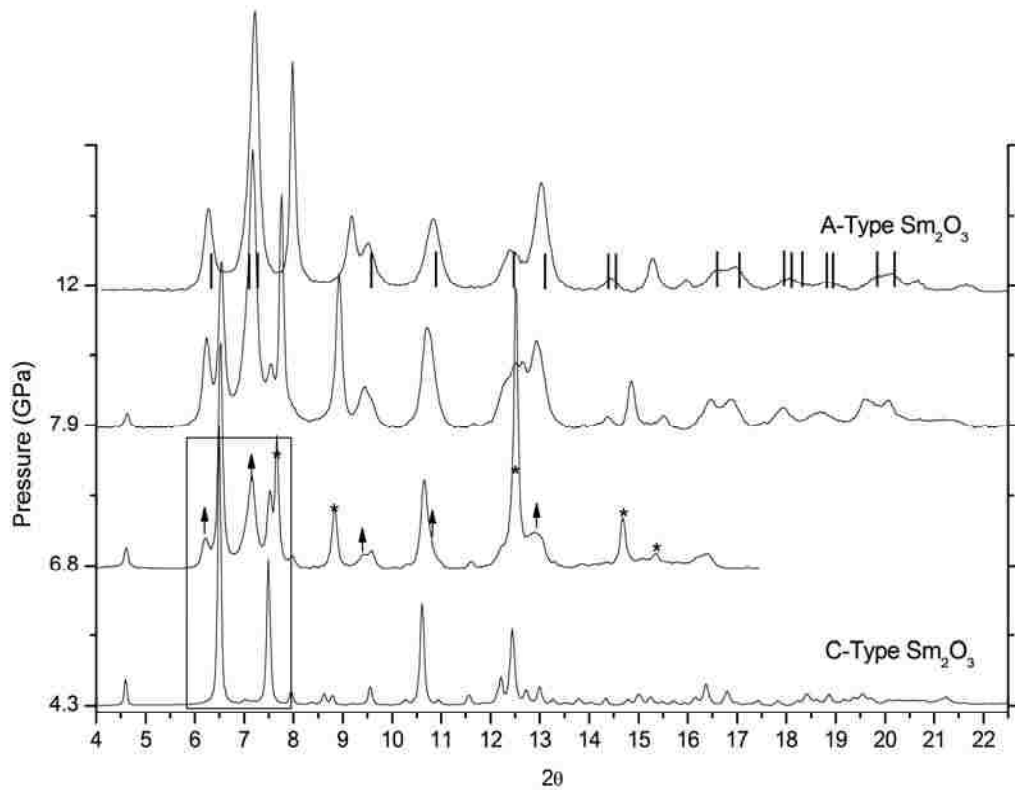
Figure 4.4 X-ray diffraction patterns collected from $Sm_2O_3$ Experimental Run: #3.
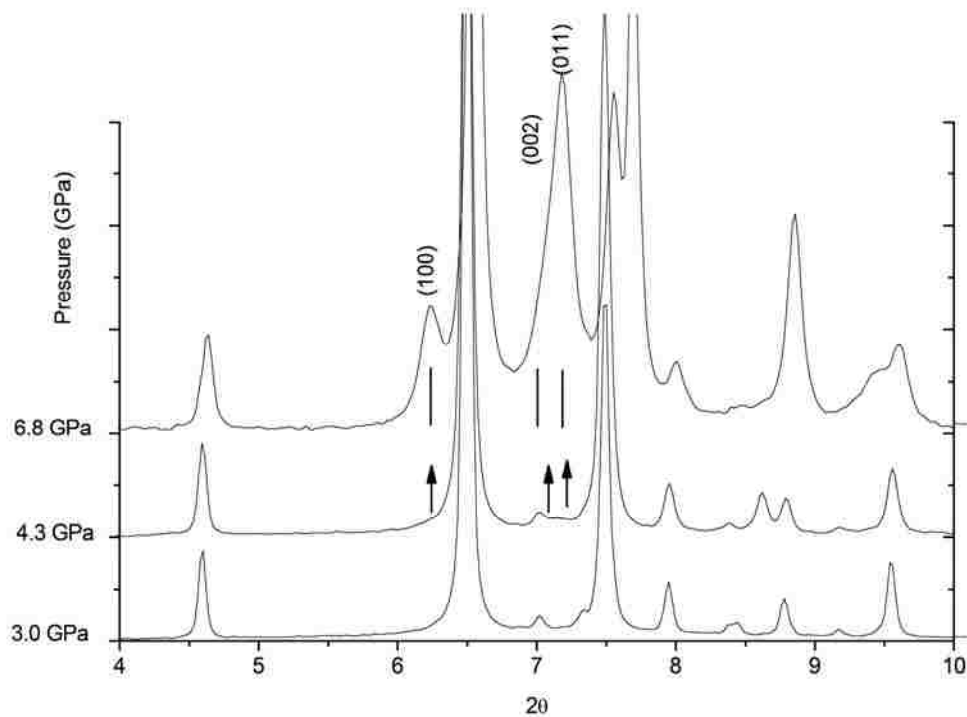


Figure 4.5 X-ray diffraction patterns collected from $Sm_2O_3$ Experimental Run: #3 zoomed in region from figure 4.4.

A-type sesquioxide phase in $Sm_2O_3$ is stable throughout the pressure range investigated. It was originally thought that the broadening observed in the diffraction peak profiles, seen in A-type $Sm_2O_3$, might be the result of non-hydrostatic stressed imparted to the sample from the argon pressure medium. This issue is revisited in section 4.1.4 with $Gd_2O_3$ and is confirmed not to be the case.

Figure 4.7 displays the P-V EOS data for $Sm_2O_3$ Experimental Runs 1-3. The dotted line at 4.3 GPa indicates the onset of the phase transition to the A-Type sesquioxide phase. The Vinet equation of state is used to model the compression data in both phases. Similar to the Vinet EOS fit to A-type $La_2O_3$, it is seen here that the Vinet model again fails to accurately represent the high pressure data for the A-Type $Sm_2O_3$ phase.

All extracted lattice constants for $Sm_2O_3$ Experimental Runs 1-3 are listed in the Appendix.

### 4.1.3 $Eu_2O_3$

Two compression studies are performed on $Eu_2O_3$ covering the pressure range of 0.69 to 16.3 GPa referred to as $Eu_2O_3$ Experimental Run #1 and #2. The first experimental run is performed on the B2 beamline at CHESS using a collimated X-ray beam of wavelength 0.61992 angstroms. The pressure transmitting medium used is $N_2$ and annealed ruby spheres are used as pressure markers. Pressure was increased in approximately 1 GPa increments up to 8 GPa in an effort to determine more accurately where the phase transition to the A-Type sesquioxide structure begins. $Eu_2O_3$ Experimental Run #2 is a
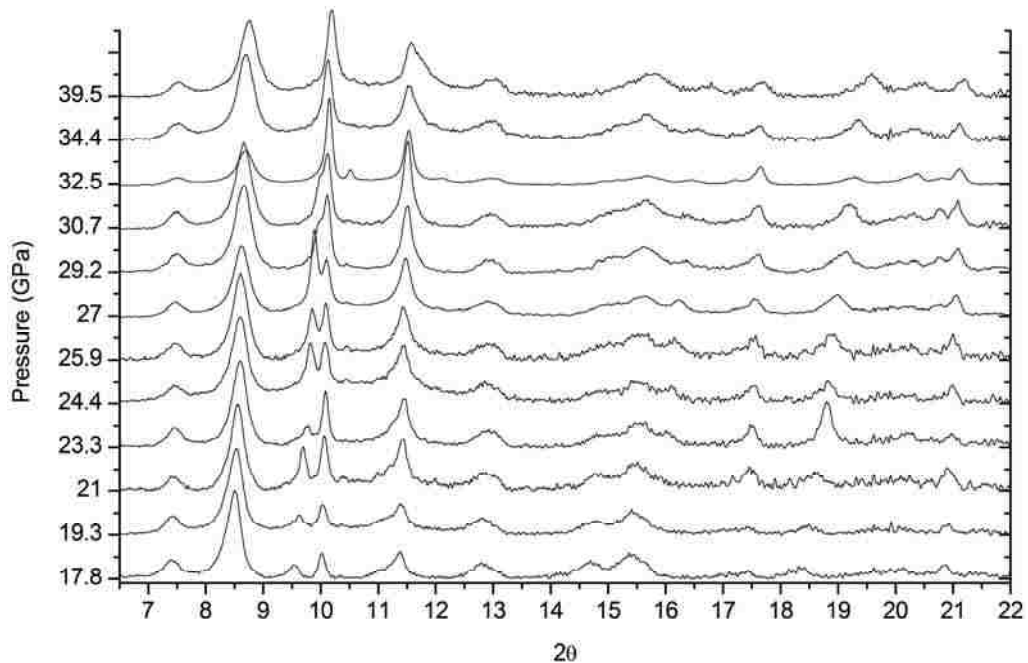
Figure 4.6 X-Ray diffraction patterns from $Sm_2O_3$ Experimental Run #2.
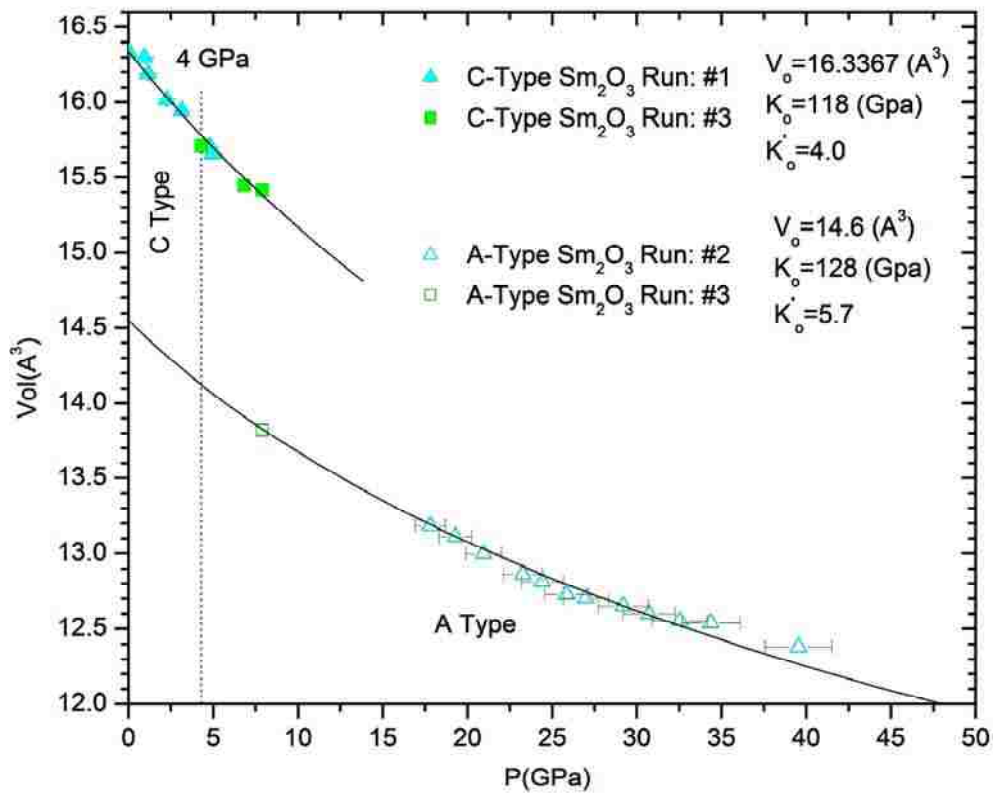


Figure 4.7 Volume versus pressure equation of state of $Sm_2O_3$.

continuation of the previous run, however, the diffraction data is collected at HPCAT's

16 ID-B beamline at the APS using a focused X-ray beam of wavelength 0.368194

angstroms.

Figure 4.8 shows the diffraction data collected from $Eu_2O_3$ Experimental Run #1.

Upward arrows indicate initial observation of the phase transition. At 5.1 GPa there is an

increase in diffracted intensity in the 2-theta range coinciding to the peak position of the

(002) lattice plane in the A-Type phase. However, it is not ultimately clear that the new

phase is forming until 7.1 GPa. The onset of the C to A-type phase transition is taken to

be 6 GPa +/- 1.5 GPa.

The rectangular area in figure 4.8 is enlarged in figure 4.9 providing a clearer image of

the diffraction patterns in the vicinity of the phase transition. The three most intense

peaks are assigned to the (100), (011), and (002) diffraction planes in the A-Type

structure. Drop lines indicate the best known centroid positions of the diffraction peaks

belonging to the A-type phase.

Diffraction patterns from $Eu_2O_3$ Experimental Run #2 are shown in figure 4.10. The

C-type phase is observed to be in coexistence with the newly forming A-type phase from

6 to 14 GPa. At approximately 14 GPa the $Eu_2O_3$ sample has completely transformed to

the A-Type phase. The peak profiles belonging to the A-type phase, again, appear very

broad in comparison to the C-type parent phase.
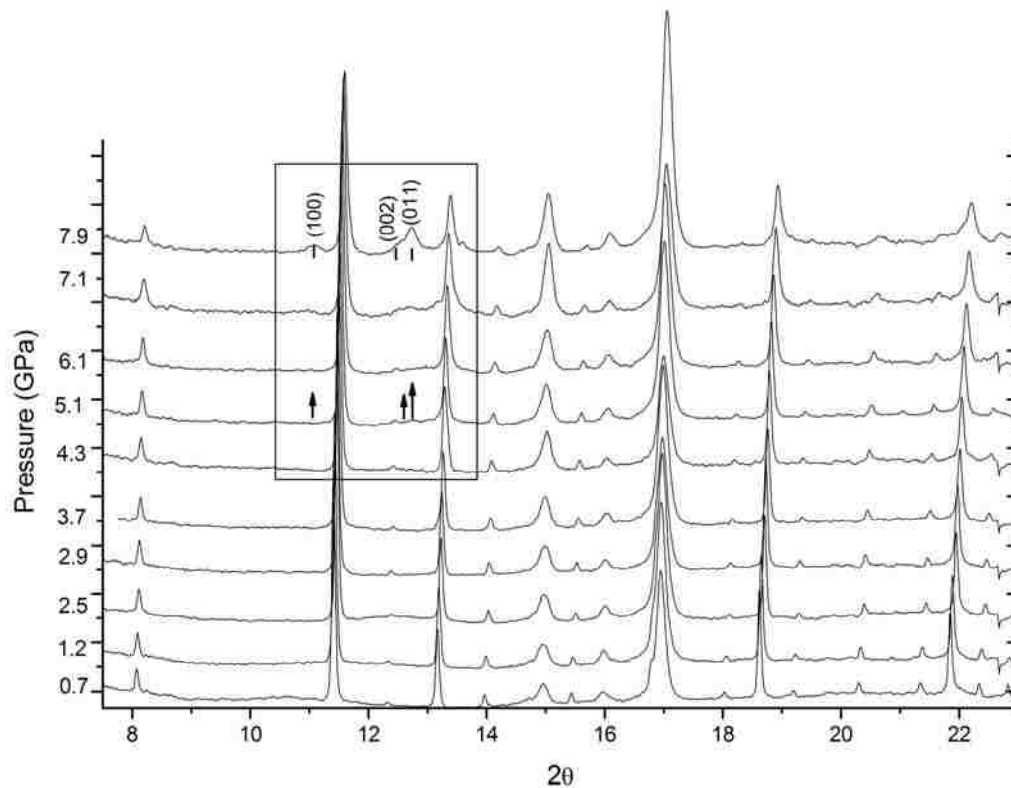
Figure 4.8 Diffraction of $Eu_2O_3$ Experimental Run #1. Upward arrows indicate the initial observation of the A-Type phase. An enlargement of the region in the vicinity of the phase transition is shown to the right.

Figure 4.11 shows all of the compression data collected on $Eu_2O_3$ where the fit to the data is from the Vinet equation of state. The dotted line at 6 GPa indicates the pressure where the transition to the A-type phase begins. Lattice constants for $Eu_2O_3$ Experimental Runs #1 and #2 are located in the Appendix.

86
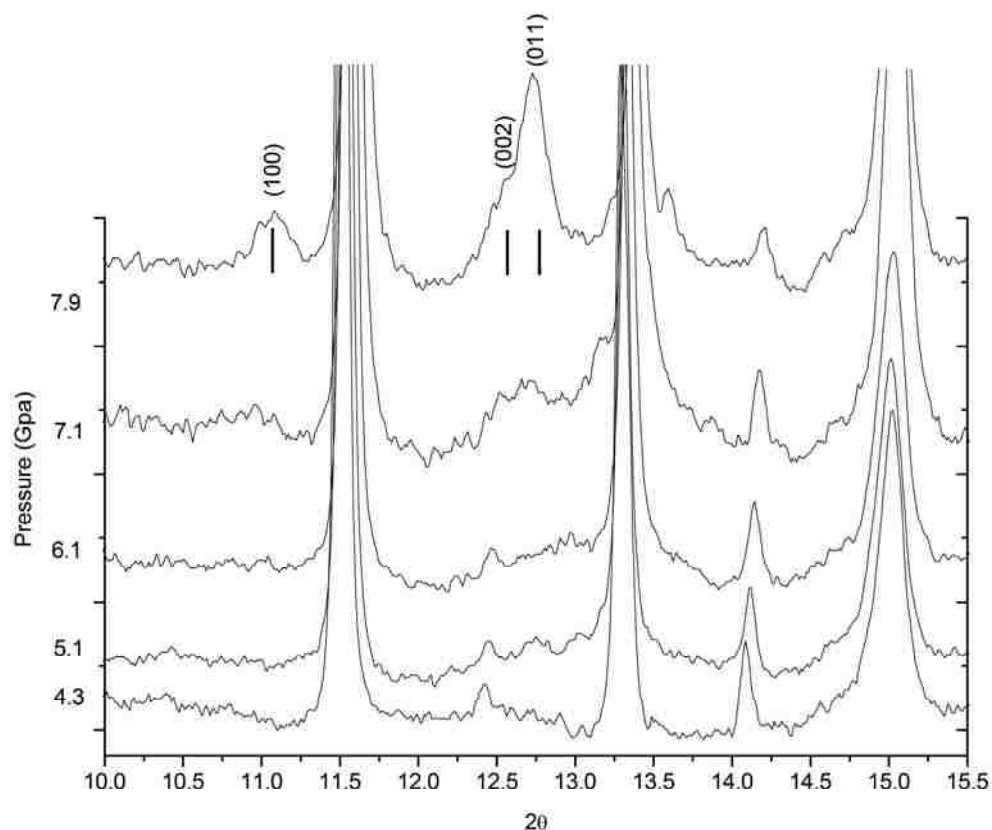
Figure 4.9 Enlargement of the diffraction patterns of $Eu_2O_3$ in Experimental Run #1.
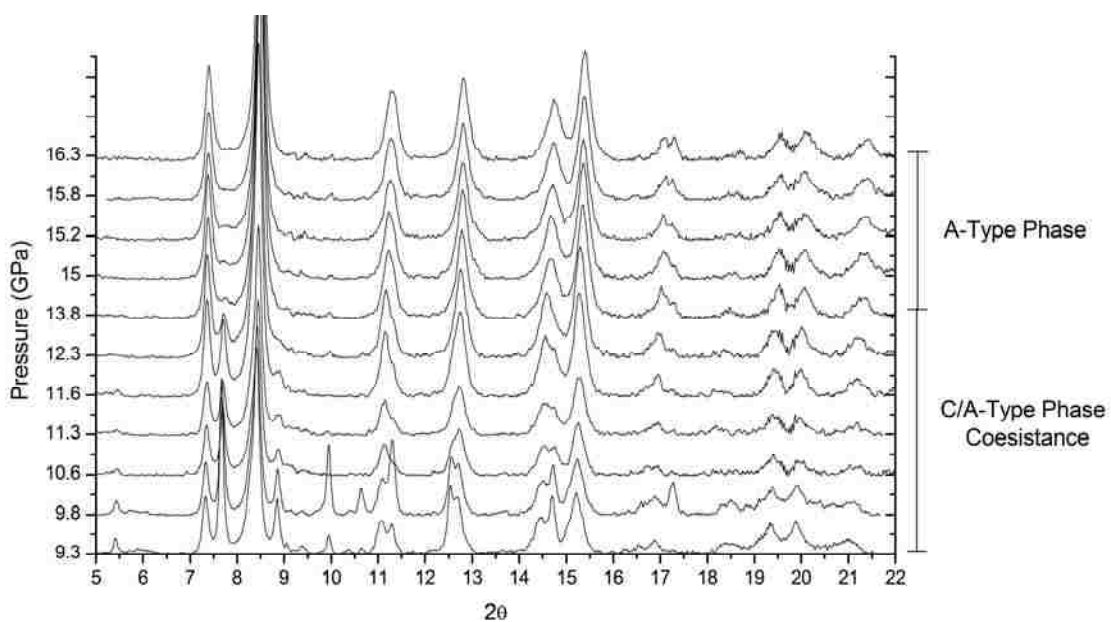


Figure 4.10 Diffraction patterns from $Eu_2O_3$ Experimental Run #2.  Diffraction peaks from the C-Type phase are present up to 14 GPa as indicated by the bars on the right side of the graph.
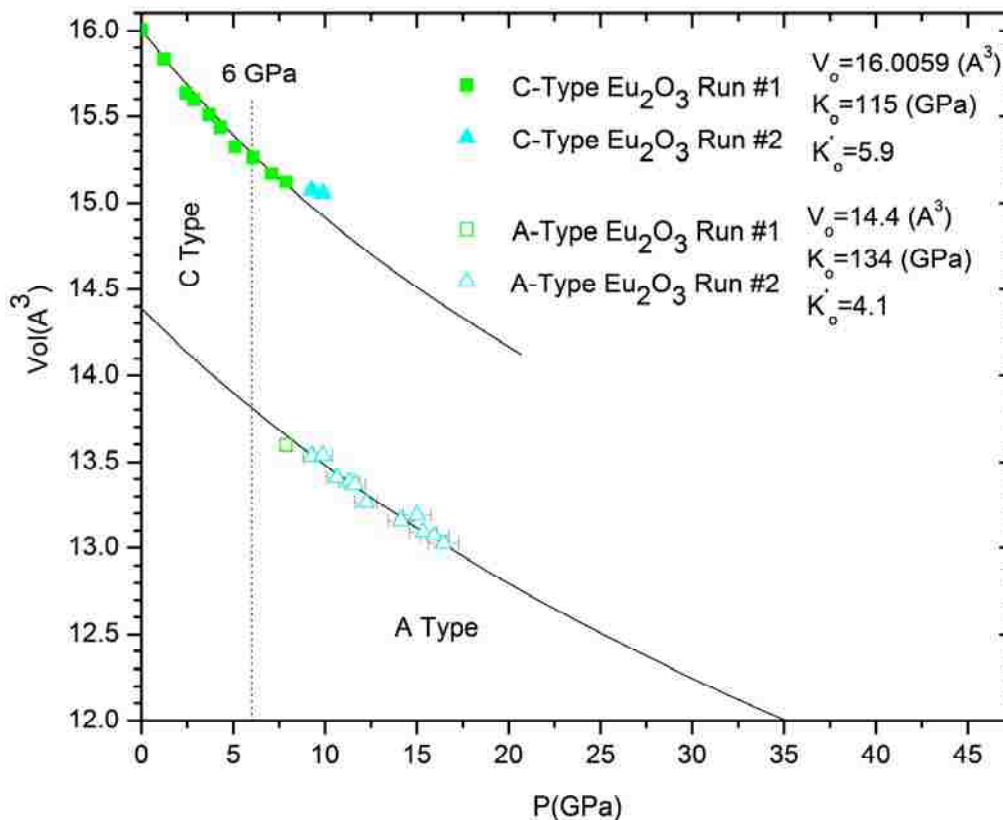
Figure 4.11 Volume versus pressure equation of state of $Eu_2O_3$.

### 4.1.4 $Gd_2O_3$

Five compression studies are performed on $Gd_2O_3$ achieving a maximum pressure of 77 GPa. $Gd_2O_3$ Experimental Runs #1-#4 are performed collected at HPCAT's 16 ID-B beamline at the APS using a focused X-ray beam of wavelength 0.41356, 0.41356, 0.368194, 0.39310 angstroms respectively. $Gd_2O_3$ Experimental Run #5 is performed on B2 at the CHESS facility using a collimated X-ray beam of wavelength 0.61992 angstroms. Argon is used a pressure transmitting medium in Runs #1, #2, and #4. Helium and nitrogen are used as pressure transmitting media for Runs #3 and #5 respectively. Annealed ruby spheres are used as pressure markers in all runs and Pt is used as a diffraction pressure marker in run #4.

Figure 4.12 shows the power diffraction data collected in $Gd_2O_3$ Experimental Run #5.

Nitrogen is used as the pressure transmitting medium for this experiment and the pressure

limit is set at 11 GPa.  In order to better determine the phase transition pressure, an

average pressure increase of 0.4 GPa is applied between data points.  The trend from the

previous experiments on $Sm_2O_3$ and $Eu_2O_3$ suggest that the phase transition in $Gd_2O_3$

should occur around 8 GPa.  This is based on the prediction that the phase transition

pressure should increase linearly with the 4f electron occupation number.

The onset of the phase transition to the A-Type sesquioxide structure in $Gd_2O_3$ is seen

at approximately 7 +/- 1.5 GPa.  The enclosed rectangular region in figure 4.12 is

enlarged in figure 4.13 so that features in the diffractions patterns pertaining to the

identification of the A-type phase may be seen.  Miller indices are placed above upward

pointing arrows to indicate the appearance of diffraction peaks from lattice planes

belonging to the A-type phase.
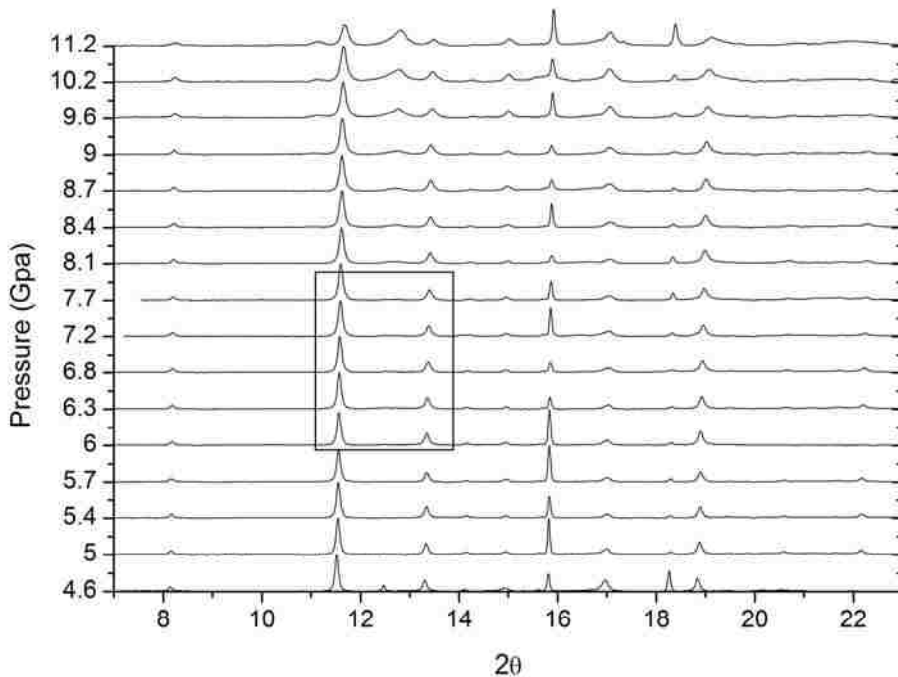


Figure 4.12 Diffraction patterns of $Gd_2O_3$ Experimental Run #5.  A nitrogen pressure transmitting medium is used and the material compressed up to 11 GPa.
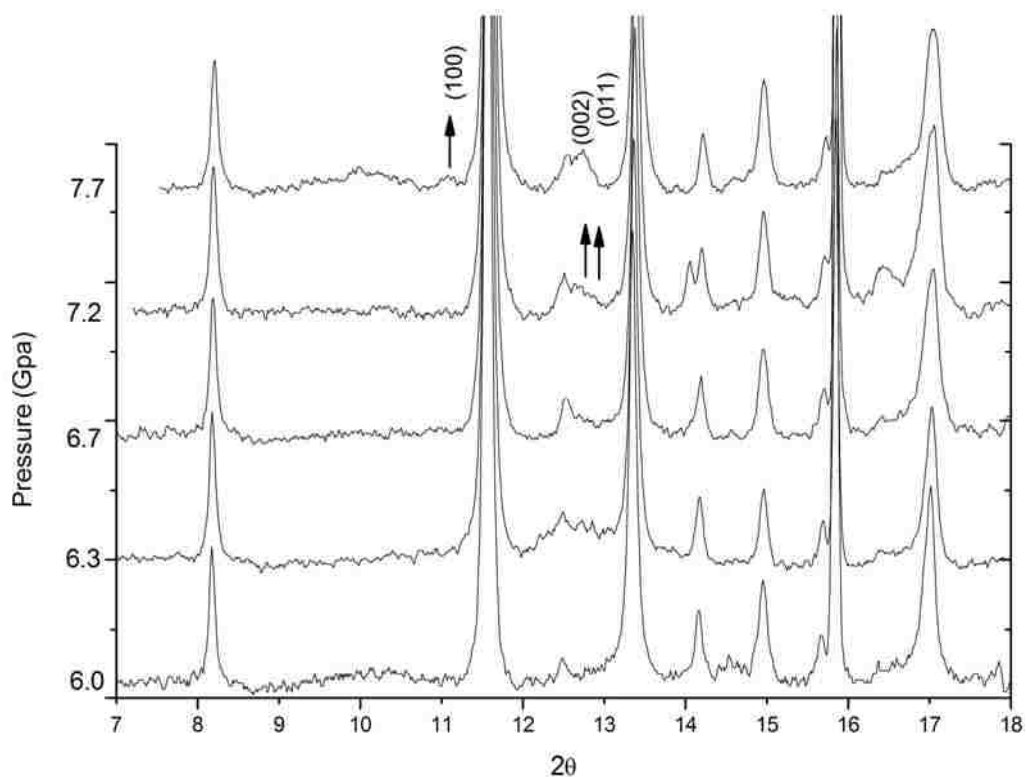
Figure 4.13 Enlargement of the diffraction patterns of $Gd_2O_3$ Experimental Run #5. Upward arrows indicate peaks indexed to the A-Type phase.

In $Gd_2O_3$ Experimental Run #4, an argon pressure transmitting medium is used and the experiment terminated at approximately 77 GPa. Figure 4.14 shows the diffraction data collected in $Gd_2O_3$ Experimental Run #4 for pressures up to 18.4 GPa. It is seen that there is a phase coexistence of the C and A-type phases between 7.0 and 15.7 GPa. At 17.1 GPa, only the A-Type phase is detectable via X-ray diffraction. The diffraction peak widths have also increased significantly through the phase transition. It was thought that non-hydrostatic conditions in the sample chamber might be causing the profile broadening, however, later experiments using Helium as a pressure transmitting medium rule this out.

Figure 4.15 shows a plot of the pressure difference measured across the sample as a function of pressure. This measurement is made by placing a ruby sphere on either side of the sample (a distance of about 35um) and recording the wavelength shift in the $R_1$ line. It is seen in the region where the A-Type phase is forming (7-15.7 GPa), that the pressure difference is below 0.1 GPa indicating the presence of only a small pressure gradient across the sample. At approximately 20 GPa there is a sharp increase in the pressure difference measured across the sample, however, no obvious changes are observed in the diffraction patterns in the vicinity of this pressure.
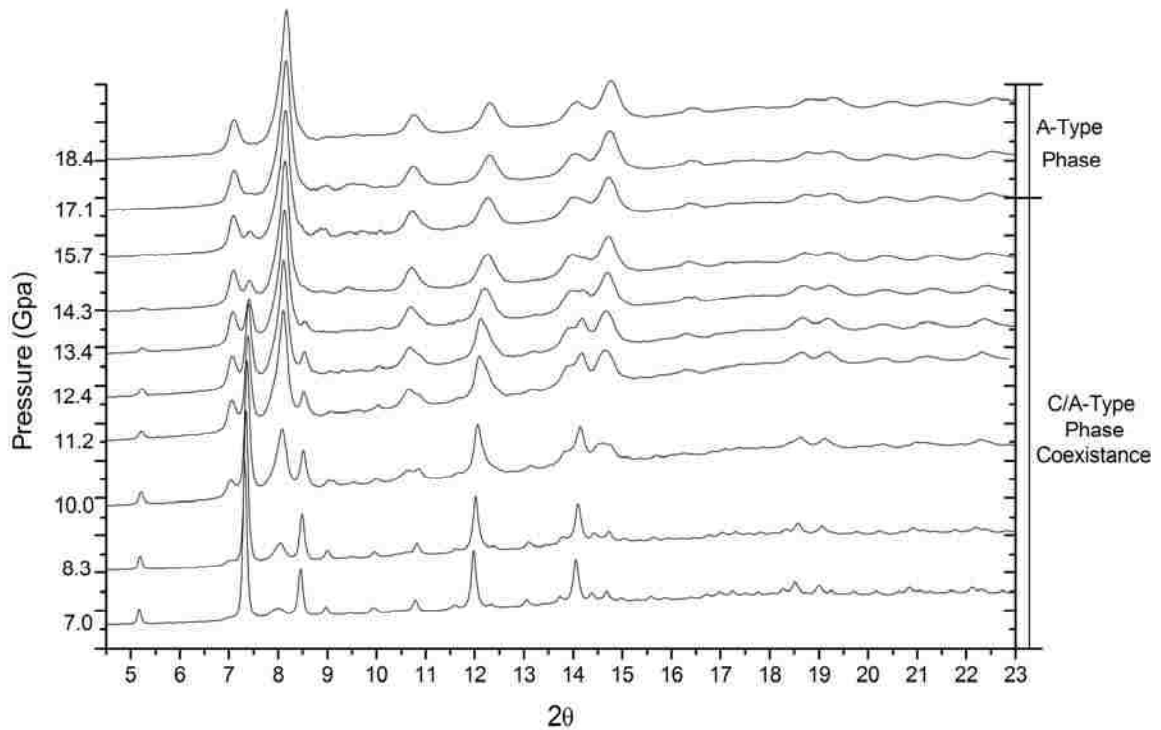


Figure 4.14 Diffraction patterns up to 18.4 GPa for $Gd_2O_3$ Experimental Run #4.
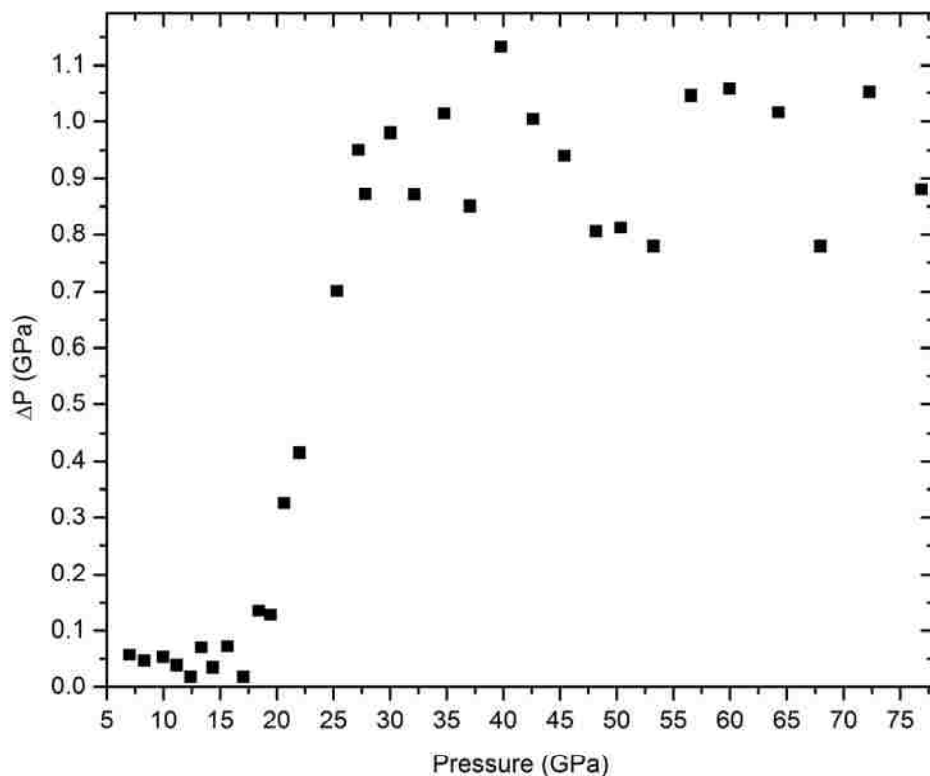
Figure 4.15 Pressure difference measured across the sample for $Gd_2O_3$ Experimental Run #4.

Diffraction patterns up to 76.9 GPa for $Gd_2O_3$ Experimental Run #4 are shown in

Figure 4.16. The diffraction peak widths continue to broaden only slightly as pressure is

increased. At 30 GPa, a diffraction peak from Pt is seen at 10 degrees 2-thetta. Given

the relatively sharp peak profiles observed for Pt under these stress conditions, it is

believed that the peak broadening seen in $Gd_2O_3$ must be dominated by structural effects.

In $Gd_2O_3$ Experimental Run #3, a helium pressure transmitting medium is introduced

into the sample chamber using the high pressure gas loading device at the CHESS

facility. Because of difficulties encountered during the loading process, the cell was

initially pressurized to 16.8 GPa. The experiment is then preformed as a pressure release

from this point down to 3.7 GPa.
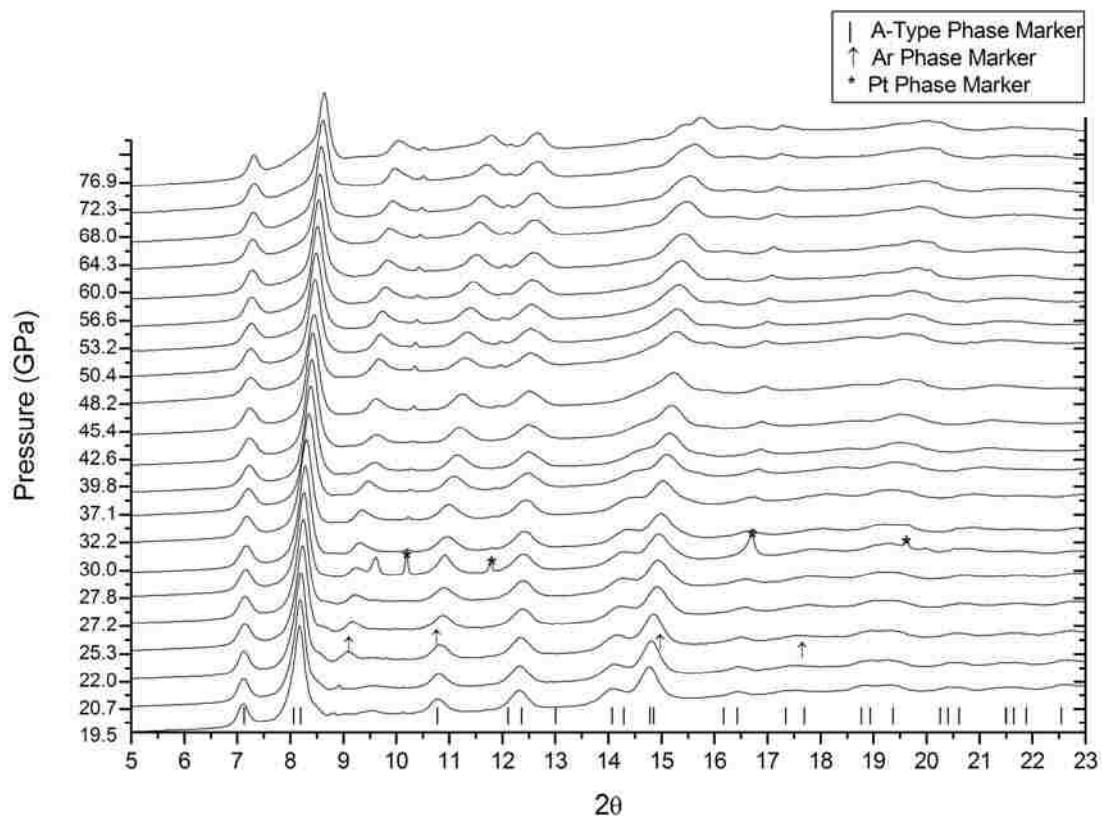
Figure 4.16 Diffraction patterns for $Gd_2O_3$ Experimental Run #4. Diffraction peaks from the A-Type phase, Ar, and Pt are marked with vertical lines, arrows and asterisks above the respective plot.

Figure 4.17 shows diffraction patterns of $Gd_2O_3$ compressed by a helium pressure transmitting medium. Up to 11 GPa, helium is a fluid and above which it forms a very soft van der Waals solid making it the most ideal pressure medium for these experiments, see table 2.1.

At 16.8 GPa, the diffraction patterns show complete conversion of $Gd_2O_3$ to the A-Type sesquioxide phase. There is no observation of the B or C-Type sesquioxide phase down to 3.7 GPa. Diffraction peak profiles of A-Type $Gd_2O_3$ transformed by hydrostatic compression using a helium pressure medium are observed to be as broad as in the cases where $N_2$ and Ar are used.
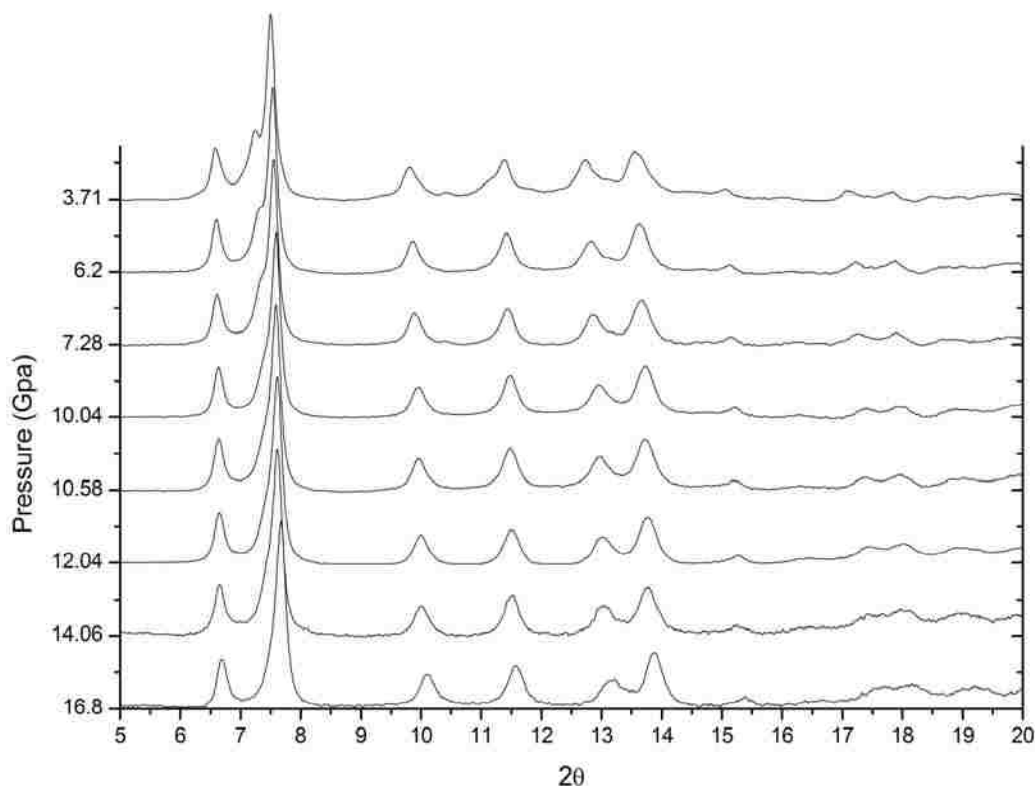
Figure 4.17 Diffraction patterns from $Gd_2O_3$ Experimental Run #3. Helium is used a pressure transmitting medium. Only the A-Type sesquioxide phase is observed throughout the entire experiment.

In Figure 4.18, a direct comparison between diffraction patterns of A-Type $Gd_2O_3$ compressed by helium and argon pressure transmitting media are shown as thick red and thin blue dashed lines respectively. Pt peaks are labeled in the pattern collected at 28 GPa, as compressed by an argon pressure medium, are seen to be much sharper than diffraction peaks from A-Type $Gd_2O_3$. This is an indication that applied stress on the Pt pressure calibrant and $Gd_2O_3$ sample should be quasi-hydrostatic. In the case where helium is used as the pressure medium the diffraction profiles are equally as broad as when argon is used. This adds further support that the observed peak broadening in the A-type RES compounds is the result of a structural anomaly rather than a response to the applied stress.
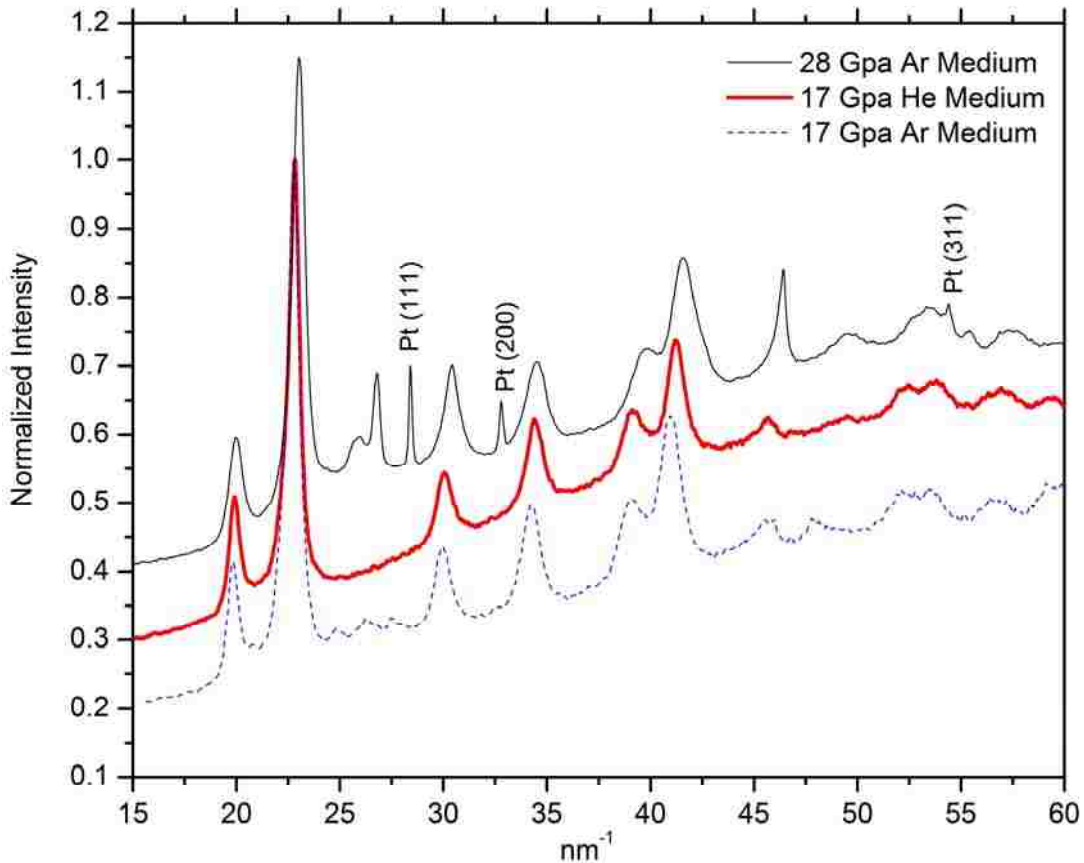
Figure 4.18 Diffraction patterns of A-Type $Gd_2O_3$ compressed using helium and argon pressure media in separate experiments. The thick and thin dashed curves are from experiments where He and Ar are used as pressure media respectively at approximately 17 GPa. The thin curve is diffraction of $Gd_2O_3$ in the A-Type phase at 28 GPa and Pt peaks are labeled.

Rietveld refinements are carried out on all diffraction patterns from $Gd_2O_3$ Experimental Runs #1, #4, and #5 using GSAS. Figure 4.19 displays all of the pressure-volume data from these experiments used in determining equation of state parameters for $Gd_2O_3$ where the fit to the data is from the Vinet equation of state. The dotted line indicates the point where the A-Type sesquioxide phase is beginning to form. Tables of all lattice constants are located in the Appendix.
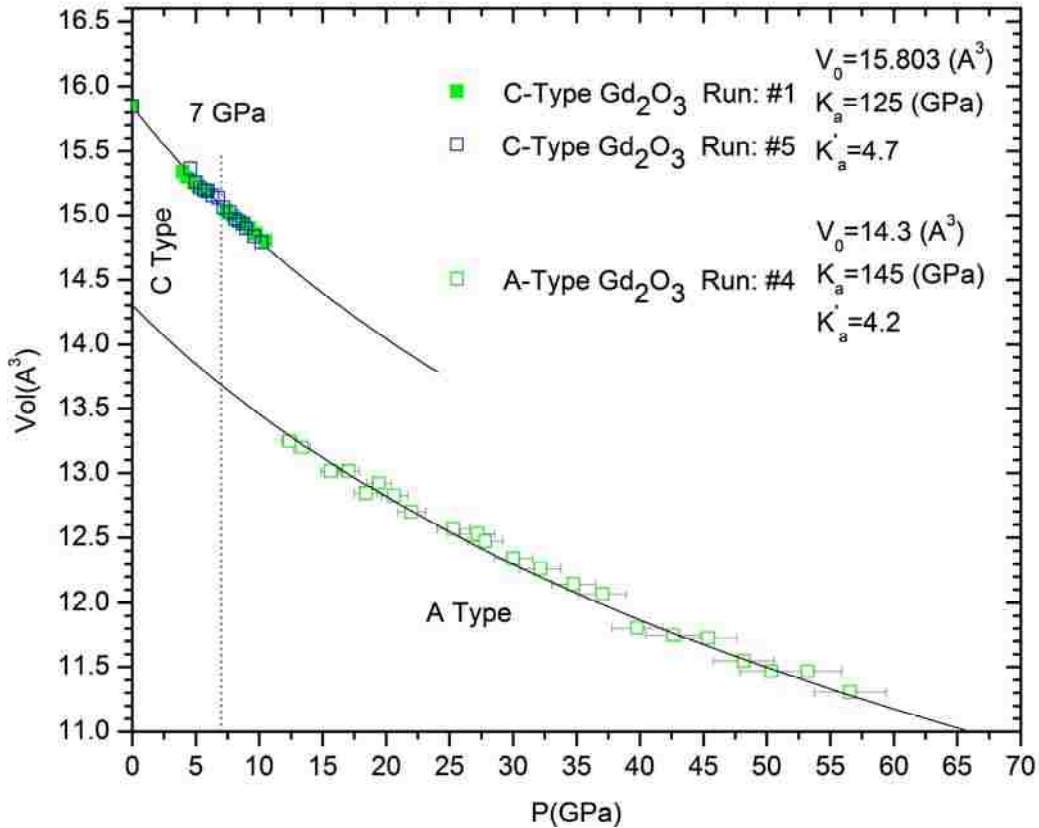
Figure 4.19 Volume versus pressure equation of state for $Gd_2O_3$.

### 4.1.5 $Er_2O_3$

One compression study is performed on $Er_2O_3$ covering the pressure range of 1.7-17.2 GPa referred to as $Er_2O_3$ Experiment Run #1. This experimental run was conducted at sector 16 BM-D of the Argonne National Lab. Energy dispersive X-ray diffraction patterns were collected using a liquid nitrogen cooled Ge detector. A fixed 2-theta angle of 12.000 degrees is used and the entrance slits to the detector set to approximately 100 μm.

The sample is loaded into a 50 μm thick by 90 μm diameter Rhenium gasted DAC and nitrogen used as a pressure transmitting medium. Ruby spheres are used as pressure markers. Figure 4.20 displays all of the diffraction patterns collected in this experimental

96

run and the phase transition to the A-type phase is seen to occur at approximately 14 GPa. Figure 4.21 is an enlargement of the diffraction patterns near transition point where upward arrows are indicating the features from the presence of the A-Type sesquioxide phase.
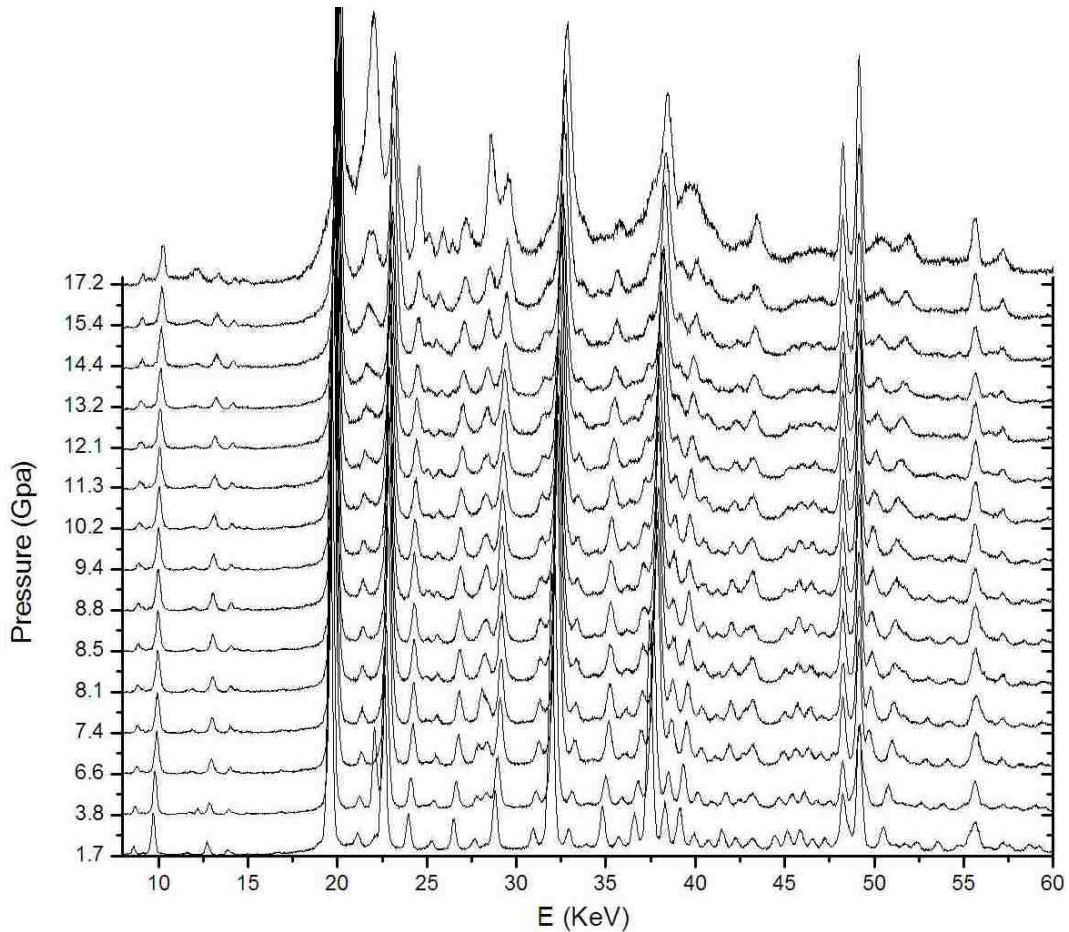


Figure 4.20 Energy dispersive X-ray diffraction patterns from $Er_2O_3$ Experiment Run #1 up to 17.2 GPa.

Lattice constants for the C-Type phase are refined in a least squares manner and the results tabulated in the Appendix. The volume as a function of pressure equation of state is determined for $Er_2O_3$ by refining the bulk modulus $K_0$ and derivative of the bulk

modulus Ko' using the Vinet equation of state. The results of this calculation and the accompanying data are displayed in Figure 4.22.
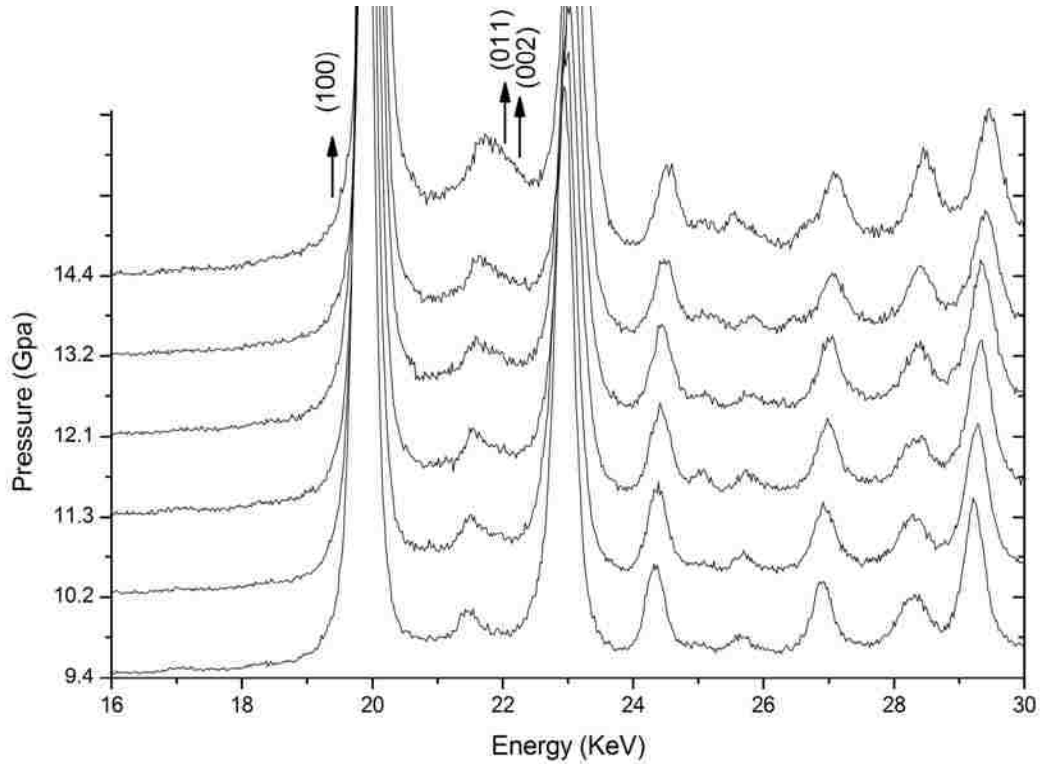


Figure 4.21 Enlargement of the diffraction patterns near the phase transition pressure in $Er_2O_3$ Experiment Run #1. Upward arrows indicate the emergence of the A-Type sesquioxide phase.

### 4.1.6  Yb$_2$O$_3$

One compression study on $Yb_2O_3$, referenced as $Yb_2O_3$ Experimental Run #1, is

conduced at the Argonne National Lab's sector 16 ID-B using a focused X-ray beam of

wavelength 0.49594 angstroms. Angularly dispersive X-ray diffraction data is collected

from a Rhenium gasted DAC having a sample chamber measuring 60 μm thick by 130

μm diameter. Ruby spheres are used as an internal pressure marker.
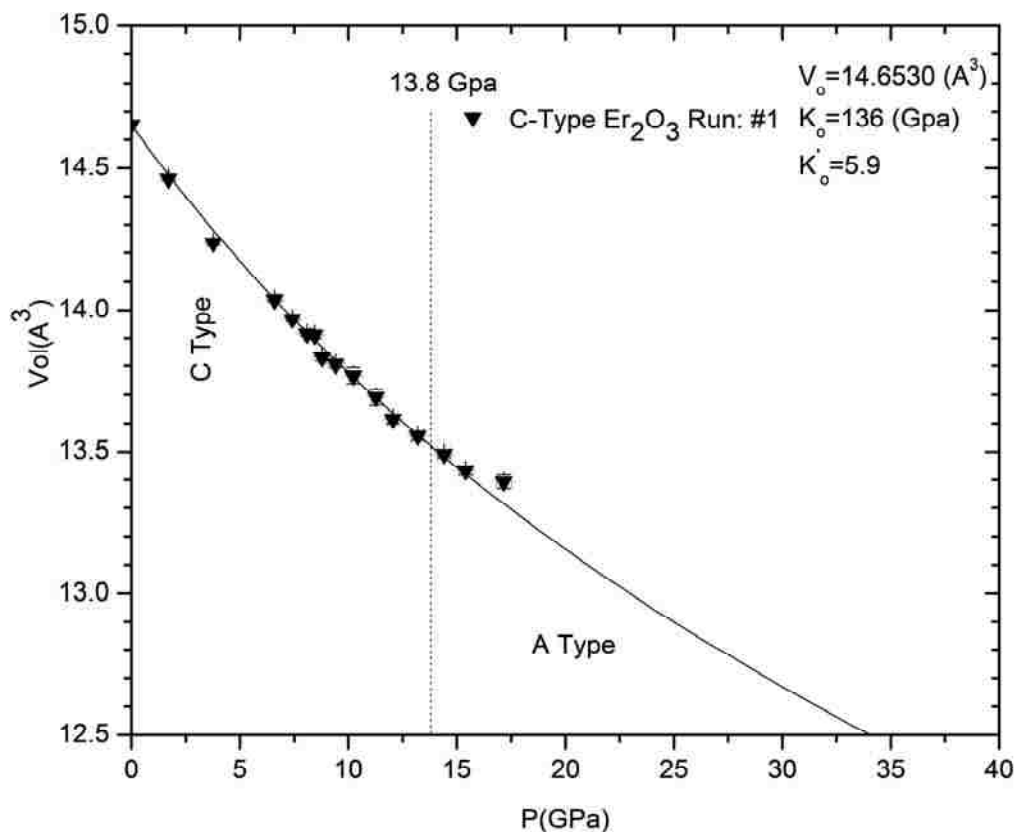
Figure 4.22 Volume versus pressure equation of state for $Er_2O_3$.


Figure 4.23 is a plot of diffraction patterns collected on $Yb_2O_3$ up to 26.5 GPa. Indicated by upward arrows are new feature in the data seen initially around 17 GPa.

A phase transition seen to occur at 17 GPa, however, the diffraction data show a poor fit to the A-Type sesquioxide structure. Rather, the data indicate a slightly better fit to the B-Type sesquioxide model. Shown in Figure 4.24 are the observed and calculated diffraction patterns for the A, B, and C-Type sesquioxide phases respectively at 21.4 GPa. Features in the top most graphs marked by asterisks and plus sign indicate the presence of rhenium and nitrogen respectively.
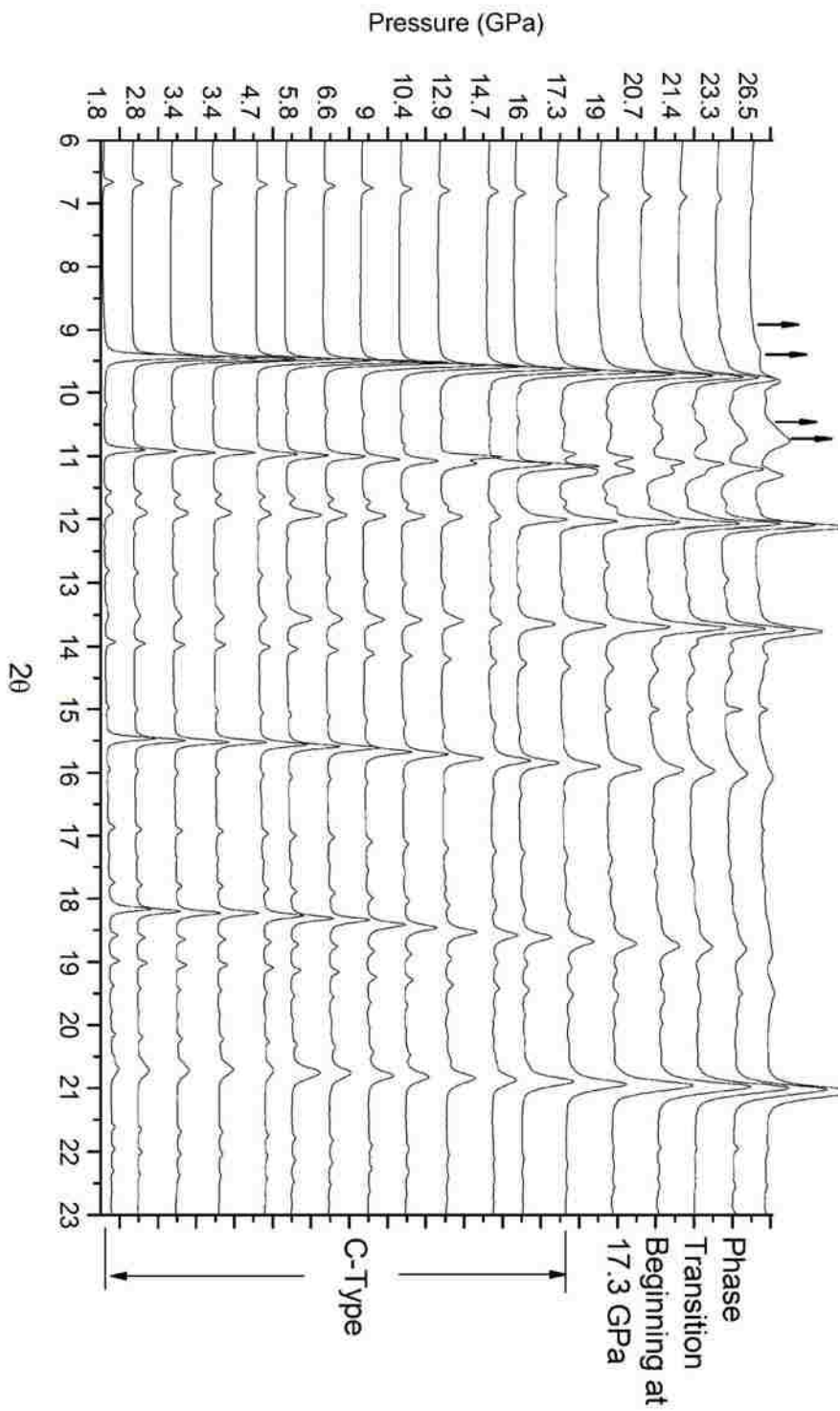
Figure 4.23 Diffraction patterns of $Yb_2O_3$ Experimental Run #1.

A significant percentage of the C-Type sesquioxide phase is still present at 21.4 GPa seen in the top graph in Figure 4.24. The middle graph indicates the calculated fit obtained for the A-Type sesquioxide phase. Evidenced by the degree to which the patterns do not overlap, it is thought that the A-Type phase has not crystallized yet at this pressure. Seen in the lower graph is the calculated B-Type sesquioxide phase. The B-Type structure model gives a better observed fit to the diffraction pattern, especially around the 10 to 12 degree 2-theta range. The calculated residual for the fit obtained using this model, however, is not so good. Combining all of the impurity phases and the B-Type sesquioxide phase in the model gives a wRp equal to 0.62. That is, statistically the calculated and observed patterns do not agree. The poor quality of the fit is partly because the degree of overlap amongst impurity phases such as nitrogen and rhenium with the unknown high pressure phase. Additionally, the diffracting volume contains only a small portion of the transformed phase making a proper refinement of the structure complicated.

Figure 4.25 is an enlargement of the calculated B-Type fit to the diffraction pattern of $Yb_2O_3$ collected at 21.4 GPa. Miller indices for each respective peak are labeled in parentheses. The intensities in the calculated B-Type fit are not very accurately matched nor are the peak positions indicating a marginal probability that the B-Type phase is really stabilized at this pressure. Because of the difficulties in determining the high pressure structure of $Yb_2O_3$ P-V EOS data are not produced.
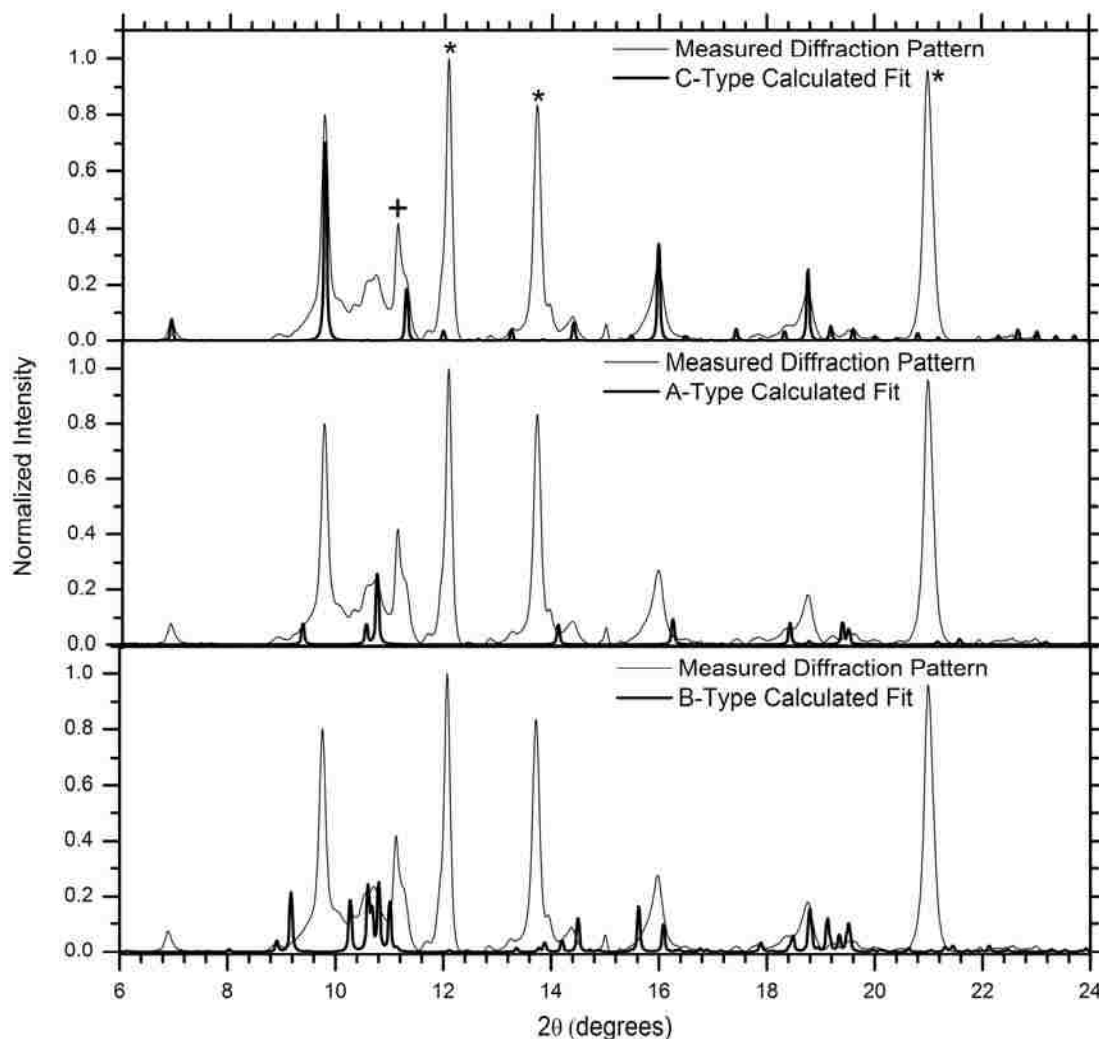
Figure 4.24 Calculated diffraction patterns for the A, B, and C-Type $Yb_2O_3$ sesquioxide structures at 21.4 GPa overlaid on observed data.

### 4.1.7 $\underline{Lu_2O_3}$

One compression study is done on $Lu_2O_3$ at sector 16 beamline ID-B of the Argonne National Lab, referenced as $Lu_2O_3$ Experimental Run #1, where a focused X-ray beam of wavelength 0.38580 angstroms is used. Angularly dispersive powder X-ray diffraction patterns are collected in a DAC up to a pressure of 16.3 GPa. Ruby spheres are used as internal pressure markers and a $N_2$ as the pressure transmitting medium. A rhenium

gasket having a sample chamber measuring 55 μm in thickness by 150 μm in diameter is used in the experiment.
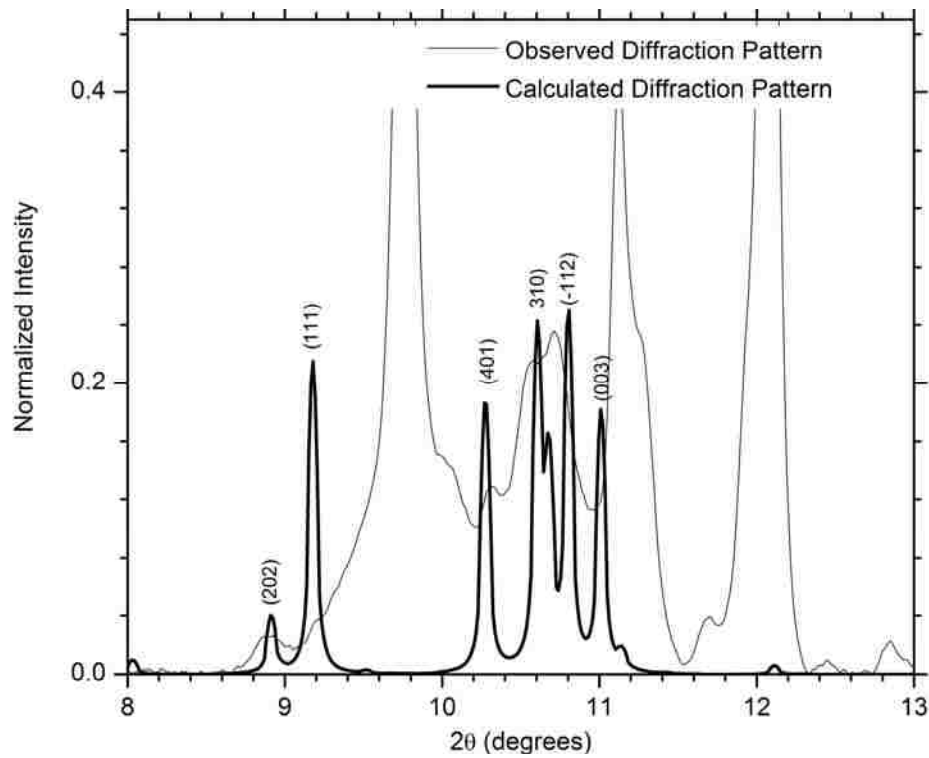


Figure 4.25 Enlargement of the diffraction patterns collected in $Yb_2O_3$ Experimental Run #1 at 21.4 GPa showing the calculated fit to the B-Type structure model.

Figure 4.26 is a plot of all of the diffraction patterns collected in $Lu_2O_3$ Experimental Run #1. The boxed in region of interest is enlarged in figure 4.27 and shows peaks belonging to the A-type phase. Upward arrows are indicating the initial appearance of these diffraction peaks and their miller indices labeled in parentheses. The phase transition is determined to occur at approximately 13.8 GPa.
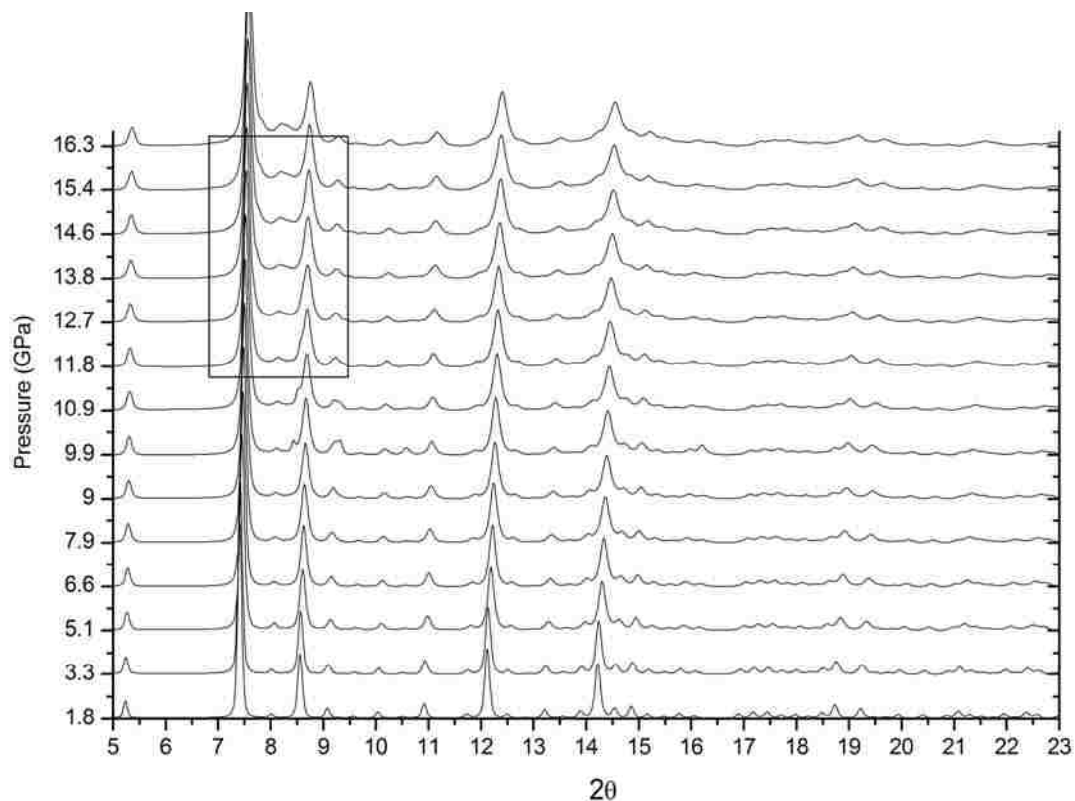
Figure 4.26 Diffraction patterns of $Lu_2O_3$ Experimental Run #1.

Because of the lack in diffraction peaks belonging to the high pressure phase seen in this compression study, it is impossible to say with complete confidence that the high pressure structure is of the A-Type. There are, however, striking similarities in the diffraction features above 14 GPa to those seen in the C to A-Type transition for $Sm_2O_3$, $Eu_2O_3$, $Gd_2O_3$, and $Er_2O_3$. This is gives evidence that the high pressure transition seen for C-type $Lu_2O_3$ is more likely to the A-Type phase and not the B-type.

Figure 4.28 is the reduction of all of the unit cell volumes for the C-Type sesquioxide phase fit to the Vinet equation of state. Least squares refinements are carried out for all data points and values for $K_0$ and $K_0$' are presented in the top right portion of the graph. The dotted line indicates the point at which the A-Type phase begins to transform. All lattice constants and unit cell volumes for $Lu_2O_3$ are tabulated in the Appendix.
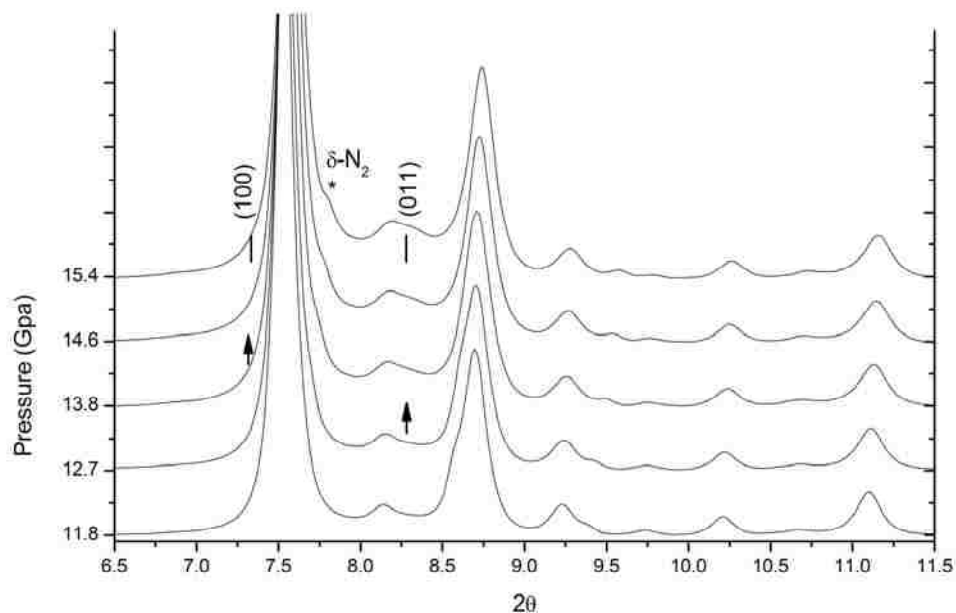
Figure 4.27 Enlargement of diffraction patterns from $Lu_2O_3$ Experimental Run #1.

### 4.1.8 $\underline{Y_2O_3}$

One compression study is done on $Y_2O_3$ at sector 16 beamline ID-B of the Argonne National Lab, referenced as $Y_2O_3$ Experimental Run #1, where a focused X-ray beam of wavelength 0.405734 angstroms is used. Angularly dispersive powder X-ray diffraction patterns are collected in a DAC up to a pressure of 34.5 GPa. Ruby spheres are used as internal pressure markers and a $N_2$ as the pressure transmitting medium. A rhenium gasket having a sample chamber measuring 50 μm in thickness by 150 μm in diameter is used in the experiment.

Figure 4.29 is a plot of all of the diffraction patterns collected in $Y_2O_3$ Experimental Run #1. C-Type $Y_2O_3$ is seen to transform to A-Type $Y_2O_3$ at a pressure near 13 GPa and coexists with the C-Type phase up to 31 GPa. Above 31 GPa the diffraction volume within the sample shows evidence only of the A-Type phase present.

105
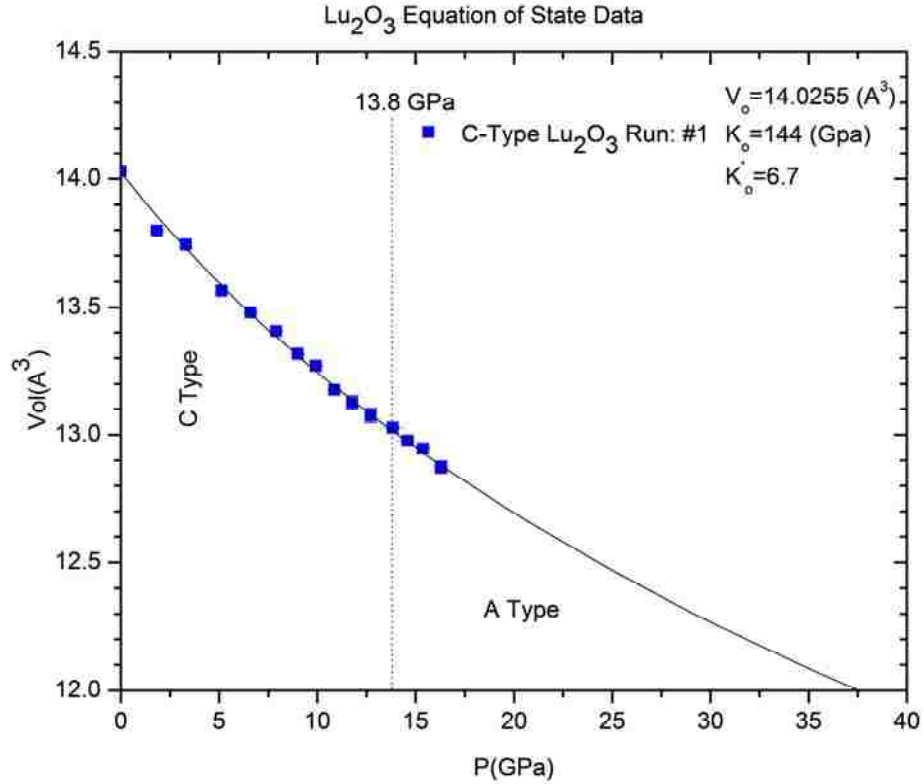
Figure 4.28 Volume versus pressure equation of state for $Lu_2O_3$.

Figure 4.30 is an enlargement of figure 4.29 over the pressure range of 12.7 to 19.8 GPa. Upward arrows at 12.7 GPa indicate the first observation of diffraction peaks associated with the A-Type sesquioxide phase. All peaks indexed to the A-Type sesquioxide phase are marked by vertical lines beneath the diffraction pattern at 19.8 GPa. Above the pattern at 19.8 GPa are the Miller indices associated with each peak.

Figure 4.31 displays the P-V EOS data from $Y_2O_3$ Experimental Run #1. Data points are plotted for the C and A-Type sesquioxide phases. A vertical doted line indicates the phase transition pressure to the A-type phase. The solid curve is a calculated fit to the observed data using the Vinet EOS. Again it is apparent that the Vinet EOS fails to provide and accurate fit for the P-V data in the A-type phase. The data for this plot are listed in the Appendix.
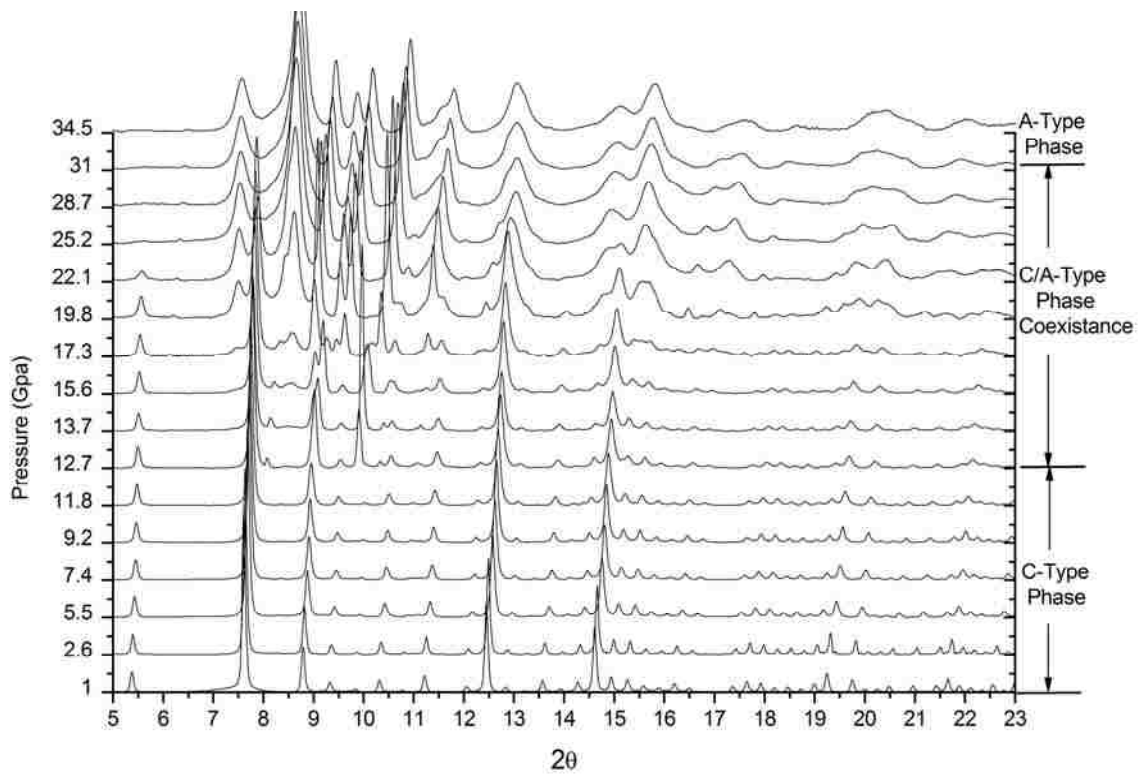
Figure 4.29 Diffraction patterns of $Y_2O_3$ Experimental Run #1.
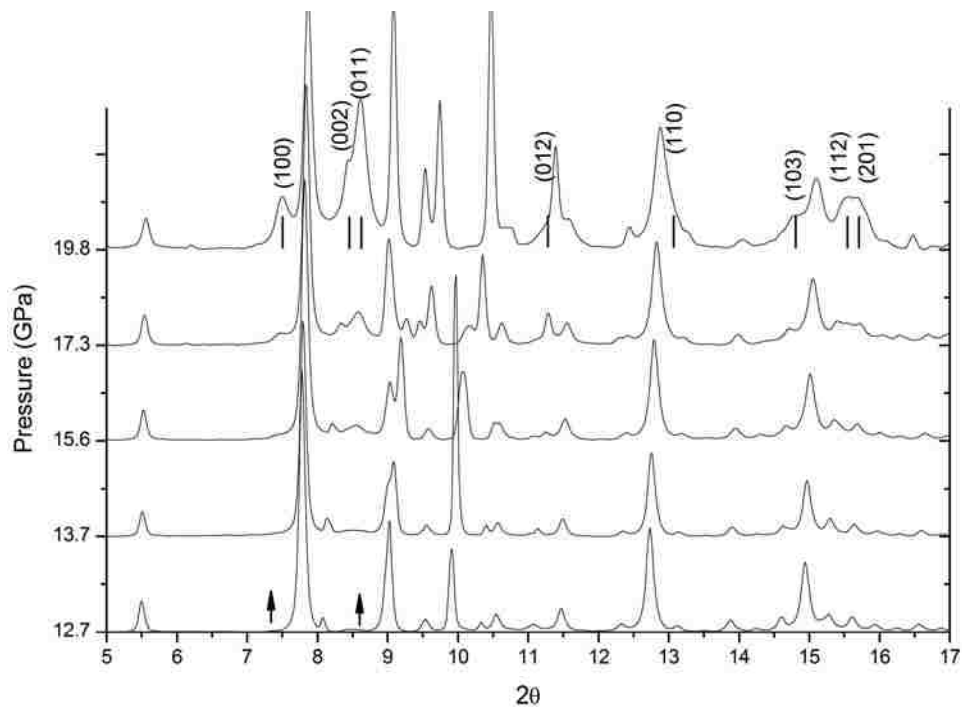


Figure 4.30 Enlargement of diffraction patterns of $Y_2O_3$ Experimental Run #1 from 12.7 to 19.8 GPa.
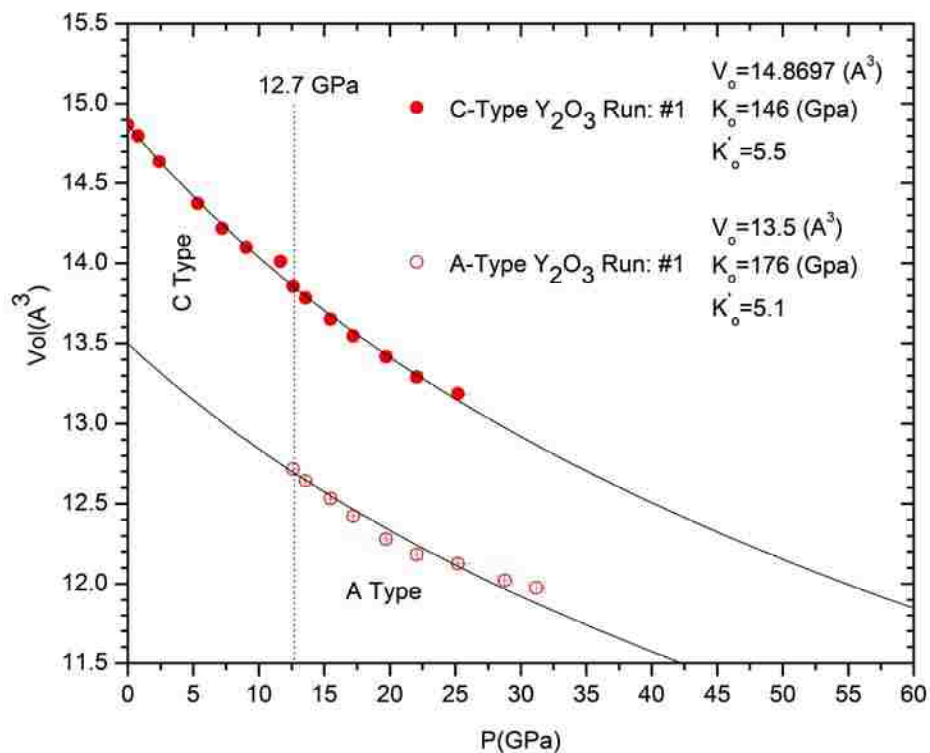
Figure 4.31 Volume versus pressure equation of state for $Y_2O_3$

## 4.2 Summary of X-Ray Diffraction Data

In this section, I summarize the findings of the systematic X-ray diffraction study on

the rare-Earth sesquioxides. There are two major points to discuss from the results

presented in Chapter 4.1. First, a discussion of the A-type phase regarding anomalies in

diffraction peak profiles and P-V EOS data. Secondly, I present a summary of all the

compression data showing the systematic high pressure behavior seen in the rare-Earth

sesquioxides.

In experiments where complete transformation from C to A-type phase is observed

(Sm, Gd, Eu, and Y sesquioxide) the structural transition is accompanied by significant

diffraction peak profile broadening. X-ray diffraction peak profiles will broaden if the

108

applied stress contains a significant deviatoric component. In high pressure DAC

experiments, this may occur when the pressure medium freezes or if the sample chamber

thins out to the point where the sample is bridging the diamond anvils. This causes

anisotropic deformation of the sample and, in particular, measurement of any lattice plane

d-spacing will contain a distribution of values resulting in the observation of strain

broadened peak profiles. Additionally, unit cell volumes measured under non-hydrostatic

conditions result in significantly larger volumes than corresponding values obtained

under hydrostatic compression.

Singh[66] has constructed a thorough theoretical description of the effects observed in x-

ray diffraction experiments on samples under non-hydrostatic stress. Because volume

strain is underestimated in non-hydrostatic conditions, a high pressure diffraction

experiment conduced through the freezing point of the pressure transmitting medium (or

where the bulk modulus of the pressure medium is rapidly increasing) may appear in P-V

space as a phase transition has occurred in the sample being studied. A good description

how non-hydrostatic stress can lead to misinterpretation of high pressure x-ray diffraction

data is seen in a recent article by Bob Downs.[67]

In $Gd_2O_3$ Experimental Run #3, helium is used as the pressure medium which has a

freezing point of 11.8 GPa at 300K and is quais-hydrostatic up to a pressure of 50 GPa.

The C to A-type phase transition in $Gd_2O_3$ is seen to occur at approximately 7 GPa and is

where the helium pressure medium is still a fluid. The diffraction data collected in $Gd_2O_3$

Experimental Run #3 still shows a substantial amount of peak profile broadening. This

indicates that the profile broadening is not occurring as a result of deviatoric stress; rather

it may come from unresolved diffraction peak multiplets present due to a structural distortion of the A-type hexagonal cell.

The misfit in P-V EOS curves to all A-type sesquioxides studied here provides additional support that the choice of high pressure crystallographic unit cell is incorrect for pressures significantly beyond the transition pressure. In the case of $La_2O_3$, where the A-type phase is purportedly the ambient pressure phase, compression data show the same misfit in EOS and diffraction peak profile broadening. This prompted a detailed investigation of $La_2O_3$ as discussed in the following chapter.

Tables 4.3 and 4.4 summarize the EoS data colleted in Chapter 4.1. Displayed are the reference volumes $V_0$ measured at ambient pressure for the C-type RES compounds and volumes extrapolated to 1 bar for the A-type RES, except for $La_2O_3$. Values for the bulk modulus ($K_o$) and the pressure derivative of the bulk modulus ($K'_o$) are listed along side calculated uncertainties in each parameter ($\sigma K_o$, $\sigma K'_o$).

Table 4.3 C-Type EoS parameters fit using Vinet equation of state.

| Equation of State Parameters for the C-Type Phase | | | | | | |
|---|---|---|---|---|---|---|
| Sample | $V_o$ | $K_o$ | $\sigma K_o$ | $K'_o$ | $\sigma K'_o$ | Red. $\chi^2$ |
| $Sm_2O_3$ | 16.3367 | 116 | 1 | 4 | fixed | 4.57 |
| $Eu_2O_3$ | 16.0059 | 115 | 1 | 5.9 | 0.4 | 1.07 |
| $Gd_2O_3$ | 15.8030 | 125 | 1 | 4.7 | 0.1 | 1.26 |
| $Y_2O_3$ | 14.8697 | 146 | 1 | 5.5 | 0.1 | 0.67 |
| $Er_2O_3$ | 14.6530 | 136 | 1 | 5.9 | 0.1 | 0.67 |
| $Lu_2O_3$ | 14.0255 | 144 | 1 | 6.7 | 0.1 | 1.31 |

Equation of state parameters shown in table 4.4 for the A-type RES compounds assume a hexagonal metric for the calculation of unit cell volumes through out the pressure range studied.

Table 4.4 A-Type EoS parameters fit using Vinet equation of state.

| Equation of State Parameters for the A-Type Phase | | | | | |
|---|---|---|---|---|---|
| Sample | $V_o$ | $K_o$ | $\sigma K_o$ | $K'_o$ | $\sigma K'_o$ | Red. $\chi^2$ |
| $La_2O_3$ | 16.4481 | 113 | 1 | 6.0 | 0.1 | 1.42 |
| $Sm_2O_3$ | 14.6 | 130 | 1 | 6.9 | 0.1 | 0.67 |
| $Eu_2O_3$ | 14.4 | 134 | 1 | 4.1 | 0.1 | 0.72 |
| $Gd_2O_3$ | 14.3 | 145 | 1 | 4.2 | 0.1 | 0.73 |
| $Y_2O_3$ | 13.5 | 176 | 1 | 5.1 | 0.1 | 1.10 |
| $Er_2O_3$ | x | x | x | x | x | x |
| $Lu_2O_3$ | x | x | x | x | x | x |

Isothermal compression data presented in tables 4.3 and 4.4 shows the clear trend of increasing bulk modulus with increasing lanthanide atomic number. This is a reflection of the ionic radii contracting with increasing atomic number causing an increase bulk density and therefore an increase in bulk modulus is observed.

Lastly, it is observed that the pressure required to initiate the C to A-type structural phase transition is linear in 4-f electron occupation number for the rare-Earth sesquioxides. This trend is shown clearly in figure 4.32 where the solid shaded bars represent the ambient pressure C-type phase and diagonal hashed bars the A-type phase. Literature values indicated in figure 4.32 are equivalent to those presented in figures 1.7, 1.8, and 1.9. The question mark above the Yb column is to indicate that in $Yb_2O_3$ Experimental Run #1 a positive identification of the A or B-type phase was not possible. The hashed bars extend upward to the highest pressure measurement made for each respective compounded. It has been assumed here that the high pressure phase observed is actually described by the A-type cell.

The scatter of literature data about the C to A-type transition line is of particular

interest. As figure 4.32 shows, several authors have observed the C-type phase transition

to the B-type and subsequently the A-type as pressure is increased. This was not the case

in the present investigation. All previously reported work on the RES compounds at high

pressure were performed using pressure transmitting media that are substantially stiffer

(see figures 1.7-1.9) than the condensed gas media used here. This may indicate that the

phase transition pathway observed is dependant on the amount of deviatoric stress acting

on the crystal.
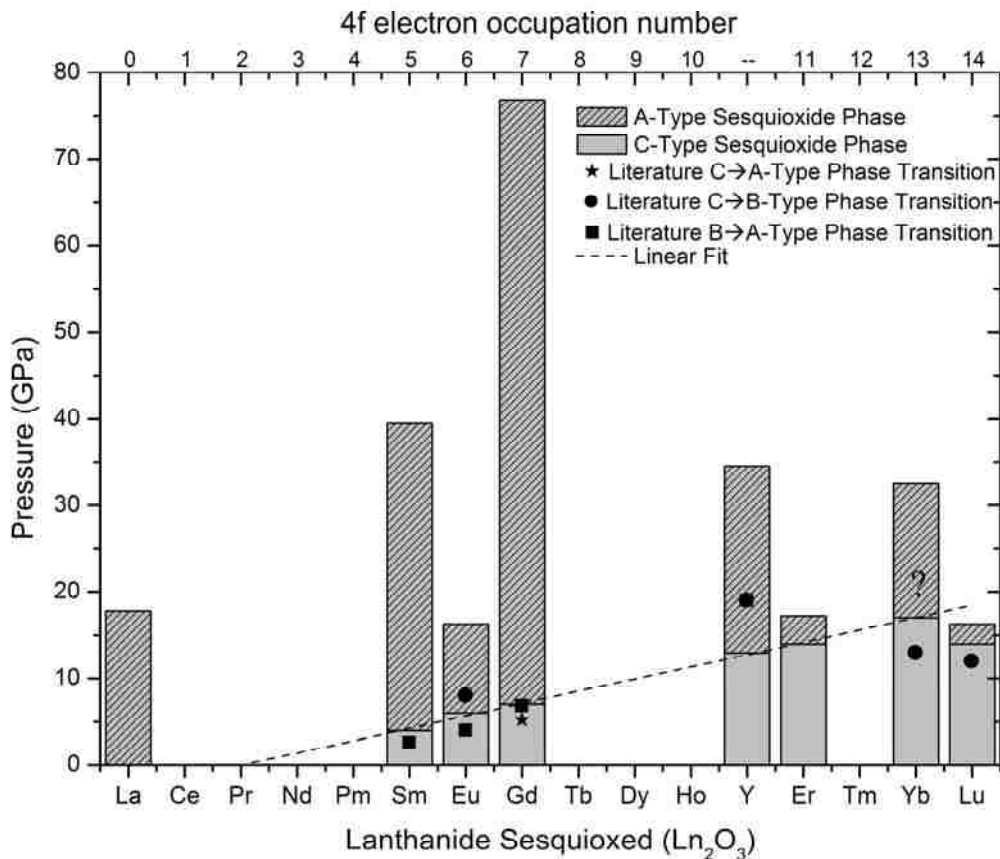


Figure 4.32 Phase stability field of the rare-Earth sesquioxides. Compilation of all
diffraction data collected in the present study.

CHAPTER 5

DETAILED ANALYSIS OF LA$_2$O$_3$

In this chapter, I show evidence that a long established sequence of high pressure

phase transformations in rare earth sesquioxides involve more than the five currently

known phases.  Here, I report results of a high-pressure study of La$_2$O$_3$ using Raman

scattering, IR absorption, and angle-dispersive x-ray diffraction (XRD) techniques.  In

XRD patterns acquired by imaging detectors at pressures above 7.5 GPa, new reflections

appear at low 2θ angle, implying that a super lattice forms.  High resolution XRD scans

reveal peak splitting consistent with a monoclinic distortion of the A-type structure.  A

model of the distorted A-type structure is derived using group-subgroup relations to

predict peak splitting and unit cells refined based on the observed XRD patterns.  Super

lattice formation is further supported by Raman spectra acquired for separate samples

which show a doubling of the A$_{1g}$ stretching mode of the A-type phase above 4 GPa.  IR

absorption and Raman scattering data are used together in a normal coordinate analysis

where calculated mode frequencies model the observed spectra up to 18 GPa with

reasonable refined values for all force constants.  Until this study, there have been no

reported pressure induced structural phase transitions outside the 5 known rare earth

sesquioxide polymorphs.

## 5.1  Experimental Details

A-type La$_2$O$_3$ was obtained commercially from Sigma-Aldrich and had a stated purity

of 99.999%.  Before each experiment, several mg of La$_2$O$_3$ were sintered at 1200 $^{\circ}$C for 8

hrs to drive off water, carbonates, and other impurities.  The sample was then annealed at

700 °C for 24 hrs and placed in a desiccator prior to loading to limit re-adsorption of water.

High pressure experiments were done in a symmetric type diamond anvil cell (DAC), see figure 2.1, with culets of 300 μm and rhenium gaskets. Each gasket was indented to a thickness of 50 μm, and a 100-μm diameter hole was drilled in the center of the indentation to form the sample chamber. An amount of $La_2O_3$ filling approximately one-third of the chamber was placed into the gasketed DAC. Several ruby spheres were added as pressure markers, and the pressure medium introduced into the sample chamber. Shifts of the $R_1$ fluorescence line from the value measured at ambient pressure were converted to pressure using the Mao-Bell pressure scale[44] with parameters A and B equaling 1904 and 9.5, respectively.[45]

Angular dispersive XRD patterns were collected at Sector 16 (HPCAT) of the Advanced Photon Source and at Sector 5A of the Pohang Accelerator Lab (PAL). At HPCAT, we used monochromatic light of wavelength 0.41356 angstroms focused to approximately a 25-μm diameter spot in the center of the DAC. Argon was the pressure transmitting medium. A MAR345 image plate detector was used to acquire 2D images of the diffracted light, and we integrated the patterns with the Fit2D[51] software package. The DAC was scanned in the plane perpendicular to incident beam to ensure that enough grains were illumined to provide adequate power diffraction statistics and improved intensities.[49]

For powder diffraction data collected at PAL, we used an X-ray beam of 0.63101 angstroms focused at the center of a six circle Huber goniometer by a sagittally bent monochromator crystal. 4:1 methanol:ethanol was the pressure transmitting medium.

Instrumental profile parameters and zero-offsets were extracted by Le Bail refinement of the powder pattern from a $LaB_6$ diffraction calibrant acquired from NIST. The DAC was centered on the goniometer and a point detector scanned in $2\theta$ at $0.01^\circ$ increments. A scanning diffractometer, such as this, gives significantly higher $2\theta$ resolution over image plate acquired data. This facilitates the identification of minor pressure induced structural changes in polycrystalline samples that may otherwise go unnoticed when lower resolution techniques are used.

All Raman measurements were excited with the 488-nm line of an Ar-Ion laser with approximately 20mW of power focused to a spot 20 μm in diameter in the sample chamber. Argon was the pressure transmitting medium. Raman scattered light was collected with a long working distance Mitutoyo objective and dispersed with a SPEX 1704 1-m focal length f/8 Czerny-Turner scanning monochromator equipped with a ruled 1200 groove/mm diffraction grating blazed at 500 nm. The widths of the entrance and exit slits were always equal at 50-100 μm so that the instrumental spectral band pass was 0.04-0.08 nm or 1.7-3.5 $cm^{-1}$ for 488 nm. A Peltier cooled Hamamatsu R928 photomultiplier tube (PMT) was used as a single point detection device with a dark count less than 1 $s^{-1}$. A detailed description of the Raman spectrometer used for these experiments is presented in Chapter 2.3.2.

Infrared (IR) absorption spectra were collected at the U2A beamline at the National Synchrotron Light Source (NSLS), Brookhaven National Laboratory. For these experiments, a symmetric DAC was equipped used with Type IIa IR quality diamonds having 300-μm culet diameters. CsI was used as the pressure transmitting medium together with annealed ruby spheres for pressure markers. The $La_2O_3$ sample and CsI

were mixed together, and the mixture was packed into a 50-μm diameter hole drilled in a 100-μm thick indented rhenium gasket.

## 5.2  Results and Discussion

X-Ray diffraction patterns of $La_2O_3$ collected at HPCAT are displayed in figure 5.1. Pressure was increased incrementally up to 18 GPa under quasi-hydrostatic conditions. Diffraction peaks originating from the Ar pressure medium and trace amounts of $La(OH)_3$ are labeled by asterisks and x's respectively.  Unit cell parameters are refined based on the A-type structure using the GSAS[52] program.

Figure 5.2 shows the results of a typical Reitveld refinement using GSAS at a pressure of 7.5 GPa.  Values for the profile-weighted residuals were typically on the order of 10%. Close inspection of the data presented in the inset of figure 5.2a show reflections that are positively indexed to the (002) and (003) planes of a super lattice formed by a geometric doubling along the c axis of the A-type unit cell.  These reflections, including several additional weak peaks, increase in intensity with increasing pressure.  The most intense of these, being the (002) reflection, is shown in figure 5.2b as a function of pressure.  At 18 GPa the (002) peak is clearly above the noise floor, however, still a mere 3% relative to the most intense peak (011) A-type or (012) in the A-type super lattice setting.

Table 5.1 lists relevant structure parameters for the A-type super lattice unit cell for selected pressures up to 18 GPa.  Bond lengths $r_1$ and $r_6$ correspond to the <La1-O3> and <La2-O2> (see Figure 5.9a) bonds respectively and are the only bonds aligned with the c-axis of the unit cell.  From the high anisotropic compressibility seen via large deviation in relative lengths of the unit cell axes, it is expected that bond lengths $r_1$ and $r_6$ should be

116

the most pressure dependent.  At 1 bar, $r_1$ is equal to $r_6$ in the A-type RES structure and no distinction is made between them.  However, strong uneven pressure dependence results in the two bonds deviating in length by 14% at a pressure of 18 GPa.  Vibrational species whose symmetry adapted coordinates transform as linear combinations of z (where the c axis is aligned to the z Cartesian axis) are of the $A_{1g}$ type and should be most affected by this anisotropic compression.

In addition to super lattice reflections observed in the XRD patterns, diffraction peak profiles broaden as pressure increases.  Given the nature of the argon pressure transmitting medium used for this experiment and previous experiments conducted where helium was the pressure medium, we do not expected to see such behavior in the diffraction patterns.  This peak broadening was observed in all compression studies involving RES where the C to A-Type structural transition is observed.  According to Atou,[32] this behavior, as seen in $Gd_2O_3$ and $Sm_2O_3$, is considered to be the result of strain or dislocations formed during this "reconstructive" phase transition.   A recent compression study on $Gd_2O_3$ by Zhang[68] et. al. attributes this to the small grain size of the diffracting crystallites.  The assumption here may be that at pressures above a few GPa the structural coherence needed for sharp diffraction peaks to be observed is not sufficiently satisfied.

In these experiments the starting phase is the A-type, and similar diffraction peak profile broadening is observed.  This is not due to poor crystallinity of the sample.  Raman spectra of the same batch of $La_2O_3$, under identical conditions, show relatively sharp and resolved peaks.  The extent of structural coherence required for the Raman effect is on the order of the excitation wavelength which is orders of magnitude greater in

length than the scale of structural coherence needed for polycrystals to exhibit sharp x-ray diffraction profiles.  Raman spectra of polycrystallites that lack structural coherence at the angstrom level would be weak, having broad peaks profiles, and this is not the case here.
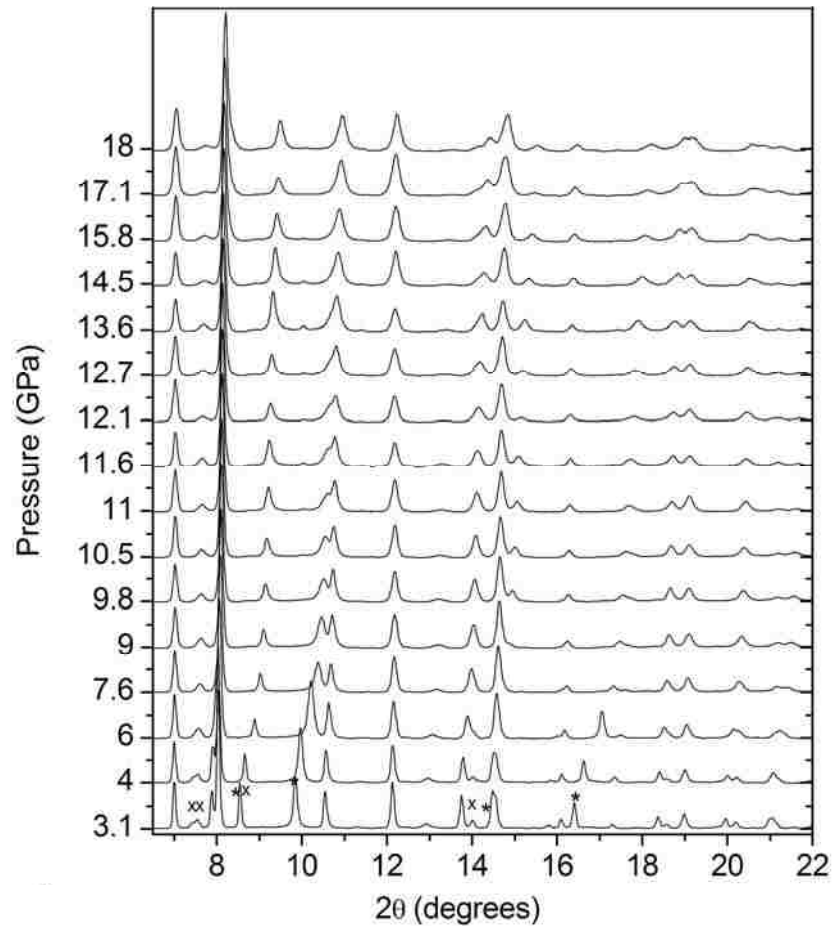


Figure 5.1 Diffraction patterns of $La_2O_3$ as a function of pressure. X's represent peaks indicating the presence of a small percentage $La(OH)_3$.  Asterisks (*) are marking peaks belonging to the Ar pressure medium.

Table 5.1 Lattice parameters (Å), bond lengths (Å), and fractional atomic coordinates  (z only) and respective Wyckoff site are listed as a function of pressure (GPa) for the A-Type super lattice.  Values r1 and r6 are bond lengths corresponding to <La1-O3> and <La2-O2> bonds respectively.

| P (GPa) | A | C | r1 | r6 | La1 - 2d | La2 - 2d | O1 - 2d | O2 - 2d | O3 - 1a | O4 - 1b |
|---|---|---|---|---|---|---|---|---|---|---|
| 0.0001 | 3.9360 | 12.3321 | 2.457 | 2.457 | 0.6235 | 0.1235 | 0.8227 | 0.3227 | 0 | 1/2 |
| 3.1 | 3.9109 | 12.0276 | 2.344 | 2.401 | 0.6231 | 0.1278 | 0.8227 | 0.3227 | 0 | 1/2 |
| 7.6 | 3.9017 | 11.8221 | 2.229 | 2.365 | 0.6225 | 0.1345 | 0.8227 | 0.3227 | 0 | 1/2 |
| 18 | 3.8680 | 11.3191 | 1.961 | 2.283 | 0.6212 | 0.1496 | 0.8227 | 0.3227 | 0 | 1/2 |
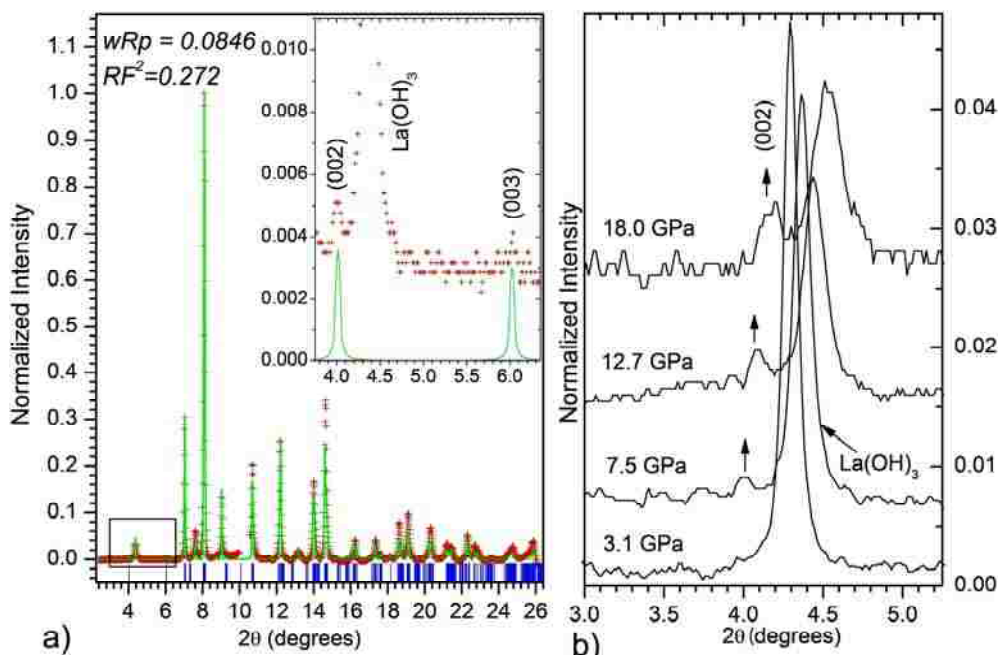
Figure 5.2. (a) Diffraction pattern of $La_2O_3$ at 7.5 GPa. Red pluses indicate the measured pattern and the solid green line represents the calculated super lattice diffraction pattern. The inset corresponds to the inscribed box at the bottom left. (b) Enlarged region of the diffraction patterns from $La_2O_3$ at various pressures. Upward arrows indicate a super lattice reflection indexed to the (002) plane. A peak from $La(OH)_3$ is present in the data and labeled.

We therefore consider the observed diffraction profile broadening to be the result of unresolved peak multiplets arising from slight monoclinic distortion of the A-Type super lattice unit cell. We use group-subgroup relationships to model the peak broadening seen in high resolution XRD scans collected at the PAL. Figure 5.3a and 5.3b compare refined diffraction patterns of the novel monoclinic distorted A-type structure to the traditional A-type cell at 7.5 GPa. We find the monoclinic structure model to better match the observed intensities ($RF^2$) and the profile weighted residual (wRp). Statistically, it is more often the case that a lowering of symmetry in the structure model results in worse $RF^2$ values; therefore, we believe this to be convincing evidence that the correct structure model is the distorted monoclinic phase.

120
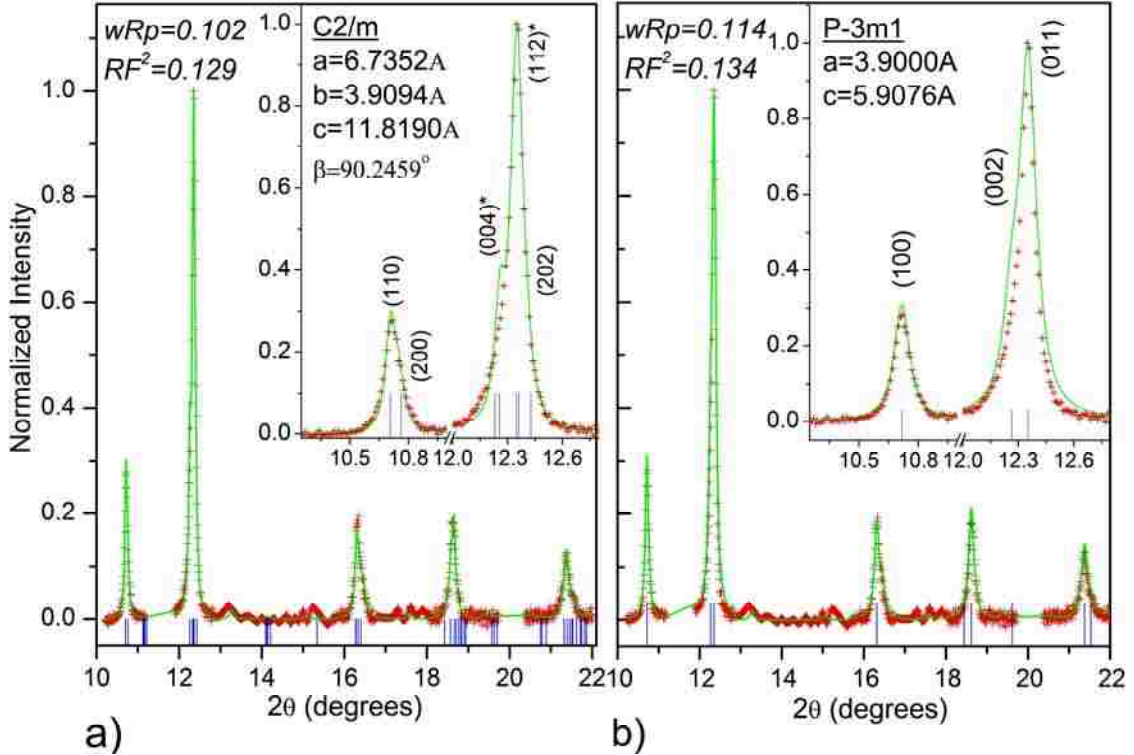
Figure 5.3. Powder diffraction data of $La_2O_3$ at 7.5 GPa collected at the PAL; (a) Red pluses indicate the calculated monoclinic distorted A-Type sesquioxide structure's diffraction pattern. The inset in the upper right of plot is an enlarged region of the lower $2\theta$ range. Drop lines indicate calculated peak positions. Asterisks above the Miller indices indicate two closely spaced peaks, the most intense listed. (b) Red pluses indicate the calculated A-Type sesquioxide structure's diffraction pattern. The inset in the upper right of plot is an enlarged region of the lower $2\theta$ range.

Following the theoretical framework developed in Chapter 3.2, a Simple Valance Force (SVF)[64] field model is constructed using the A-type $La_2O_3$ lattice parameters[19] at 1 bar in order to provide the necessary foundation from which subsequent high pressure models of $La_2O_3$ are derived. A total of five force constants are defined within the SVF model ($f_1$-$f_5$) which represents the bond stretching terms for La-O bonds ($f_1$-$f_3$) and O-O repulsion terms ($f_4$-$f_5$), see figure 5.9a. All force constants are varied in a least squares fashion until the best agreement between calculated and observed frequencies is achieved.

The correct choice of mode assignment is critical to achieving a successful refinement. Several models are tested wherein the mode assignments are varied based on previously reported results.[69-72] Boldish[70], Zarembowitch[71], and Gouteron[72] report mode assignments that exclude a low frequency band occurring around 70 cm$^{-1}$ for both $La_2O_3$ and $Nd_2O_3$. These authors assign a band at approximately 190 cm$^{-1}$, listed as $\omega_1$ in figure 3a, to the low frequency $A_{1g}$ mode in place of the band at 70 cm$^{-1}$. The band observed at 104 cm$^{-1}$ is attributed to the low frequency $E_g$ mode. When these mode assignments are used in the same SVF model, a poor agreement between observed and calculated frequencies results for both $La_2O_3$ and $Nd_2O_3$, see table 5.3. Denning and Ross[69] assign the band observed at 70 cm$^{-1}$ to the low frequency $E_g$ mode and attribute the band at 190 cm$^{-1}$ as the overtone of the low frequency $A_{1g}$ mode which is assigned to the band at 104 cm$^{-1}$. When this mode assignment is used, a significantly better agreement is seen for both the Raman and IR active modes. Moreover, the calculated vibrational frequencies for optically active modes in $Nd_2O_3$ are well represented with this assignment. It is from this agreement that the mode assignments of Denning and Ross are used in the high pressure calculations.

Force constants are listed in table 5.2 for calculations based on the various referenced mode assignments tested. Force constants for both $La_2O_3$ and $Nd_2O_3$ in the A-type setting are shown. Table 5.3 lists calculated and observed normal mode frequencies (central portion of table) according to a particular mode assignment (left column).

Table 5.2 Force constants used in normal coordinate calculations for ambient pressure A-type $La_2O_3$ structure. Atom numbering corresponds to Figure 5.9a.

| Constant | $f_1$ (Ln1-O3) | $f_2$ (Ln1-O2) | $f_3$ (Ln1-O1) | $f_4$ (O2-O1) | $f_5$ (O2-O3) |
|---|---|---|---|---|---|
| $La^b$ | 0.98 | 0.88 | 0.19 | 0.001 | 0.14 |
| $La^c$ | 0.94 | 1.12 | 0.22 | 0.04 | 0.09 |
| $La^d$ | 1.02 | 1.05 | 0.22 | 0.02 | 0.05 |
| $Nd^b$ | 1.05 | 1.03 | 0.13 | 0.10 | 0.10 |
| $Nd^c$ | 1.08 | 1.22 | 0.22 | 0.04 | 0.14 |
| $Nd^d$ | 0.99 | 0.95 | 0.23 | 0.04 | 0.11 |

a. Low frequency mode observed on a TriVista triple spectrometer in a separate experiment.
b. Calculation by author based on SVF model as described in this paper using the mode assignment in [69].
c. Calculated vibrational frequencies from ref [69].
d. Calculation is done by the author assuming the mode assignments and initial force constants given in references [70] and [71].
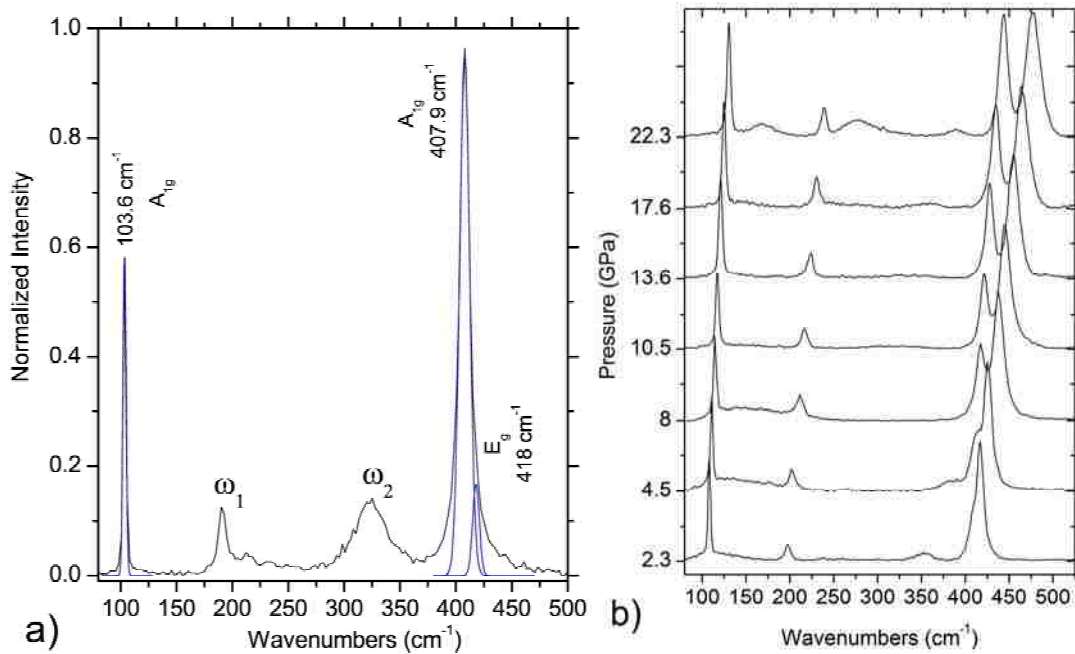


Figure 5.4 Raman spectrum of $La_2O_3$ (a) at 1 bar. The two $A_{1g}$ modes are labeled, and one of the two $E_g$ modes is seen as a shoulder to the most intense $A_{1g}$ peak. The peak labeled $\omega_1$ is assigned to the first overtone of the low frequency $A_{1g}$ mode. Peak $\omega_2$ is thought to be from an impurity phase present in the sample. Fitted peak profiles are shown below the observed data as a blue curve. (b) Selected Raman spectra of $La_2O_3$ for pressures up to 22 GPa.

Table 5.3. Observed and calculated vibrational mode frequencies, left. (R) and (IR) indicate Raman and IR activity respectively.

| | La$_2$O$_3$ | | | | | | | Nd$_2$O$_3$ | | | | | |
|---|---|---|---|---|---|---|---|---|---|---|---|---|---|
| | Obs | Calc[b] | Obs | Calc[c] | Obs | Obs | Calc[d] | Obs | Calc[c] | Calc[b] | Obs | Obs | Calc[d] |
| Mode\|\|Ref | [JM] | | [69] | | [71] | [70] | [JM] | [69] | | [JM] | [71] | [70] | [JM] |
| A$_{1g}$ (R) | 407.9 | 408 | 408 | 401 | 400 | 410 | 395 | 440 | 437 | 426 | 428 | 427 | 407 |
| A$_{1g}$ (R) | 103.6 | 107 | 108 | 113 | 191 | 195 | 111 | 108 | 118 | 108 | 191 | 190 | 108 |
| E$_g$ (R) | 418 | 411 | 444 | 449 | 408 | 410 | 428 | 480 | 477 | 440 | 436 | 436 | 421 |
| E$_g$ (R) | 70.8[a] | 69 | 74 | 67 | 106 | 107 | 60 | 74 | 73 | 62 | 106 | 107 | 68 |
| A$_{2u}$ (IR) | 376.9 | 376 | 386 | 386 | x | x | 392 | 410 | 410 | 412 | x | 405 | 385 |
| A$_{2u}$ (IR) | 184.5 | 200 | 242 | 242 | x | x | 229 | 242 | 242 | 239 | x | 228 | 240 |
| E$_u$ (IR) | 411.4 | 411 | 435 | 430 | x | x | 417 | 450 | 449 | 421 | x | 412 | 398 |
| E$_u$ (IR) | 225.4 | 211 | 242 | 244 | x | x | 233 | 242 | 245 | 220 | x | 228 | 241 |

a. Low frequency mode observed on a TriVista triple spectrometer in a separate experiment.
b. Calculation by author based on SVF model as described in this paper using the mode assignment in [69].
c. Calculated vibrational frequencies from ref [69].
d. Calculation is done by the author assuming the mode assignments and initial force constants given in references [70] and [71].

Raman spectra collected at 1 bar and for pressures up to 22.3 GPa are displayed in Figure 5.4. Figure 5.4a clearly shows the high frequency $E_g$ mode is observed as a weak shoulder to the more intense $A_{1g}$ mode at 408cm$^{-1}$. As pressure increases, a secondary shoulder to the $A_{1g}$ mode is seen to form, however, on the low frequency side. This new vibrational mode's intensity and frequency separation increase with increasing pressure as shown in Figure 5.4b. The high frequency $E_g$ mode remains in the shoulder of the $A_{1g}$ mode and at higher pressures becomes indistinguishable.
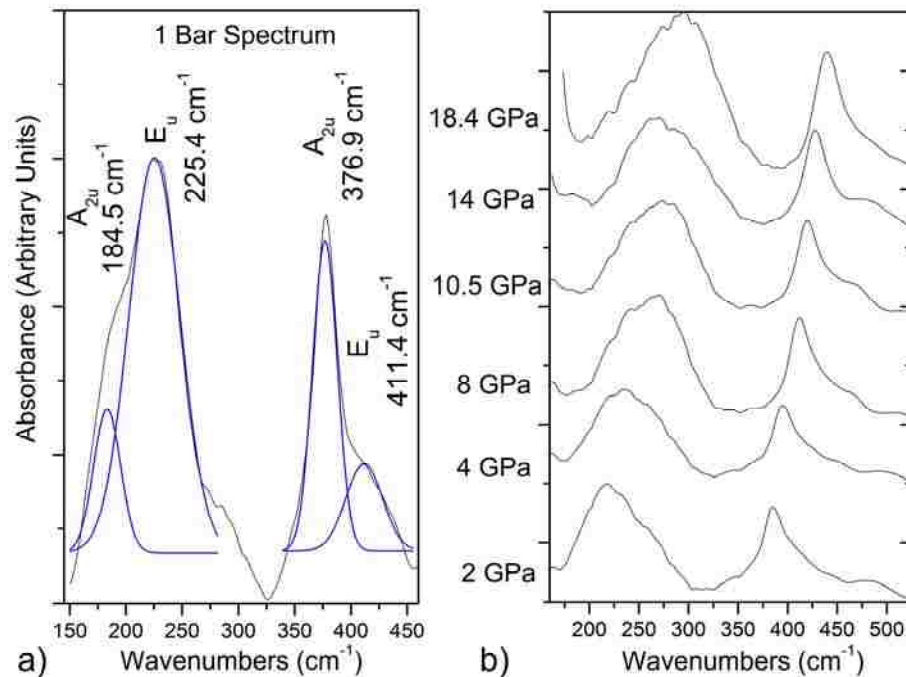


Figure 5.5. IR absorption spectra of La$_2$O$_3$. (a) Spectrum at 1 bar. Mode assignments are listed above their respective peaks. Fitted peak profiles are shown below the observed data as a blue curve. (b) IR absorption spectra collected at selected pressure points.

IR absorption spectra are shown in Figure 5.5 for a similar pressure range over which previous Raman spectra were collected. The inherently broad spectral nature to IR

absorbance measurements makes mode identification more complicated. Figure 5.5a shows the observed spectrum at ambient pressure and fitted peak profiles below the observed data. The same mode assignments are made for spectra collected at pressures above 1 bar.

Phase transformation to the A-type super lattice via geometric doubling along the c axis of the A-type unit cell, as suggested by the XRD data analysis, results in a new mode enumeration. It is determined from the correlation method that the number of Raman active modes double in the super lattice structure following the doubling of atomic sites. The number of IR active modes also doubles; however, two modes derived to have $A_{2u}$ and $E_u$ symmetry in the total representation are acoustic modes and must be subtracted leaving 10 total IR active modes.

$$\Gamma_{total} = 4A_{1g} + 6A_{2u} + 4E_g + 6E_u$$
$$\Gamma_{Acoustic} = A_{2u} + E_u$$
$$\Gamma_{vib} = 4A_{1g} + 5A_{2u} + 4E_g + 5E_u$$

High pressure vibrational spectra are simulated using an extension of the normal coordinate model developed for the ambient pressure phase. In this model, the c axis of the unit cell is doubled which increases the number of internal coordinates and bond stretching interactions by a factor of 2. Initially, the two cells are exact replicas, and the additional cell only caries redundant coordinates. Once pressure is increased, bond lengths <La1-O3> and <La2-O2> compress in a non-uniform manner. This requires different bond stretching interactions to be considered and lifts one set of redundant coordinates. In all, three additional bond stretching interactions are required to specify the changes in the high pressure super lattice unit cell. These are referred to as $r_6$, $r_7$, and $r_8$ and allow specifically for the uneven displacement of La atoms in the two sub-lattices.

Bonds $r_7$ and $r_8$ correspond to <La2-O3> and <La2-O1> respectively. Bond lengths $r_1$ and $r_6$ are of particular interest as they allow for the anisotropic change along the c axis between the two $C_{3v}$ sites; <La1-O3>:$r_6$ and <La2-O2>:$r_1$ bonds.

Force constants used in the super lattice model are obtained from the ambient pressure model and are used as initial values for the lowest pressure data point simulated in the calculation. Three additional force constants complementing the three new bond stretching interactions are required. Initial values for these force constants labeled $f_6$, $f_7$, and $f_8$ are taken from $f_1$, $f_2$, and $f_3$ respectively because at ambient pressure they are identical.

Results of calculations for the Raman active modes are shown in figure 5.6. The model predicts the observed splitting in the $A_{1g}$ mode with reasonable agreement for pressures up to 18 GPa. Three low frequency modes are predicted at frequencies less than 100 cm$^{-1}$ and fall below the detection limit of the Raman spectrometer used for this work. Two high frequency $E_g$ modes labeled $E_g1$ and $E_g2$ are predicted. The $E_g1$ mode is weakly observable in the 1 bar spectrum and is calculated to have significant overlap with the two high frequency $A_{1g}$ modes $A_{1g}1$ and $A_{1g}2$ above ambient pressure. The $E_g2$ mode is not seen in the 1 bar spectrum because its appearance is solely the result of the super lattice formation. Above 1 bar, the calculated frequency of the $E_g2$ mode becomes convoluted with the $A_{1g}2$ mode making its empirical observation difficult.
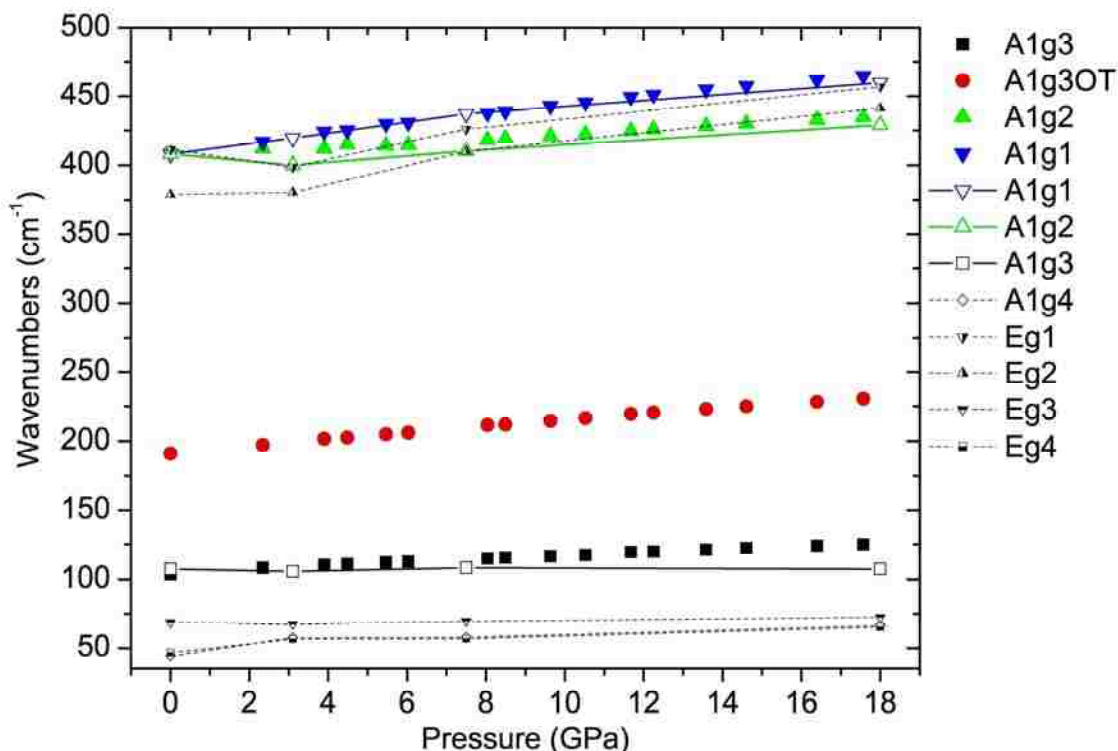
Figure 5.6. Observed (solid symbols) and calculated (hollow symbols) Raman spectra shown for pressures up to 18 GPa. Lines connecting data points are only a guide. Partially filed symbols represent calculated $E_g$ modes. The overtone to the $A_{1g}3$ mode is listed as $A_{1g}3OT$. No spectral observations were possible below 100 cm$^{-1}$.

Calculations for the IR vibrational spectra are shown in figure 5.7. Mode assignments for the high pressure spectra are consistent with the 1 bar mode assignments. The calculated vibrational modes agree reasonably with the observations. The normal coordinate model predicts the appearance of an additional $E_u$ or $A_{2u}$ mode for each mode predicted in the 1 bar model. These features are not observed as isolated peaks in the data, rather a broadening in the observed spectra is seen and attributed to the formation of these new modes.
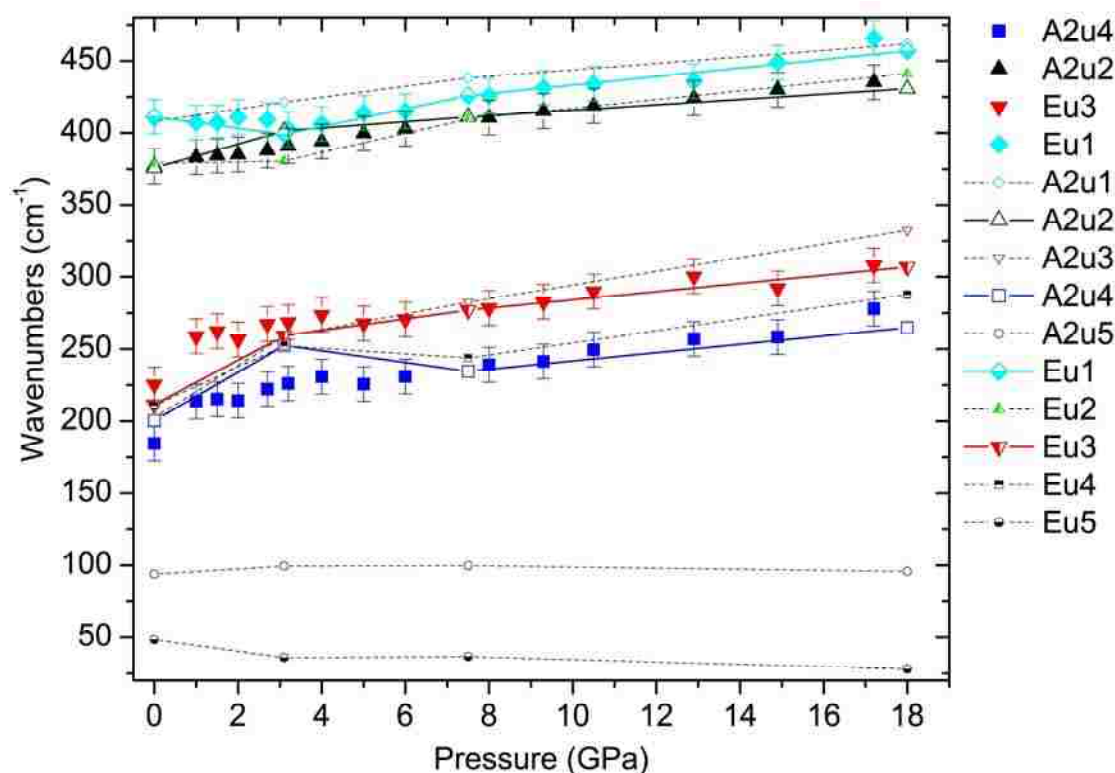
Figure 5.7  Observed (solid symbols) and calculated (hollow/partially filled symbols) IR absorption spectra shown for pressures up to 18 GPa.  Lines connecting data points are only a guide.

Pressure dependency of the force constants and bond lengths are plotted in Figure 5.8. As anticipated by the high compressibility in the c axis of the A-Type unit cell, bond lengths $r_1$ and $r_6$ show the strongest pressure dependence.  Their associated force constants $f_1$ and $f_6$ are also influenced more than other force constants in the model.

It was expected that the pressure dependency of certain $A_{1g}$ modes would be strongly affected by the super lattice formation because the symmetry adapted coordinates for the $A_{1g}$ Raman active modes are linear combinations of the z atomic Cartesian coordinates. Contrarily, the symmetry adapted coordinates for the $E_g$ modes, being linear combinations of the x and y Cartesian atomic coordinates, were expected to change only slightly with pressure.  We see this indirectly because neither $E_{g1}$ nor $E_{g2}$ dramatically

increase in intensity or frequency. In fact, they remain mostly convolved with the high frequency $A_{1g}1$ and $A_{1g}2$ modes.
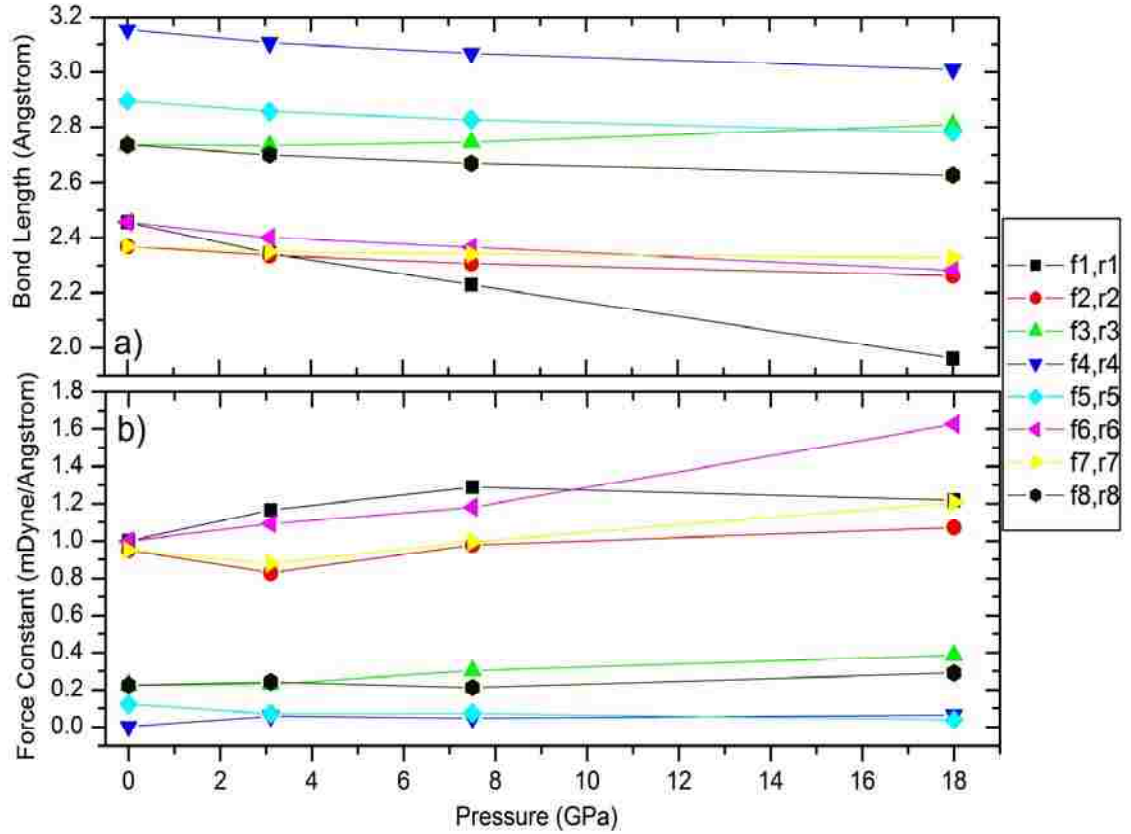


Figure 5.8 (a) Bond lengths r1 through r8 as a function of pressure. (b) Force constants f1 through f8 as a function of pressure. Plotted lines are only a guide for the eye.

The origin of this structural phase transition may be described within the framework of Landau theory of phase transitions. In particular, a subset of the manifold of continuous $2^{nd}$ order structural phase transitions falling under the Landau description are described by Toledano[73] as non-ferroic phase transitions. Non-ferroic phase transitions (NFPT) are continuous structural transitions occurring with a breaking of translational symmetry within the same crystal class and are generally identified experimentally via the appearance of super lattice reflections. In the present case, we consider the possible
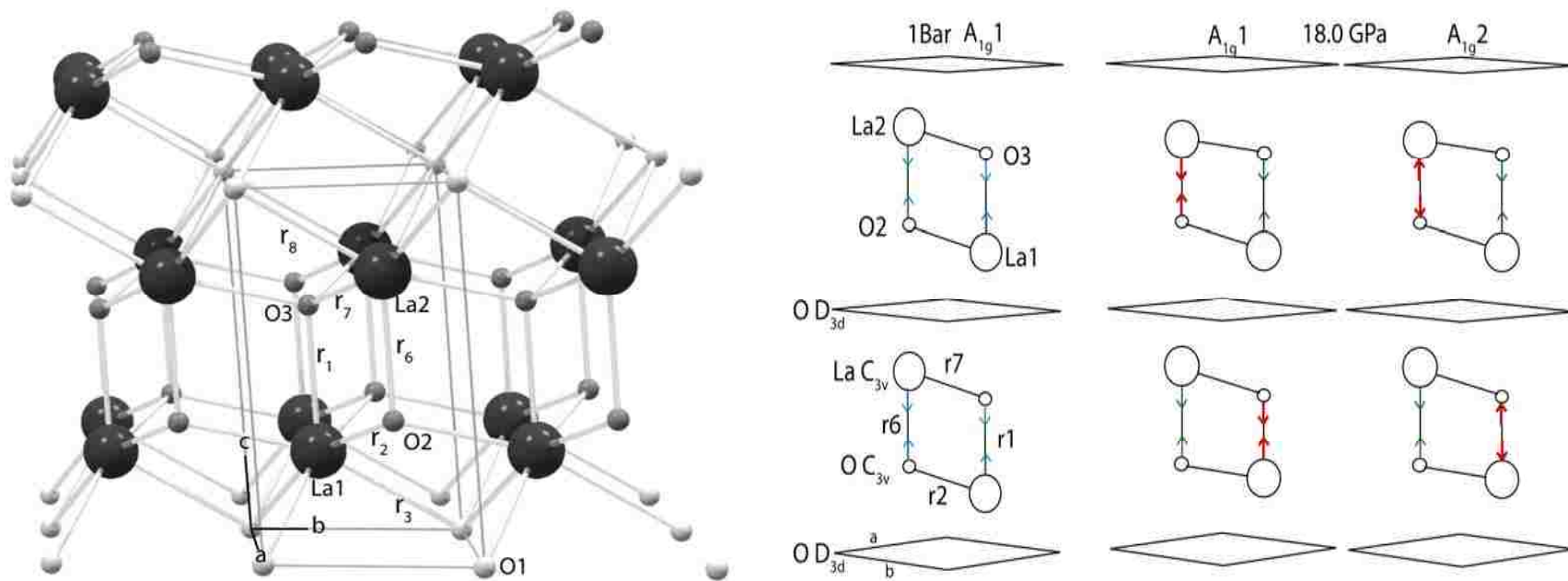
Figure 5.9 (a) The crystal structure of the A-type RES.  Edges of the primitive cell are drawn, and the atoms included in the Bravais cell are labeled.  Lanthanum atoms (dark gray), La1 and La2, are situated on one of the two $C_{3v}$ sites.  Oxygen atoms (medium gray), O2 and O3, are situated on the second $C_{3v}$ site.   Oxygen atoms (light gray), O1, occupy the only $D_{3d}$ site. Bond lengths $r_4$-$r_5$, not labeled, are the O3-O1 and O3-O2 repulsion terms.  (b) Super lattice structure shown at ambient pressure and at 18 GPa with the differences in $r_6$ and $r_1$ depicted qualitatively.

non-ferroic phase transitions in P-3m1 as restricted by the Landau and Lifschits symmetry criteria.[74] In the case where the high and low symmetry phases are identically P-3m1, the Brillouin-zone point relative to the order parameter is the zone boundary A-point having $\mathbf{k}=(0,0,1/2)\pi/c$. The irreducible representation (IR) corresponding to the order parameter (OP) adopts the IR of the small representation $\tau_n$ of the k-vector representative of $\mathbf{k}^*$. In the present case, $\mathbf{k}^*$ has only one arm $(0,0,1/2)\pi/c$ and the symmetry of the OP goes as $\tau_1$ which transforms as the totally symmetric representation of the group.[67] In the group P-3m1, the totally symmetric representation adopts $A_{1g}$ symmetry and normal coordinate analysis dictates modes having $A_{1g}$ symmetry to involve only linear combinations of the z-atomic coordinates.

It follows from Landau theory that the structure of the low symmetry phase is uniquely determined by the eigen vector of the soft phonon mode and the structure of the high symmetry phase.[75] The soft phonon eigen vector in this case is described by linear combinations of the z-atomic coordinates. In $La_2O_3$, the only atomic sites allowing movement along the z-axis, without breaking point group symmetry, are the $C_{3v}$ sites. The atomic displacements affiliated with this phase transition are therefore z-coordinates of the atoms occupying the $C_{3v}$ sites. The soft phonon mode associated with this phase transition is the zone-boundary phonon at the A-point. When this mode condenses, the imposed static distortion requires that $(0,0,1/2)*\pi/c$ become a reciprocal lattice point in the new phase. That is, a loss in translational symmetry along the z-axis that results in the formation of a super lattice. This is evidenced experimentally through the observation of super lattice reflections in the diffraction data.

A qualitative representation of the super lattice structure at ambient pressure and at 18 GPa is shown in Figure 5.9b. Planes of oxygen atoms situated on $D_{3d}$ sites are represented graphically by rhombohedral sheets that alternate with the $C_{3v}$ atomic sites. At ambient conditions, bond lengths $r_1$ and $r_6$ are equal, and the two sub-lattices identical to one another.  As pressure increases, $r_6$ is seen to compress more slowly than $r_1$ resulting two $A_{1g}$ modes different in character but similar in frequency.  The difference in bond lengths increases with pressure allowing the two $A_{1g}$ modes to become distinct in frequency.

CHAPTER 6

CONCLUDING REMARKS

A detailed investigation into the high pressure behavior of the rare-Earth sesquioxides is shown. I have demonstrated that a linear trend in the high pressure structural phase transitions from C to A-type RES compound exists which was not known prior to this investigation. The linearity in pressure needed to transform a particular RES from the C-type to A-type is thought be reflected in the linearity observed in the decrease in cation radii due to the lanthanide contraction.

Additionally, I have shown that long established trends for the RES compounds at high pressure involve more than the five currently known phases. For A-type $La_2O_3$, pressure causes La-O bonds aligned with the c-axis to compress anisotropically. This anisotropic change in bond length becomes periodic with respect to a unit cell doubled in length along the c-axis. This is thought to occur following the condensation of the A-point zone boundary phonon. This requires the A-point to become a reciprocal lattice point thus a doubling of the real space lattice should be observed. From image plate acquired XRD patterns, reflections are observed that positively index to peaks belonging to an A-type super lattice structure for pressure at and above 7.5 GPa. Raman spectra add further support to super lattice formation when the $A_{1g}$ mode, observed at 408cm$^{-1}$ (ambient pressure), "splits" into two $A_{1g}$ modes of different character above 2 GPa.

Normal coordinate calculations show good agreement to observed Raman and IR spectra for pressures up to 18 GPa. The observation of the $A_{1g}$ mode "splitting" in advance of the super lattice diffraction peak detection can be attributed to the overall

sensitivity of Raman measurements to minor changes in local symmetry. XRD measurements are not as sensitive to these effects.

Following the super lattice formation is the observation of diffraction peak multiplets by high resolution diffraction scans collected using a point detector. These data indicate a slight monoclinic distortion occurring at a pressure of 7.5 GPa. However, this distortion is within $0.2459^{o}$ from orthogonal; thus, the preceding discussion of the A-type structures in Chapter 4 has been based on a structure which contains 'psuedo-hexagonal' symmetry.

Herein, the Raman spectra have been quantitatively explained by the hexagonal A-type supercell while the origin of the weak monoclinic distortion must remain the subject of future work.

To conclude, figure 6.1 depicts a generalized phase diagram for the RES including the novel A-type phase discovered in $La_2O_3$. Common wisdom leads to the assumption that this new phase should exist at increasing pressures as one traverses the lanthanide series (from La to Lu). The investigation of the presence of the novel A-type phase in the remaining RES is the subject of future work.
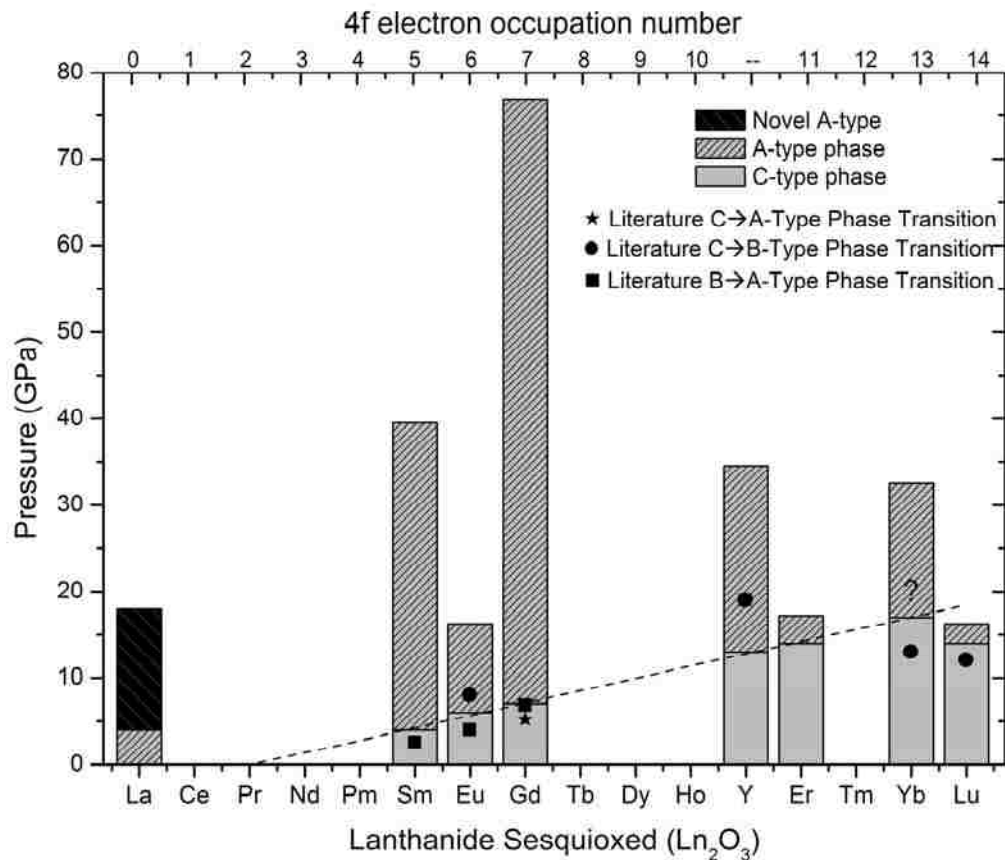
Figure 6.1  Generalized phase diagram for the RES including the novel A-type phase in La$_2$O$_3$. References for phase transition points obtained in the literature for the various RES are listed in figures 1.7 through 1.9.

APPENDIX

SUPPLEMENTARY DATA

Refer to the tables below for all compression data collected for the rare-Earth sesquioxides included in this thesis study. Tables are presented in order of increasing atomic number beginning first with the C-Type phase and secondly for the A-Type phase.

## C-Type $Sm_2O_3$

Compression Data on C-Type $Sm_2O_3$

Experimental Run: $Sm_2O_3$ #1
Source: HPCAT ID-B

| P (GPa) | c($A^3$) | Vol($A^3$)/Z |
|---------|----------|--------------|
| 0.0001 | 10.9333 | 16.3367 |
| 1.0 | 10.925 | 16.300 |
| 1.2 | 10.900 | 16.188 |
| 2.3 | 10.861 | 16.015 |
| 3.1 | 10.845 | 15.943 |
| 4.8 | 10.790 | 15.703 |
| 5.0 | 10.780 | 15.659 |

Cell volumes are reported as cubic Angstroms
per number of atoms (Z) in the primitive cell.

Compression Data on C-Type $Sm_2O_3$

Experimental Run: $Sm_2O_3$ #3
Source: HPCAT ID-B

| P (GPa) | c($A^3$) | Vol($A^3$)/Z |
|---------|----------|--------------|
| 4.3 | 10.792 | 15.71 |
| 6.8 | 10.731 | 15.45 |
| 7.9 | 10.724 | 15.42 |

Cell volumes are reported as cubic Angstroms
per number of atoms (Z) in the primitive cell.

## C-Type Eu₂O₃

Compression Data on C-Type $Eu_2O_3$

Experimental Run: $Eu_2O_3$ #1

Source: CHESS B2

| P (Gpa) | c(A$^3$) | Vol/Z |
|---|---|---|
| 0.0001 | 0.00 | 16.01 |
| 1.24 | 0.04 | 15.84 |
| 2.45 | 0.07 | 15.63 |
| 2.87 | 0.09 | 15.60 |
| 3.71 | 0.11 | 15.51 |
| 4.31 | 0.13 | 15.44 |
| 5.10 | 0.15 | 15.33 |
| 6.09 | 0.18 | 15.26 |
| 7.09 | 0.21 | 15.17 |
| 7.87 | 0.24 | 15.12 |
| 9.27 | 0.28 | 15.07 |
| 9.89 | 0.30 | 15.06 |

Cell volumes are reported as cubic Angstroms per number of atoms (Z) in the primitive cell.

## C-Type Gd₂O₃

Compression Data on C-Type $Gd_2O_3$

Experimental Run: $Gd_2O_3$ #1

Source: HPCAT ID-B

| P (GPa) | c(A$^3$) | Vol(A$^3$)/Z |
|---|---|---|
| 0.0001 | 10.8231 | 15.8477 |
| 3.99 | 10.706 | 15.34 |
| 4.34 | 10.696 | 15.29 |
| 4.88 | 10.685 | 15.25 |
| 5.24 | 10.680 | 15.23 |
| 5.96 | 10.669 | 15.18 |
| 7.4 | 10.636 | 15.04 |
| 7.94 | 10.626 | 15.00 |
| 8.84 | 10.613 | 14.94 |
| 9.21 | 10.603 | 14.90 |
| 9.75 | 10.593 | 14.86 |
| 10.48 | 10.580 | 14.80 |

Cell volumes are reported as cubic Angstroms per number of atoms (Z) in the primitive cell.

Compression Data on C-Type $Gd_2O_3$

Experimental Run: $Gd_2O_3$ #5
Source: CHESS B2

| P (GPa) | $c(A^3)$ | $Vol(A^3)/Z$ |
|---------|----------|--------------|
| 0.0001 | 10.8231 | 15.8477 |
| 4.6 | 10.712 | 15.36 |
| 5.0 | 10.687 | 15.26 |
| 5.4 | 10.676 | 15.21 |
| 5.7 | 10.672 | 15.19 |
| 6.0 | 10.671 | 15.19 |
| 6.3 | 10.663 | 15.15 |
| 6.8 | 10.659 | 15.14 |
| 7.2 | 10.641 | 15.06 |
| 7.7 | 10.632 | 15.02 |
| 8.1 | 10.620 | 14.97 |
| 8.4 | 10.616 | 14.96 |
| 8.7 | 10.611 | 14.94 |
| 9.0 | 10.602 | 14.90 |
| 9.6 | 10.588 | 14.84 |
| 10.2 | 10.577 | 14.79 |

Cell volumes are reported as cubic Angstroms
per number of atoms (Z) in the primitive cell.

**C-Type Er$_2$O$_3$**

Compression Data on C-Type Er$_2$O$_3$

Experimental Run: Er$_2$O$_3$ #1

Source: HPCAT BM-D

| P (GPa) | c(A$^3$) | Vol(A$^3$)/Z |
|---------|----------|--------------|
| 0.0001 | 10.5440 | 14.6530 |
| 1.7 | 10.498 | 14.46 |
| 3.8 | 10.443 | 14.24 |
| 6.6 | 10.394 | 14.04 |
| 7.4 | 10.377 | 13.97 |
| 8.1 | 10.364 | 13.92 |
| 8.5 | 10.363 | 13.91 |
| 8.8 | 10.343 | 13.83 |
| 9.4 | 10.337 | 13.81 |
| 10.2 | 10.327 | 13.77 |
| 11.3 | 10.308 | 13.69 |
| 12.1 | 10.289 | 13.62 |
| 13.2 | 10.274 | 13.56 |
| 14.4 | 10.258 | 13.49 |
| 15.4 | 10.243 | 13.43 |
| 17.2 | 10.233 | 13.39 |

Cell volumes are reported as cubic Angstroms
per number of atoms (Z) in the primitive cell.

## C-Type Lu$_2$O$_3$

Compression Data on C-Type Lu$_2$O$_3$

Experimental Run: Lu$_2$O$_3$ #1

Source: HPCAT ID-B

| P (GPa) | c(A$^3$) | Vol(A$^3$)/Z |
|---------|----------|--------------|
| 0.0001  | 10.3913  | 14.0255      |
| 1.8     | 10.335   | 13.80        |
| 3.3     | 10.321   | 13.74        |
| 5.1     | 10.276   | 13.56        |
| 6.6     | 10.255   | 13.48        |
| 7.9     | 10.236   | 13.41        |
| 9.0     | 10.213   | 13.32        |
| 9.9     | 10.201   | 13.27        |
| 10.9    | 10.177   | 13.18        |
| 11.8    | 10.164   | 13.12        |
| 12.7    | 10.151   | 13.08        |
| 13.8    | 10.139   | 13.03        |
| 14.6    | 10.126   | 12.98        |
| 15.4    | 10.118   | 12.95        |
| 16.3    | 10.099   | 12.87        |

Cell volumes are reported as cubic Angstroms
per number of atoms (Z) in the primitive cell.

**C-Type Y$_2$O$_3$**

Compression Data on C-Type Y$_2$O$_3$

Experimental Run: Y$_2$O$_3$ #1

Source: HPCAT ID-B

| P (GPa) | c(A$^3$) | Vol(A$^3$)/Z |
|---------|----------|--------------|
| 0.0001 | 10.5957 | 14.8697 |
| 0.8 | 10.579 | 14.80 |
| 2.4 | 10.540 | 14.64 |
| 5.3 | 10.477 | 14.37 |
| 7.2 | 10.438 | 14.22 |
| 9.1 | 10.409 | 14.10 |
| 11.7 | 10.388 | 14.01 |
| 12.6 | 10.349 | 13.86 |
| 13.6 | 10.331 | 13.78 |
| 15.5 | 10.298 | 13.65 |
| 17.2 | 10.272 | 13.55 |
| 19.7 | 10.239 | 13.42 |
| 22.1 | 10.207 | 13.29 |
| 25.2 | 10.179 | 13.18 |

Cell volumes are reported as cubic Angstroms
per number of atoms (Z) in the primitive cell.

## A-Type La$_2$O$_3$

Compression Data on A-Type La$_2$O$_3$
Experimental Run: La$_2$O$_3$ #1
Source: HPCAT ID-B

| P (GPa) | a(A$^3$) | c(A$^3$) | Vol(A$^3$)/Z |
|---------|----------|----------|--------------|
| 0.0001  | 3.9340   | 6.1360   | 16.4481      |
| 3.1     | 3.911    | 6.014    | 15.93        |
| 4.0     | 3.908    | 5.991    | 15.85        |
| 6.0     | 3.901    | 5.933    | 15.64        |
| 7.6     | 3.896    | 5.889    | 15.48        |
| 9.0     | 3.891    | 5.875    | 15.40        |
| 9.8     | 3.885    | 5.862    | 15.32        |
| 10.5    | 3.884    | 5.860    | 15.31        |
| 11.0    | 3.878    | 5.849    | 15.23        |
| 11.6    | 3.878    | 5.850    | 15.24        |
| 12.1    | 3.871    | 5.841    | 15.16        |
| 12.7    | 3.869    | 5.837    | 15.13        |
| 13.6    | 3.8(85)  | 5.766    | 15.07        |
| 14.5    | 3.8(79)  | 5.736    | 14.95        |
| 15.8    | 3.8(76)  | 5.712    | 14.86        |
| 17.1    | 3.8(75)  | 5.678    | 14.77        |
| 18.0    | 3.8(68)  | 5.660    | 14.67        |

Cell volumes are reported as cubic Angstroms
per number of atoms (Z) in the primitive cell.

## A-Type Sm$_2$O$_3$

Compression Data on A-Type Sm$_2$O$_3$
Experimental Run: Sm$_2$O$_3$ #1
Source: HPCAT ID-B

| P (GPa) | a(A$^3$) | c(A$^3$) | Vol(A$^3$)/Z |
|---------|----------|----------|--------------|
| 8.1     | 3.825    | 5.564    | 14.098       |
| 9.1     | 3.750    | 5.477    | 13.340       |
| 10.2    | 3.715    | 5.549    | 13.263       |
| 12.4    | 3.713    | 5.422    | 12.944       |
| 14.7    | 3.726    | 5.549    | 13.346       |

Cell volumes are reported as cubic Angstroms
per number of atoms (Z) in the primitive cell.

Compression Data on A-Type $Sm_2O_3$

Experimental Run: $Sm_2O_3$ #3
Source: HPCAT ID-B

| P (GPa) | a($A^3$) | c($A^3$) | Vol($A^3$)/Z |
|---------|----------|----------|--------------|
| 17.8 | 3.724 | 5.489 | 13.18 |
| 19.3 | 3.720 | 5.469 | 13.11 |
| 21.0 | 3.710 | 5.453 | 13.00 |
| 23.3 | 3.690 | 5.452 | 12.86 |
| 24.4 | 3.687 | 5.441 | 12.81 |
| 25.9 | 3.678 | 5.433 | 12.73 |
| 27.0 | 3.676 | 5.427 | 12.70 |
| 29.2 | 3.669 | 5.425 | 12.65 |
| 30.7 | 3.659 | 5.4(31) | 12.60 |
| 32.5 | 3.658 | 5.416 | 12.55 |
| 34.4 | 3.664 | 5.392 | 12.54 |
| 39.5 | 3.656 | 5.346 | 12.38 |

Cell volumes are reported as cubic Angstroms
per number of atoms (Z) in the primitive cell.

Compression Data on A-Type $Sm_2O_3$

Experimental Run: $Sm_2O_3$ #3
Source: HPCAT ID-B

| P (GPa) | a($A^3$) | c($A^3$) | Vol($A^3$)/Z |
|---------|----------|----------|--------------|
| 7.9 | 3.743 | 5.696 | 13.822 |

Cell volumes are reported as cubic Angstroms
per number of atoms (Z) in the primitive cell.

## A-Type Gd$_2$O$_3$

Compression Data on A-Type Gd$_2$O$_3$

Experimental Run: Gd$_2$O$_3$ #4

Source: HPCAT ID-B

| P (GPa) | a(A$^3$) | c(A$^3$) | Vol(A$^3$)/Z |
|---------|----------|----------|--------------|
| 12.4 | 3.67 | 5.681 | 13.25 |
| 13.4 | 3.67 | 5.656 | 13.20 |
| 14.3 | 3.66 | 5.612 | 13.05 |
| 15.7 | 3.66 | 5.605 | 13.01 |
| 17.1 | 3.66 | 5.601 | 13.01 |
| 18.4 | 3.65 | 5.573 | 12.84 |
| 19.4 | 3.65 | 5.5(87) | 12.(92) |
| 20.7 | 3.65 | 5.5(66) | 12.(82) |
| 22.0 | 3.67 | 5.436 | 12.70 |
| 25.3 | 3.66 | 5.417 | 12.57 |
| 27.2 | 3.66 | 5.410 | 12.53 |
| 27.8 | 3.65 | 5.405 | 12.47 |
| 30.0 | 3.65 | 5.364 | 12.34 |
| 32.2 | 3.64 | 5.354 | 12.26 |
| 34.8 | 3.63 | 5.328 | 12.14 |
| 37.1 | 3.61 | 5.3(35) | 12.(07) |
| 39.8 | 3.59 | 5.277 | 11.80 |
| 42.6 | 3.59 | 5.273 | 11.75 |
| 45.4 | 3.58 | 5.275 | 11.73 |
| 48.2 | 3.56 | 5.249 | 11.55 |
| 50.4 | 3.56 | 5.230 | 11.47 |
| 53.2 | 3.56 | 5.218 | 11.47 |
| 56.6 | 3.54 | 5.198 | 11.31 |

Cell volumes are reported as cubic Angstroms
per number of atoms (Z) in the primitive cell.

**A-Type Y$_2$O$_3$**

Compression Data on A-Type Y$_2$O$_3$
Experimental Run: Y$_2$O$_3$ #1
Source: HPCAT ID-B

| P (GPa) | a(A$^3$) | c(A$^3$) | Vol(A$^3$)/Z |
|---------|----------|----------|--------------|
| 12.6 | 3.614 | 5.621 | 12.72 |
| 13.6 | 3.608 | 5.606 | 12.64 |
| 15.5 | 3.595 | 5.600 | 12.53 |
| 17.2 | 3.593 | 5.557 | 12.42 |
| 19.7 | 3.575 | 5.546 | 12.28 |
| 22.1 | 3.574 | 5.506 | 12.18 |
| 25.2 | 3.573 | 5.485 | 12.13 |
| 28.8 | 3.558 | 5.484 | 12.02 |
| 31.2 | 3.554 | 5.475 | 11.98 |

Cell volumes are reported as cubic Angstroms
per number of atoms (Z) in the primitive cell.

# REFERENCES

1. S. Cotton, <u>Lanthanide and Actinide Chemistry</u>, (2006).

2. B. Johansson, A. Rosengren, Interpolation scheme for the cohesive energies for the lanthanides and actinides, *Phys. Rev. B*, **11**, 1367-1373 (1975).

3. D. B. McWhan and A. L. Stevens, Effect of pressure on the Magnetic Properties and Crystal Structure of Gd, Tb, Dy, and Ho, *Phys. Rev. B*. **139**, 2836, (1965)

4. B. Johansson, A. Rosengren, Generalized phase diagram for the rare-Earth elements: Calculations and correlations of bulk properties, *Phys. Rev. B*, **11**, 2836-2857 (1975).

5. J. C. Duthie, D. G. Pettifor, Correlation between d-Band Occupancy and Crystal Structure in the Rare Earths, *Phys. Rev. Lett.*, **38**, 564-567 (1976).

6. Y. K. Vohra, H. Olijnik, W. A. Grosshans, W. B. Holzapfel, Structural Phase Transitions in Yttrium under Pressure, *Phys. Rev. Lett.,* **47**, 1065-1067.

7. V. P. Dmitriev, A. Yu. Kuznetsov, O. Bouvier, L Duborvinsky, D. Machon, H. P. Weber, Stability of the high-pressure monoclinic phases in Ce and Pr metals: Comparative diffraction study and phenomenological theory, *Phys. Rev. B*, **70**, 014104 (2004).

8. J.P. Rueff, J. P. Itie, M. Taguchi, et. al., Probing the g-a Transition if Bulk Ce under pressure: A Direct Investigation by Resonant Inelastic X-Ray Scattering, *Phys. Rev. Lett.*, **96**, 237403 (2006).

9. K. Haule, V. Oudovenko, S. Savrasov, G. Kotliar, The a-g Transition in Ce: A Theoretical View from Optical Spectroscopy, *Phys. Rev. Lett*. **94**, 036401 (2005).

10. C. Dallera, M. Grioni, A. Shukla, G. Vanko, et. al., New Spectroscopy Solves and Old Puzzle: The Kondo Scale in Heavy Fermions, *Phys. Rev. Lett.*, **88**, 196403 (2002).

11. W. A. Grosshans, Y. K. Vohra, W. B. Holzapfel, Evidence for a Soft Phonon mode and a New Structure in Rare-Earth Metals under Pressure, *Phys. Rev. Lett.* **49**, 1572-1575 (1982).

12. W. A. Grosshans, W. B. Holzapfel, Systematics of f Electron Delocalization in Lanthanide And Actinide Elements under Pressure, *Physica* **144B**, 14-18 (1986).

13. W. A. Grosshans, W. B. Holzapfel, Atomic volumes of rare-earth metals under pressures to 40 Gpa and above, *Phys. Rev. B*, **45**, 5171-5178 (1992).

14. N. Hamaya, Y . Sakamoto, H. Fujihisa, Y. Fujii, et. al., Crystal Structure of the distorted fcc high-pressure phase of praseodymium, *J. Phys. Condensed Matter*, **5**, L369-L374 (1993).

15. F. Porsch, W. B. Holzapfel, Symmetry change at the fcc--distorted-fcc phase transition of the lanthanides under pressure, *Phys. Rev. B*, **50**, 16212-16218 (1994).

16. W. B. Holzapfel, Structural systematics of 4f and 5f elements under pressure, *J. Alloys and Compounds*, **223**, 170-173 (1995).

17. D. A. Young, *Phase Transitions of the Elements* (University California Press, Berkley, 1991).

17. H. R. Hoekstra, Phase relationships in the Rare Earth Sesquioxides at High Pressure, *Journal of Inorganic Chemistry,* **5**, 754 (1965).

18. M. Zinkevich, Thermodynamics of rare earth sesquioxides, *Progress in Materials Science* **52**, 597–647 (2007).

19. W. Koehler, Neutron-Diffraction Study of the Structure of the A-form of the Rare Earth Sesquioxides, *Acta Cryst.,* **6,** 741 (1953).

20. H. Barnighausen, The Crystal Structure of A-CeO2, *Journal of the Less Common Metals*, **110**, 385 (1985).

21. R. Wyckoff, 2'nd Edition, Crystal Structures, Vol. 2, *Inter-Science*, New York, 1-22 (1967).

22. O. Guentert, The Monoclinic Modification of Gadolinium Sesquioxide Gd2O3, *Acta Cryst*., **11**, 746 (1958).

23. H. Yakel, A refinement of the Crystal Structure of Monoclinic Europium Sesquioxide, *Acta Cryst*., **B35**, 563 (1979).

24. D. Cromer, The Crystal Structure of Monoclinic Sm2O3 *J. Phys. Chem*., **61**, 753 (1957).

25. B. O'Connor, A Neutron Diffraction Study of the Crystal Structure of the C-for of Yttrium Sesquioxide, *Acta Cryst*., **B25**, 2140 (1969).

26. G. McCarthy, Crystal Data on C-type terbium Sesquioxide Tb$_2$O$_3$, *Acta Cryst*., **4**, 399 (1971).

27. F. Hanic, Real Structure of Undoped Y2O3 Single Crystals, *Acta Cryst.* **B40**, 76 (1984).

28. E. Malsen, A synchrotron X-ray Study of the Electron Density in C-Type Rare Earth Oxides, *Acta Cryst*, **B52**, 414 (1996).

29. G. Chen, Systematics of the Phase Behavior in Lanthanide Sesquioxides, *Journal of*

*Alloys and Compounds*, **186**, 233 (1992).

30. J. Sawyer, Pressure and Polymorphisms in the Rare Earth Sesquioxides, *Journal of Inorganic Chemistry*, 426 (1964).

31. V.B. Glushkova, Polymorphisms of Rare-Earth Sesquioxides, *Izvestiya Akademii Nauk SSSR*, **7**, 1131 (1965).

32. T. Atou, Pressure-Induced Phase Transitions in Rare Earth Sesquioxides, *High-Pressure Research: Application to Earth and Planetary Sciences,* 469 (1992).

33. T. Atou, Reversible B-Type – A-Type transition of $Sm_2O_3$ Under High Pressure, *Material Research Bulletin*, **24**, 1171 (1989).

34. G. Chen, An Energy-Dispersive X-Ray Diffraction Study of Monoclinic Eu2O3 Under Pressure, *Journal of Solid State Chemistry*, **111**, 447 (1994).

35. E. Husson, Phase Transitions In Yttrium Oxide at High Pressure Studied by Raman Spectroscopy, *Materials Research Bulletin*, **34**, 2085 (1999).

36. C. Meyer, Mossbauer and Energy-Dispersive X-Ray Diffraction Studies of the Pressure-Induced Crystallographic Phase transition in C-type $Yb_2O_3$, *Physical Review B*, **51**, 187 (1995).

37. T. Hongo, T. Atou, High Pressure Spectroscopic Study of the Structural Phase Transition in Samarium Oxide, *Journal of Material Science*, **43**, 2582 (2007).

38. C. E. Weir, E. R. Lippincott, A. Van Valkenburg, and E. N. Bunting, Infrared Studies in the 1- to 15-Micron Region to 30,000 Atmospheres, *J. Res. Natl. Bur. Stand.* **63A**, 55-62(1959).

39. A. Jayaraman, Ultrahigh Pressures, *Review of Scientific Instrumentations*, **57**, 1013 (1986).

40. G. J. Piermarini, S. Block, J. D. Barnett, and R. A. Forman, Calibration of the Pressure Dependence of the R1 Ruby Fluorescence Line to 195 kbar, *J. Appl. Phys*. **46**, 2774-2780 (1975).

41. D. L. Decker, Equation of State of NaCl and Its Use as a Pressure Gauge in High-Pressure Research, *J. Appl. Phys.* **36**, 157 (1965).

42. P.W. Bridgeman, *Proc. Am. Acad. Arts Sci.*, 74, 21 (1940).

43. H. Mao, P. Bell, J. Shaner, D. Steinberg, Specific volume measurements of Cu, Mo, Pd, and Ag and calibration of the ruby R1 fluorescence pressure gauge from 0.06 to 1 Mbar, *Journal of Applied Physics*, **49**, 3276 (1978).

44. H. Mao, J. Xu, P. Bell, Calibration of the Ruby Pressure Gauge to 800 kbar Under Quasi-Hydrostatic Conditions, *Journal of Geophysical Research*, **91**, 4673 (1986).

45. A. Dewaele, P. Loubeyre, M. Mezouar, Equations of state of six metals above 94 Gpa, *Physical Review B*, **70**, 094112 (2004).

46. J. J. Eggert, F. Moshary, W. J. Evans, K.A. Goettel, I. F. Silvera, Ruby at high pressure. III. A pumping scheme for the R lines up to 230Gpa, *Phys. Rev. B*. **44**, 14 (1991).

47. K. Nakamoto, 5'th Edition, Infrared and Raman Spectra of Inorganic and Coordination Compounds, *Wiley-Interscience*, New York (1997).

48. M. Eremets, High Pressure Experimental Methods, *Oxford University Press*, New York (1996).

49. W.I.F David, K. Shankland, L.B. McCusker, Ch. Baerlocher, Structure Determination from Powder Diffraction Data, *IUCr Monographs on Crystallography*, Oxford, New York (2002).

50. J.A. Nielson, D. McMorrow, Elements of Modern X-Ray Physics, *Wiley*, England (2001).

51. A P Hammersley, *ESRF Internal Report*, **ESRF97HA02T**, ``FIT2D: An Introduction and Overview'', (1997)

52. A.C. Larson and R.B. Von Dreele*,* "General Structure Analysis System (GSAS)", *Los Alamos National Laboratory Report,* LAUR 86-748 (1994).

53. D.L. Bish, J.E. Post, Modern Powder Diffraction, *Reviews in Mineralogy* **20** (277-308).

54. L.B. McCusker, R.B. Von Dreele, *et. al*, Rietveld Refinement Guidelines, *Journal of Applied Crystallography*, **32**, 36-50, (1999).

55. R. LeSar, D. Schiferl, et. al., Raman Spectroscopy of Solid Nitrogen up to 374 kbar, *Solid State Communications*, **32**, 131 (1979).

56. Zin, Schiferl, Nicol J. Chem. Phys. **87** 1267 (1987).

57. K. Takemura, Hydrostatic Experiments up to Ultrahigh Pressures, *J. Phys. Soc. Japan*, **79**, 202 (2007).

58. F. Stacey, Finite Strain, Thermodynamics and the Earth's Core, *Physics of the Earth and Planetary Interiors*, **128**, 179 (2001).

59. W. B. Holzapfel, Physics of Solids Under Strong Compression, *Rep. Prog. Phys*. **59**, 29 (1996).

60. K. S. Singh and N. S. Parmar, Infinite Pressure Behavior of Certain Inverted Type Equations of State for Solids, *J. Phys. Chem. Solids*, 67, 2392 (2006).

61. B. P. Singh, A Comparison of Equations of State Including the Generalized Rydberg EOS, *Physica B*, **369**, 111 (2005)

62. E. B. Wilson, J. C. Decius, and P. C. Cross, *Molecular Vibrations*, McGraw-Hill, New York, (1955).

63. T. Shimanouchi and M. Tsuboi, *J. Chem. Phys.,* **35**, 5, (1961).

64. K. Nakamoto, *Infrared and Raman Spectra of Inorganic and Coordination Compounds,* 5'th ed., John Wiley & Sons, Inc., New York, 1997.

65. J.R. Ferraro and J.S. Ziomek, *Introductory Group Theory and its Applications to Molecular Structure*, 2'nd ed., Plenum Press, New York, 1975.

66. A. K. Singh et. al., Analysis of Lattice Strains Measured Under Non-Hydrostatic Pressure, *J. Appl. Phys*. **83**, 12, 1998

67. R. Downs and A. Singh, *J. Phys. Chem. Solids*, **67** 2006

68. F.X. Zhang, et.al., *Phys. Rev. B*, **70**, 094112 (2004).

69. J. H. Denning and S. D. Ross, *J. Phys. C: Solid State Phys.,* **5**, 1123 (1972).

70. S. Boldish and W White, *Spectrochemica Acta.,* **35A**, 1235 (1979).

71. Zarembowitch et. al., *Phys. Stat. Sol.,* **94**, 249 (1979).

72. J. Gouteron, D. Michel, A. M. Lejus, J. Zarembowitch, *J. Solid State Chem.,* **38**, 288 (1981).

73. P. Toledano, *Phys. Rev. B,* **25**, 3 (1982).

74. J. C. Toledano, P. Toledano, *The Landau Theory of Phase Transitions*, World Scientific, Singapore, Oxford (1980).

75. P. Fleury, *Annu. Rev., Mater. Sci.,* **6**, 157-180 (1976).

VITA

Graduate College
University of Nevada, Las Vegas

Jason Patrick McClure

Degrees:
    Bachelor of Science, Physics, 2002
    Denison University, Granville

Publications:
    O. Tschauner, B. Kiefer, J. McClure, and S. Sinogeikin, Submited to *Journal of Physics\Conf.Ser* (2009)

    H. Kohlmann, Y. Zhao, M. Nicol, and J. McClure, *Z. Kristallogr.,* **223**, 706-710 (2008)

    O. Tschauner, J. McClure, and M. Nicol, *Journal of Synchrotron Radiation*, **12**, 626-631 (2005).

Dissertation Title: High Pressure Phase Transitions in the Lanthanide Sesquioxides

Dissertation Examination Committee:
    Co-Chairperson, Andrew Cornelius, Ph.D.
    Co-Chairperson, Oliver Tschauner, Ph.D.
    Committee Member, Len Zane, Ph.D.
    Committee Member, Brendon O'Toole, Ph.D.